



Thaís Cristina Viana de Carvalho

**Chemical, structural, tribological, and optical
properties of hexagonal boron nitride films
synthesized by chemical vapor deposition.**

Tese de Doutorado

Thesis presented to the Programa de Pós-graduação em Física of
PUC-Rio in partial fulfillment of the requirements for the degree
of Doutor em Ciências - Física

Advisor : Prof. Marcelo Eduardo Huguenin Maia da Costa
Co-advisor: Prof. Cesar Augusto Diaz Mendoza

Rio de Janeiro
June 2024



Thaís Cristina Viana de Carvalho

**Chemical, structural, tribological, and optical
properties of hexagonal boron nitride films
synthesized by chemical vapor deposition.**

Thesis presented to the Programa de Pós-graduação em Física of PUC-Rio in partial fulfillment of the requirements for the degree of Doutor em Ciências - Física. Approved by the Examination Committee:

Prof. Marcelo Eduardo Huguenin Maia da Costa

Advisor

Departamento de Física – PUC-Rio

Prof. Cesar Augusto Diaz Mendoza

UERJ

Prof. Dante Ferreira Franceschini Filho

UFF

Prof. Paola Alexandra Ayala Hinojosa

Universidade de Wien

Prof. Claudio Radtke

UFRGS

Prof. Alexandre de Resende Camara

UERJ

Rio de Janeiro, June 21st, 2024

All rights reserved.

Thaís Cristina Viana de Carvalho

Graduated in physics (2017) and obtained her M.Sc. Degree in Physics (2020), both from the Universidade Federal do Piauí.

Bibliographic data

Carvalho, Thaís

Chemical, structural, tribological, and optical properties of hexagonal boron nitride films synthesized by chemical vapor deposition. / Thaís Cristina Viana de Carvalho; advisor: Marcelo Eduardo Huguenin Maia da Costa; co-advisor: Cesar Augusto Diaz Mendoza. – 2024.

118 f: il. color. ; 30 cm

Tese (doutorado) - Pontifícia Universidade Católica do Rio de Janeiro, Departamento de Física, 2024.

Inclui bibliografia

1. Física – Teses. 2. Método LPCVD. 3. Nitreto de Boro hexagonal (h-BN). 4. Substrato de Silício. 5. Isolante. I. Costa, Marcelo. II. Pontifícia Universidade Católica do Rio de Janeiro. Departamento de Física. III. Título.

CDD: 004

To my friends and family.

Acknowledgments

I would like to express my gratitude, firstly, to my advisor, Professor Marcelo, for welcoming me into his research group, for his trust in my work, and for his availability and support throughout these years.

I express my gratitude to the entire research group at the Van de Graaff laboratory, led by Professor Lázaro, and his team: Andre, Cesar, Neileth, and Shuai. Thank you for the support, teachings, and enjoyable moments. Without you, everything would certainly be much more complicated.

I extend my thanks to my family, particularly to my parents, Raimundo and Maria da Conceição, for supporting my choices. I also appreciate my siblings, their spouses, and my dear nieces, Luísa and Cecília. Despite the physical distance, I received complete support, affection and understanding.

I am immensely grateful to my friends and colleagues at PUC-Rio for the pleasant moments, conversations, and knowledge exchanges. And to everyone in the study room, Rodrigo, Priscila, and Moysés. Valuable partnership at all times. I especially thank my friends from Piauí, Júnior, Anupama, Caique, Cícera, Lívio, João which are with me since graduation.

I also want to express my gratitude to the staff members, Giza, Eduardo, Nilton, Sérgio, and Edson for always being willing to help with whatever was necessary. Specially to Suellen, for always to share her chemicals knowledge's. My heartfelt thanks. Specifically for the long and pleasant conversations that made this journey lighter and significantly contributed to my reaching this point.

I would like to thank Professor Rodrigo Prioli, and Carlos Senna for the STEM and SEM measurements. I thank Professor Alexandre Camara for welcoming me to his laboratory at UERJ-RJ and for conducting the UV-vis measurements. I would like to thank Prof. Claudio Radtke for sending the precursor material, without which this work would not have been completed. And, I also thank Professor Juan Lucas Nachez for the tribology measurements and for welcoming me to his laboratory at UFF-RJ.

This study was financed in part by the Coordenação de Aperfeiçoamento de Pessoal de Nível Superior - Brasil (CAPES) - Finance Code 001. To CNPq, and PUC-Rio, I extend my gratitude for the grants provided.

Abstract

Carvalho, Thais; Costa, Marcelo (Advisor); (Co-Advisor). **Chemical, structural, tribological, and optical properties of hexagonal boron nitride films synthesized by chemical vapor deposition.** Rio de Janeiro, 2024. 118p. Tese de Doutorado – Departamento de Física, Pontifícia Universidade Católica do Rio de Janeiro.

Hexagonal Boron Nitride (h-BN) is a material composed of alternating Boron (B) and Nitrogen (N) atoms with a hexagonal aspect. Thin films of h-BN play a crucial role in the development of applications such as 2D devices based on Van der Waals heterostructures, protective coatings, tribological applications, among others. The synthesis of h-BN still represents a significant challenge. In this thesis, the synthesis of h-BN was investigated using the low-pressure chemical vapor deposition (LPCVD) method, employing ammonia borane (AB) as a precursor source of B and N. The study focused on direct growth on the silicon $\langle 100 \rangle$ substrate, thus eliminating the need for film transfer for subsequent characterization and avoiding degradation and contamination associated with the transfer process. The first part of this study focused on CVD growth, controlling parameters such as the amount of precursor material, precursor and furnace evaporation temperature, gas flow rates during the reduction and synthesis stages, temperature, reduction time, synthesis, and cooling. Two series were synthesized: one as a function of growth temperature between 1173 and 1373 K, and a second as a function of synthesis time at a temperature of 1373 K. The films were characterized by spectroscopy, Raman, Fourier-transform infrared (FTIR), UV-visible (UV-Vis), X-ray photoelectron (XPS), atomic force microscopy (AFM), contact angle measurements, scanning electron microscopy (SEM), scanning transmission electron microscopy (STEM), and tribology. Initially, the effect of growth temperature on the quality of films grown for 10 minutes was studied. Raman spectroscopy results confirmed the growth of h-BN, evidenced by the E_{2g} peak at approximately 1375 cm^{-1} . Morphological studies showed that temperature variations lead to the formation of different structures on the Si surface. Growth is observed from 1273 K, while samples grown below 1223 K show no signs of growth. We observed the formation of two-dimensional (2D) nanosheets with lateral dimensions ranging from 80 to 500 nm, as well as the continuous growth of films with nanocrystals of varying sizes. The B:N ratio determined by XPS was

approximately 1:1, and the optical gap of the h-BN films was determined to be 5.75 eV. Tribology studies demonstrated a friction coefficient of 0.1, and there was no delamination after 3000 linear reciprocating cycles in the ball-on-disk test, covering 10 mm in each cycle on the film, while for Si it was 0.6. For films synthesized as a function of time, Raman spectroscopy characterization revealed an E_{2g} vibration mode peak at 1374 cm^{-1} with intensity correlated to the film thickness. FTIR spectroscopy confirmed the presence of B-N bonds, and the optical band was determined to be 5.65 eV. Contact angle measurements showed hydrophobic films. XPS data indicated a stoichiometric 1:1 ratio between B and N, and the thickness was analyzed by cross-sectional STEM measurements, being around 20 nm for films grown for 10 minutes at 1373 K.

Keywords

LPCVD method; hexagonal Boron Nitride (h-BN); Silicon (Si) substrate; Insulator; .

Resumo

Carvalho, Thais; Costa, Marcelo; . **Propriedades químicas, estruturais, tribológicas e ópticas de filmes de nitreto de boro hexagonal sintetizados por deposição química na fase vapor.** Rio de Janeiro, 2024. 118p. Tese de Doutorado – Departamento de Física, Pontifícia Universidade Católica do Rio de Janeiro.

O Nitreto de Boro Hexagonal (h-BN) é um material composto por átomos alternados de Boro (B) e Nitrogênio (N) com um aspecto hexagonal. Os filmes finos de h-BN desempenham um papel crucial no desenvolvimento de aplicações como em dispositivos 2D baseados em heteroestruturas de Van der Waals, revestimentos protetivos, tribológicos, entre outros. A síntese de h-BN ainda representa um desafio significativo. Nesta tese, investigou-se a síntese do h-BN utilizando o método de *low pressure chemical vapour deposition* (LPCVD), empregando amônia borane (AB) como fonte precursora de B e N. O estudo focou-se no crescimento direto sobre o substrato de silício $\langle 100 \rangle$, eliminando, assim, a necessidade de transferência do filme para posterior caracterização e evitando a degradação e contaminações associadas ao processo de transferência. A primeira parte deste estudo concentrou-se no crescimento por CVD, controlando os parâmetros de quantidade de material precursor, temperatura de evaporação do precursor e do forno, fluxo de gases nas etapas de redução e de síntese, temperatura, tempo de redução, síntese e resfriamento. Foram sintetizadas duas séries: uma em função da temperatura de crescimento entre 1173 e 1373 K, e uma segunda em função do tempo de síntese a uma temperatura de 1373 K. Os filmes foram caracterizados por espectroscopias Raman, infravermelho por transformada de Fourier (FTIR), UV-visível (UV-Vis), de fotoelétrons excitados por raios X (XPS), microscopia de força atômica (AFM), ângulo de contato, microscopia eletrônica de varredura (SEM), microscopia eletrônica de varredura por transmissão (STEM) e tribologia. Inicialmente, foi estudado o efeito da temperatura de crescimento na qualidade dos filmes crescidos por 10 minutos. Os resultados de espectroscopia Raman confirmam o crescimento de h-BN, evidenciado pelo pico E_{2g} em aproximadamente 1375 cm^{-1} . Estudos morfológicos mostraram que variações de temperatura levam à formação de diferentes estruturas na superfície do Si. O crescimento é observado a partir de 1273 K, enquanto amostras crescidas abaixo de 1223 K não

apresentam sinais de crescimento. Observamos a formação de folhas bidimensionais (2D) com dimensões laterais variando de 80 a 500 *nm*, assim como o crescimento contínuo de filmes com nanocristais de tamanhos variados. A razão B:N determinada por XPS foi de aproximadamente 1:1 e o gap óptico dos filmes de h-BN foi determinado em 5,75 eV. O estudo de tribologia demonstrou um coeficiente de atrito de 0,1 e não houve delaminação após 3000 ciclos de ida e volta lineares no teste esfera no disco percorrendo 10 mm em cada ciclo no filme, enquanto o do Si foi de 0,6. Para os filmes sintetizados em função do tempo, a caracterização por espectroscopia Raman revelou um pico de modo de vibração E_{2g} em 1374 cm^{-1} com intensidade correlacionada à espessura do filme. A espectroscopia FTIR confirmou a presença de ligações B-N, e a banda óptica foi determinada em 5,65 eV. O ângulo de contato mostrou filmes hidrofóbicos. Os dados de XPS indicaram uma relação estequiométrica 1:1 entre B e N, e a espessura foi analisada pela medida de seção transversal por STEM, sendo da ordem de 20 *nm* para filmes crescidos por 10 minutos a 1373 K.

Palavras-chave

Método LPCVD; Nitreto de Boro hexagonal (h-BN); Substrato de Silício; Isolante.

Table of contents

1	Introduction	21
1.1	Aim and scope	23
1.2	State of the art	24
2	Structure, Properties and Applications of h-BN	27
2.1	Structure	27
2.2	Properties	28
2.3	Applications	32
3	Theoretical Background	36
3.1	Fundamentals concepts about Raman Scattering	36
3.2	Fourier-Transform Infrared Spectroscopy	41
3.3	X-ray Photoelectron Spectroscopy	44
3.4	Principles of atomic force microscopy (AFM)	47
3.5	Wettability	51
3.6	Scanning Transmission Electron Microscopy (STEM)	53
3.7	Scanning Electron Microscopy (SEM)	55
3.8	Ultra Violet visible spectroscopy	56
3.9	Tribology	58
3.10	Chemical Vapor Deposition - (CVD)	60
3.11	Ultrasonic bath	61
4	Methodology	63
4.1	Materials and methods	63
4.2	Borane - ammonia complex (AB) Precursor	64
4.3	Substrate preparation	66
4.4	Cleaning procedure of quartz tube and crucible	66
4.5	Hexagonal Boron Nitride (h-BN) synthesis process	67
5	Equipment and procedures for characterization	70
5.1	Raman spectroscopy/atomic force microscopy (AFM)	70
5.2	FTIR spectroscopy	71
5.3	XPS spectroscopy	72
5.4	UV-vis spectroscopy	73
5.5	Contact Angle (Goniometer)	74
5.6	Microtribometer	74
6	Temperature-dependent growth of h-BN films	75
6.1	Raman spectroscopy	75
6.2	UV- visible spectroscopy	78
6.3	X-ray Photoelectron Spectroscopy (XPS)	79
6.4	Atomic Force Microscopy (AFM)	80
6.5	Scanning Electron Microscopy (SEM)	83
6.6	Contact Angle	85
6.7	Tribology	85

6.8	Summary	91
7	Time-dependent growth of h-BN films	92
7.1	Raman spectroscopy	92
7.2	XPS	94
7.3	AFM	97
7.4	Contact Angle	99
7.5	UV-visible spectroscopy	102
7.6	Summary	103
8	Conclusion and perspectives	105
9	Bibliography	107

List of figures

- Figure 1.1 Left panel: Optical image of as-grown NCBN film on SiO_2 surface. Right panel: Cross-section TEM image showing 7 layers with interlayer distance of 0.35 nm for film grown for 5 min [1]. 25
- Figure 1.2 Left panel: Optical image of the manufactured device on a NCBN film. Right panel: I-V plot for the NCBN device, indicating the non-conducting properties of the films [1]. 25
- Figure 1.3 Left panel: Raman spectra of the h-BN samples grown on Si substrates by LPCVD at deposition temperatures range of 1173-1573 K. Right panel: cross sectional SEM images of h-BN films grown on the Si substrate at 1473 K [2]. 26
- Figure 1.4 (a) UV-visible absorption spectrum, the inset is optical bandgap on a quartz substrate. (b) I-V characteristics of the h-BN photodetector ($2.3 \mu m$ thick) measured at room temperature in dark and under UV-enhanced, xenon lamp light irradiation, the inset shows the schematic of the photodetector [2]. 26
- Figure 2.1 Left panel: Crystal structure of h-BN. Right panel: hexagonal structure of monolayer h-BN, showing the unit cell defined by the lattice vectors a_1 and a_2 [3, 4]. 27
- Figure 2.2 Microstructure of atomic layers hexagonal BN. (a-c) HRTEM images of the film edges, with two to five layers (scale bar $5 nm$). The insert of (a) is the corresponding SEAD of the regions, (d) A typical atomic image of a h-BN films. The scale bars is $2 nm$. (e) The fast Fourier transform pattern of a region of panel d, (f) EELS spectrum of a h-BN film [5]. 28
- Figure 2.3 Crystal structure of (a) wurtzite (wz-BN); and (b) zinc-blende (zb-BN) crystals [3]. 28
- Figure 2.4 Phonon-dispersion curve of bulk h-BN calculated theoretically in the high symmetry points of Brillouin zone (BZ) [6]. 29
- Figure 2.5 Left panel: band structure of monolayer h-BN calculated theoretically in the high symmetry points of Brillouin zone (BZ). Are indicated the Fermi energy E_F i. e., the zero of the energy, $B-P_z$ and $N-P_z$ orbitals [3]. 29
- Figure 2.6 (a) Scanning Electron Micrograph of a Large h-BN film spanning an array of circular holes $1 \mu m$ in diameter, and (b) Schematic of nanoindentation performed on a suspended h-BN membrane [5]. 31
- Figure 2.7 Typical ultraviolet-visible absorption spectra of h-BN film [5]. 32
- Figure 2.8 Schematic of graphene (GR) device structure with grown h-BN nanosheets [7]. The mobility of charge carriers in graphene as a function of carrier density. 33
- Figure 2.9 (a) Design and Characteristics of a high performance Field-Effect Transistor (FET) based on WSe_2 with contacts made of 2D/2D, and (b) depict the optical micrograph encapsulation of the channel region in h-BN from Both top and bottom within the device [8]. 34

Figure 3.1	Rayleigh scattering, Stokes Raman and anti-Stokes Raman scattering [9].	38
Figure 3.2	Schematic representation of Feynman diagrams for one-phonon Stokes and anti-Stokes scattering and the symbols used in drawing Feynman diagrams [10].	39
Figure 3.3	Raman spectra of h-BN film: (a) Raman spectra of h-BN films with different thicknesses. The inset shows a plot of Raman peak intensity against the number of h-BN layers. (b) A plot of Raman peak position versus the number of h-BN layers [11].	41
Figure 3.4	Absorption of electromagnetic radiation.	42
Figure 3.5	Shows the relation of the electronic states density in the sample onto the distribution of kinetic energy of the photoelectrons. Electrons in occupied states are detectable once they are excited above the vacuum level by electrons with energy $\hbar\omega$ [12].	44
Figure 3.6	Basics components of XPS experiment, include photon source, sample to be analyzed, analyzer and a detector [12].	45
Figure 3.7	A hemispherical electron energy analyzer of XPS instruments.	46
Figure 3.8	Survey spectra of an h-BN sample in the spectral range of energy from 0 to 1000 eV. Are highlighted the interest elements to posterior analysis [1].	47
Figure 3.9	The schematic illustrates an Atomic Force Microscope components. A sharp tip mounted on the end of a cantilever, a position-sensitive photodiode, laser diode, sample to be measured, sample holder (base), piezo scanner are shown.	48
Figure 3.10	Two modes of operation are depicted. Small circles represent sample atoms, and dotted lines represent the contour of constant force. a) Contact mode and b) Non-contact mode.	49
Figure 3.11	The force-distance curve for contact (repulsive region) mode scanning regime. The deflection-distance curve, may be converted to a force-distance curve, both have a similar shape. Right: illustration of probe bending [13].	49
Figure 3.12	The force-distance curve for non-contact (attractive regime) AFM [13].	50
Figure 3.13	Intermittent-contact operating regime. In this mode, the AFM probe's oscillation is large enough to move from the repulsive regime through the attractive regime [13].	51
Figure 3.14	Wetting model diagram: (a) Young's model; (b) Wenzel's model	52
Figure 3.15	Water droplets on bare Si and on the Si substrate coated with h-BN films at 10 min of growth time deposition. (a) bare Si - $\theta = 61.0^\circ \pm 1.0$, and (b) 10 min - $\theta = 105.0^\circ \pm 5.0$.	53
Figure 3.16	Schematic diagram of the major STEM components [14].	54
Figure 3.17	Schematic of the various electron detectors in a STEM [15].	55
Figure 3.18	Schematic of the electron column showing the electron gun, lenses, the deflection system, and the electron detector [16].	56

Figure 3.19 The Jablonski diagram for a hypothetical molecule illustrates various photophysical processes. It depicts the absorption of a photon (indicated by purple and green arrows, thermal (non-radiative) relaxation processes including internal conversion (IC) and intersystem crossing (ISC) (represented by black arrows), fluorescence (yellow arrow), and phosphorescence (red arrow). 57

Figure 3.20 (a) A schematic diagram of two surfaces in static contact shows that the contact occurs at only a few discrete contact spots, and (b) two surfaces in sliding contact, therefore the interfacial forces act on these contact spots [17]. 59

Figure 3.21 Illustrates the setup utilized for the CVD process. The Si <100> substrate is positioned at the center of the hot zone within the furnace, ensuring optimal exposure to the precursor gases for h-BN film deposition. 60

Figure 3.22 Left: the schematic depiction of the ultrasonic cleaning apparatus illustrates key components, including the immersed sample within the solvent, the water bath contained within the tank, and the transducer [18]. Right: ultrasonic cleaner in the *Laboratório de Revestimentos Protetores e Materiais Nanoestruturados* at PUC-Rio. 62

Figure 4.1 Raman spectroscopy of Ammonia - borane (AB) powder pure, and the residual material collected after synthesis, heated at 373 K and 403 K. (a) Raman spectra of the entire region of the powder of AB pure, heated at 373 K and 403 K, respectively. Indicating three distinct regions R_1 , R_2 , and R_3 . (b) the peak in the region R_1 at $\sim 785\text{ cm}^{-1}$ is related to BN bonds. (c) the peak in the region R_2 at $\sim 2285\text{ cm}^{-1}$ is related to BH bonds and (d) the peak in the region R_3 at $\sim 3257\text{ cm}^{-1}$ is related to NH bonds. 65

Figure 4.2 Si substrate of 500 ± 15 micrometers (μm) thick cut with a diamond-tipped pen tool in the preferred crystal orientation. 66

Figure 4.3 Apparatus employed for the deposition of h-BN films comprises: (a) a single-stage temperature-controlled CVD system, (b) an oven temperature controller, (c) the powering and display mechanisms for two Baratron® transducers, calibrated to measure in units of mTorr and Torr, and (d) gas cylinders accessible in the laboratory, including argon, oxygen, hydrogen, and methane. 67

Figure 4.4 Overview temperature profile diagram depicting the temperature distribution within the CVD furnace. The temperature gradient is monitored, starting from the ramp-up to reach 1373 K the deposition temperature and subsequently the growth duration at 20 min of the h-BN films, finally the cool down phase with the opening of CVD chamber to allow the system to cool at a rate of $\sim 300\text{ K/min}$ for 2.5 minutes until it reached 773 K, after that, it took over 1 hour and 30 min for the system to return to room temperature under ambient air conditions. 69

Figure 5.1 The Raman spectrometer used to analyze the samples in the *Laboratório de Revestimentos Protetores e Materiais Nanoestruturados* at PUC-Rio. 70

Figure 5.2 FTIR spectrometer used to study the vibrational characteristics of the sample in the *Laboratório de Revestimentos Protetores e Materiais Nanoestruturados* at PUC-Rio. 72

Figure 5.3 X-ray photoelectron spectrometer used to study chemical composition of the samples in the *Laboratório de Revestimentos Protetores e Materiais Nanoestruturados* at PUC-Rio. 73

Figure 5.4 Goniometer setup used to contact angles measurements in the *Laboratório de Revestimentos Protetores e Materiais Nanoestruturados* at PUC-Rio. 74

Figure 6.1 Raman spectrum of an h-BN film showing the entire region of Si characteristics in the range from 100 to 1600 cm^{-1} . The Si modes are characterized as the transverse optic (TO)- 520 cm^{-1} , second order longitudinal acoustic (2LA) and second order transversal optic (2TO). On the other hand, the inset Figure show the E_{2g} vibrational mode of h-BN, Si mode at 1450 cm^{-1} , and molecular Oxygen O_2 at ~ 1563 cm^{-1} . 76

Figure 6.2 Raman spectra of h-BN samples grown in the temperature range of 1273 to 1373 K. In (a) shows the Raman spectra of the h-BN characteristic E_{2g} vibration mode, the dashed line shows that these peaks do not suffer significant shifts for blueshift or redshift. Including the peaks referring to the Si and the molecular oxygen peak, at ~ 1450 and O_2 , ~ 1563 cm^{-1} . (b) show the A_{1g} characteristic out-of-plane h-BN vibration mode observed in a sample grown for 5 minutes. It is noteworthy that the A_{1g} peak is consistently observed across all samples. 77

Figure 6.3 UV-Vis spectrum of h-BN film 10 min at 1273, and 1323 K on a Si substrate. The inset shows the optical bandgap analysis of the h-BN film. In (a) and (b) the E_g was 5.7 eV. 78

Figure 6.4 XPS spectra of the samples grown in the temperature of 1323, and 1373 K. In (a) show the B $1s$ spectrum of the B-N and B-O overlap (b) show the N $1s$ spectrum of the N-B and N-C overlap, and (c) show the spectra of the Si $2p$ (Si-Si at 99 eV and Si-N at 102 eV) regions of the as-grown sample at 1323 K. (d) and (e) highlight the Survey spectra of the elements in the region, Si $2p$, B $1s$, C $1s$ and N $1s$. 79

Figure 6.5 AFM images of h-BN films with a scan size of 1 μm^2 at 1273 K. In (a) shows the 2D nanosheet-like structures with the roughness of $RMS = 1.0 \pm 0.2$ nm, (b) the 3D image, (c) the height of the 2D nanosheet of 2.5 ± 0.6 nm and (d) the height distribution with the main lying on 3.0 nm. 81

Figure 6.6 AFM images of h-BN films with a scan size of 1 μm^2 at 1323 K. In (a) the obtained roughness was $RMS = 1.5 \pm 0.3$ nm, (b) the 3D plot, (c) indicates the height of a point without nucleation of 10.3 ± 1.5 nm taken from (a) in the green dashed line, (d) shows the height distribution with the main lying on 10.5 ± 1.0 nm. 82

Figure 6.7 AFM image showing the topography of the 10 min sample of an area of 1 μm^2 , (a) showing almost total coverage of the substrate surface. The grain analysis shows the respective $RMS = 6.8 \pm 1.3$ nm roughness. In (b) a 3D image of the film surface, (c) the height of the film of 17 ± 0.8 nm along the pink line direction in a region without nucleation, and (d) the histogram of the height distribution of the h-BN film ranging from 0 to 20 nm. 83

Figure 6.8 Scanning electron microscopy (SEM) images of h-BN samples in the temperature range of 1273 to 1373 K. (a-b) show at 1273 K sample. (c-d) depict sample grown at 1323 K showcasing this point defects on the film's surface. (e-f) exhibiting a circular pattern for the samle at 1373 K characterized by small aspect ratios, identified as "hillocks" features with a brighter contrast (white). 84

Figure 6.9 Raman spectra of the as-grown h-BN samples. (a), (b) and (c) displays the characteristic vibrational mode E_{2g} at approximately 1375 cm^{-1} . 86

Figure 6.10 Vibrational spectra obtained from FTIR spectroscopy. (a), (b) and (c) shows the corresponding absorption peak at 1375 cm^{-1} . 86

Figure 6.11 AFM images of the h-BN sample grown on Si at 1373 K for 1 hour are shown. (a) Displays the sample morphology with a root mean square (RMS) roughness of $7.7 \pm 2.1\text{ nm}$, (b) the corresponding 3D profile, (c) the height profile of $30.0 \pm 5.3\text{ nm}$ taken from the vertically dashed line indicated in (a), and (d) the height distribution, with the main peak lying at 40 nm . 87

Figure 6.12 AFM images of the h-BN sample grown on Si for 1 hour are shown. Displays the sample topography with a root mean square (RMS) roughness of (a) $12.8 \pm 2.6\text{ nm}$, (b) $1.99 \pm 0.1\text{ nm}$, and (c) $1.5 \pm 0.2\text{ nm}$ for the samples at 1373, 1323 and 1273 K, respectively. 88

Figure 6.13 XPS spectra of the sample grown at 1273 K for 1 hour. In (a) show the B $1s$ spectrum of the B-N and B-O overlap, (b) show the N $1s$ spectrum of the N-B and N-C overlap, and (c) highlight Survey spectra of the elements in the region, Si $2p$, B $1s$, C $1s$ and N $1s$. 88

Figure 6.14 Presents the results obtained from the tribology test conducted on the Si $\langle 100 \rangle$ substrate and Si coated with h-BN (h-BN/Si) samples grown at 1 hour at 1273, 1323, and 1373 K, respectively. Under linear reciprocating ball-on-disc test. The test involved a constant sliding speed of 10 mm/s , a 10 mm sliding distance, and a corresponding Hertzian pressure of 398 MPa , displaying the variation of the coefficient of friction (CoF) with time (s). 89

Figure 6.15 Study of Wear tracks through Profilometry. (a) A 3D profile of the wear track from the tribology test of a bare Si substrate, (b) The height of the scratch corresponding to (a), indicating a depth of $\sim 1340\text{ nm}$, (c) A 3D profile of the wear track of the 1373 K (sample), and (d) The height of the scratch corresponding to (c), indicating a depth of $\sim 15.7\text{ nm}$. 90

Figure 6.16 Study of Wear tracks through Profilometry. (a) A 3D profile of the wear track from the tribology test for 1323 K (sample), (b) The scratch height corresponding to (a) of $\sim 10\text{ nm}$, (c) A 3D profile for 1273 K (sample), and (d) The height of $\sim 160\text{ nm}$. 91

Figure 7.1 Raman spectra of h-BN samples grown at 1373 K variation in growth time between 5, 10, and 20 minutes under Si substrate. In (a) shows the Raman spectra of samples with different growth times the characteristic E_{2g} vibration mode, the dashed line shows that these peaks do not suffer significant shifts for blueshift or redshift. Are highlighted peaks referring to the silicon substrate and the molecular oxygen peak, at ~ 1450 and O_2 , $\sim 1563 \text{ cm}^{-1}$. In (b) show the A_{1g} relative to the out-of-plane h-BN vibration mode sample grown at 5 minutes. The A_{1g} peak is present in all samples. 93

Figure 7.2 Infrared transmission spectra of films grown at 10 min (1373 K). The absorption band at $\sim 1373.2 \text{ cm}^{-1}$, is attributed to B-N bonds characteristic of the in-plane ring vibration. 94

Figure 7.3 XPS spectra of the samples in the range of 5-20 min growth at 1373 K. In (a) are the N $1s$ spectrum of the N-B and N-C overlap, (b) the B $1s$ spectrum of the B-N and B-O overlap, and (c) the from the Survey highlighting the elements in the region, Si $2p$, B $1s$, C $1s$ and N $1s$ for the 20 min sample. In (d-i) show the N $1s$, B $1s$ and Survey spectra for the 10 and 5 min samples, respectively. 95

Figure 7.4 XPS spectra of the Si $2p$ (Si-Si at 99 eV and Si-N at 102 eV) regions of the as-grown sample at 10 minutes. 96

Figure 7.5 AFM image showing the topography of the 5 min sample of an area of $1 \mu\text{m}^2$, (a) showing the surface with features identified as "hillock". The grain analysis shows the respective $\text{RMS} = 8.4 \pm 3.0 \text{ nm}$ roughness. In (b) show a 3D image of the film surface, (c) the height of the "hillock" of $\sim 68 \text{ nm}$, and (d) the histogram of the height distribution ranging from 20 to 70 nm, indicating the rapid promotion of this features. 97

Figure 7.6 AFM image showing the topography of the 20 min sample of an area of $1 \mu\text{m}^2$, (a) show total coverage of the substrate surface the grain analysis shows the respective $\text{RMS} = 3.7 \pm 1.6 \text{ nm}$ roughness. In (b) show a 3D image of the film surface. In (c) the histogram of the height distribution of the h-BN film ranging from 5 to 30 nm, the main lies on $10.8 \pm 0.3 \text{ nm}$. 98

Figure 7.7 Water droplets on bare Si and on the Si substrate coated with h-BN films at 10 min of growth time deposition. (a) bare Si - $\theta = 61.0^\circ \pm 1.0$, and (b) 5 min - $\theta = 101.0^\circ \pm 3.0$, (c) 10 min - $\theta = 105.0^\circ \pm 5.0$, and (b) 20 min - $\theta = 100.0^\circ \pm 1.0$. 99

Figure 7.8 Scanning electron microscopy (SEM) images of h-BN films grown at 1373 K are provided. (a-b) displays a 5-min grown sample exhibiting a circular pattern characterized by small aspect ratios, and features identified as "hillocks" with a brighter contrast (white). (c-d) displays a 10-min grown sample exhibiting a circular pattern and features and (e-f) depict the sample at 20-min showcasing a continuous and a coverage of the surface with the h-BN film. 101

Figure 7.9 Cross-section SEM image of h-BN film showing the hillock features with height of $\sim 300 \text{ nm}$ 101

Figure 7.10 Cross-section STEM image of h-BN film depicting an h-BN film, overlaid with a 100 nm thick platinum (Pt) coating, grown on a Si $\langle 100 \rangle$ substrate, following a 10-minute growth period at 1373 K. 102

Figure 7.11 The UV-Vis spectrum of h-BN films grown at 1373 K on a silicon substrate, the inset shows an analysis of the optical bandgap by applying the Tauc's equation. samples grown at (a) 5 min the E_g of 5.7 eV (b) 10 min E_g of 5.6 eV and (c) 20 min E_g of 5.7 eV.

List of tables

Table 4.1	FTIR - Bond Stretch assignments from Frueh <i>et al.</i> (2011) studies [19].	64
Table 4.2	Experimental parameters used in the deposition of h-BN films on Si substrate.	68
Table 6.1	Set of samples varying temperature and for tribology studies with growth conditions.	75
Table 6.2	Show the respective analysis parameter for the samples in the temperature range of 1273 to 1373 K. The FWHM values were used to estimate the crystallite sizes (L_a), and X_c is the peak position in cm^{-1} .	77
Table 7.1	The set of samples grown from 2 to 20 min and the growth conditions.	92
Table 7.2	Show the respective analysis parameter for the samples grown at 5, 10 and 20 minutes (1373 K). The FWHM values in cm^{-1} were used to estimate the crystallite sizes (L_a), and X_c is the peak position in cm^{-1} .	94
Table 7.3	Position of the B-N and N-B peaks in the B $1s$ and N $1s$ regions, respectively. And stoichiometric atomic ratio of B and N atoms obtained by area quantification, using the factor $RSF = 0.486$ (B) and $RSF = 1.8$ (N).	96

*Nothing is more honorable than a grateful
heart.*

Seneca, Lucius.

1

Introduction

Hexagonal Boron Nitride (h-BN) is a material analogous to graphene, featuring a honeycomb structure formed by its constituent atoms of Boron and Nitrogen [20, 21]. Within each h-BN layer, B and N atoms establish strong covalent bonds in the plane, whereas interlayer interactions are governed by Van der Waals forces reminiscent of graphite bonding [5].

Boron nitride (BN) exhibits different allotropic forms with bonding of sp^2 or sp^3 . In the case of sp^2 -bonded BN, it can adopt a hexagonal (h-BN) or rhombohedral (r-BN) phase, while sp^3 -bonded BN can crystallize in a cubic (c-BN) or wurtzite (w-BN) phase [22]. h-BN, as an insulator with a wide bandgap ranging from 4-6 eV [23, 24, 25, 26, 6], possesses properties such as chemical inertness, thermal conductivity, and good resistance to oxidation at elevated temperatures [27, 28, 29, 30].

These inherent characteristics make h-BN a promising candidate for various applications, including deep-ultraviolet (DUV) optoelectronics and high-power electronics, where h-BN films can serve as dielectric material in graphene-based electronics, solid-state thermal neutron detectors, and tunnel barriers in tunnel devices [31, 32, 33, 34, 35]. The h-BN nanocoatings have also demonstrated anticorrosion properties, i.e. can function as protective coatings because of their mechanical properties, including high hardness and toughness [35]. Furthermore, its hydrophobic nature limits the interaction of the substrate with corrosive media [35, 36].

Recent studies have revealed that h-BN, with its good lubricity, especially at high temperatures, is a promising alternative to other well-known solid lubricants such as graphite, which begins to oxidize at temperatures above 673 K. Similarly, MoS_2 , a member of the class of Transition Metal Dichalcogenides (TMDs), is easily oxidized when temperatures exceed 623 K, leading to the formation of MoO_3 . This oxidation increases the coefficient of friction (CoF) and wear rate, reducing its lubricity and limiting its effectiveness as a solid lubricant. The lubricating properties of h-BN are particularly due to its layered structure and high thermal conductivity, which promotes resistance to oxidation at high temperatures [37, 38].

Solid lubrication has become an integral part of materials science and engineering. Materials designed to reduce friction and wear are referred to as tribological materials. Some of the properties necessary for good lubricating performance in terms of mechanical and physical properties are strength, stiff-

ness, fatigue life, thermal expansion, and damping. In light of this, many efforts are being made to understand and design materials, including multilayer coatings and novel coating architectures that can adapt to varying environments [37].

The realization of these devices requires h-BN films with uniform thickness, coverage over large surface areas, and good crystallinity. For this purpose, various synthesis methods are employed, including mechanical exfoliation, molecular beam epitaxy, atomic layer deposition (ALD), ion beam sputtering deposition, cosegregation [39, 40, 41, 42, 43, 44, 45], and chemical vapor deposition (CVD). The CVD method, widely used for h-BN and other Van der Waals materials, offers advantages such as thickness and layer control, making it a candidate for industrial-scale h-BN growth processes. However, challenges persist, particularly in the growth of h-BN implementing polycrystalline metallic catalysts such as Ni, Co, Pt and Cu as substrates [46, 47, 48].

Precursors used for the growth of h-BN exist in various states, including gas (Diborane and Ammonia), liquid (Borazine), and solid (ammonia borane, trimethylamine borane, and oligomeric amine borane) [49]. The solid precursors offer advantages over those of liquid and gaseous precursors, particularly in terms of chemical stability, such as resistance to oxidation leading to the formation of borates, cost, and toxicity. For example, Ammonia Borane (BH_3NH_3) is employed as solids precursor, featuring a 1:1 ratio of B to N. They also exhibit significant benefits in terms of safe handling within the laboratory [50, 51]. Notably, some reports demonstrate the direct, transfer-free growth of h-BN thin films on silicon (Si)-based substrates, including Si_3N_4/Si and SiO_2/Si , as well as on $Si <001>$ [2, 52, 53]. This approach eliminates the need for substrate preparation, such as etching, polishing, high-temperature annealing, and the film transfer process, avoiding contamination of the CVD chamber. Despite these advances, synthesizing h-BN thin films essential for electronic, optoelectronic, or dielectric applications remains a challenge [22, 54].

In this context, we present an approach to synthesizing h-BN films on Si $<100>$ substrates utilizing a low-pressure chemical vapor deposition (LPCVD) system and the Ammonia Borane complex as a precursor. The variation of growth time is investigated to discern its role and impact on the process. Our experimental results, incorporating Raman spectroscopy, Infrared spectroscopy (FTIR), X-ray Photoelectron Spectroscopy (XPS), Atomic Force Microscopy (AFM), Scanning electron microscopy (SEM), and Ultraviolet-Visible (UV-VIS) spectroscopy, collectively provide evidence of the hexagonal phase of BN, the optical properties, protective capabilities, and morphological characteristics of h-BN films. This investigation offers insights into h-BN

growth dynamics and contributes to the evolving field of Van der Waals material synthesis and characterization.

This document is structured as follows. In Chapter 1 we present some previous work relevant to our problem. In Chapter 2 we show some properties and applications of h-BN films. In Chapter 3 we show the theoretical foundation. In Chapter 4 we show the methodology used to grow h-BN films. In Chapter 5 we show equipment and procedures for characterization. In Chapters 6 and 7 we present our results. Finally, in Chapter 8 we present our conclusions.

1.1

Aim and scope

In this thesis, our objective was to synthesize h-BN films using the LPCVD method. Initially, a bibliographical review was conducted to determine the best parameters for synthesizing the films with the materials and techniques available in the thin film at *Laboratório de Revestimentos Protetores e Materiais Nanoestruturados* at PUC-Rio. The literature extensively explores the synthesis of these films on various transition metal substrates such as Cu [27, 50, 5], Ni, Co, Pt, Fe, and Cu-Ni binary alloy substrates [55].

The h-BN films grown on copper foil requires transfer onto suitable substrates like SiO_2 for subsequent material analysis and device manufacturing. However, this additional transfer step poses challenges to the practical integration of CVD h-BN due to the inherent process intricacies and potential degradation in electrical properties resulting from defects or residues introduced during the transfer process. Given the disadvantages associated with the transfer process, it is crucial to explore alternative methods for nucleating h-BN layers directly on dielectric or insulating substrates, such as SiO_2/Si , Si_3N_4/Si , Al_2O_3 , and quartz.

Recently, there have been efforts to directly grow h-BN sheets on insulating or dielectric substrates such as SiO_2/Si , Si_3N_4/Si , silicon (111), quartz, sapphire, single crystal diamond, and 6H-SiC. These efforts utilize various techniques, including low-pressure thermal chemical vapor deposition (CVD) [56, 53, 57, 58, 1, 59], cold wall chemical vapor deposition, metal-organic chemical vapor deposition (MOCVD), molecular beam epitaxy (MBE), ion beam sputtering deposition (IBSD), metal-organic vapor phase epitaxy (MOVPE), and atomic layer deposition (ALD) [60].

Therefore, a deposition process capable of growing high-quality, ultra-smooth, transfer-free h-BN with controllable thickness directly on a variety of insulating and conductive substrates would be highly advantageous for the advancement of graphene and TMD technologies [61]. Consequently, this

thesis focuses on direct growth on silicon $\langle 100 \rangle$ substrates. By optimizing the CVD parameters for direct deposition on silicon, we aim to eliminate the complications associated with the transfer process and improve the quality and purity of the resulting films.

To comprehend the growth mechanism and achieve controlled growth of atomically thin to thicker films of h-BN, a systematic study on various essential CVD parameters was carried out. The effects of CVD parameters, such as substrate position, growth temperature, growth duration, sublimation temperature, and the weight of the AB precursor on h-BN nucleation and growth were methodically investigated.

Investigating the effects of these parameters is crucial for obtaining high-quality and uniform h-BN films. This comprehensive analysis aims to optimize the CVD process parameters to enhance the film's uniformity and quality. This approach seeks to advance the development of h-BN films suitable for various applications, particularly in optoelectronics and other fields requiring precise control over film morphology and properties.

1.2

State of the art

In this section, previous studies are discussed regarding the relevance of direct growth of h-BN on dielectric substrates, as well as the application of different synthesis parameters and methodologies.

Tay *et al.* (2015) demonstrated the growth of nanocrystalline h-BN (NCBN) films on dielectric substrates. Few to multi-layer NCBN films were directly grown on amorphous SiO_2/Si and quartz substrates in a CVD chamber using 30 mg of ammonia borane. Due to the non-self-limiting growth mechanism, the thickness of NCBN can be controlled by using different growth times; therefore, they controlled the thickness by adjusting the growth time between 5-30 minutes. The samples were characterized with various techniques. The left panel of Figure 1.1 shows their optical characterization of the h-BN film on the SiO_2 substrate, displaying a scratched region of the grown film exposing the underlying part of the substrate. The right panel shows a cross-sectional transmission electron microscope (TEM) image taken at the film edge of the sample grown for 5 minutes, with the interlayer distance in both films being 0.35 nm.

At 1273 K, borazine $(BNH_y)_x$ molecules are formed, enabling them to be deposited on any substrate. The starting BN layers initially grow parallel to the SiO_2 surface and thicken over time as more precursor gas (borazine) is supplied into the reaction. They observed that as the film thickens, it roughens

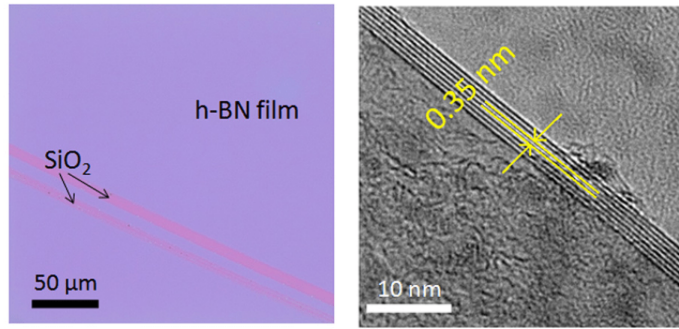


Figure 1.1: Left panel: Optical image of as-grown NCBN film on SiO_2 surface. Right panel: Cross-section TEM image showing 7 layers with interlayer distance of 0.35 nm for film grown for 5 min [1].

due to surface irregularities and multiple grain boundaries.

The crystallite sizes, extracted through the FWHM of Raman spectra, were found to be 23.0-24.9 nm. Additional evidence of the film thickness was obtained through Ultraviolet-visible (UV-vis) spectroscopy analysis, where NCBN films showed insulating properties with a wide bandgap ranging from 5.59 eV for thicker films of 17.5 nm to 6.03 eV for atomically thin films of 2.45 nm. After carrying out the characterizations on the films, they manufactured a device and conducted electrical measurements to confirm that the films do not conduct electricity. Figure 1.2 (Left panel) shows an optical image of the device, and the I-V plot for the NCBN indicates that the film is highly non-conductive (Right panel).

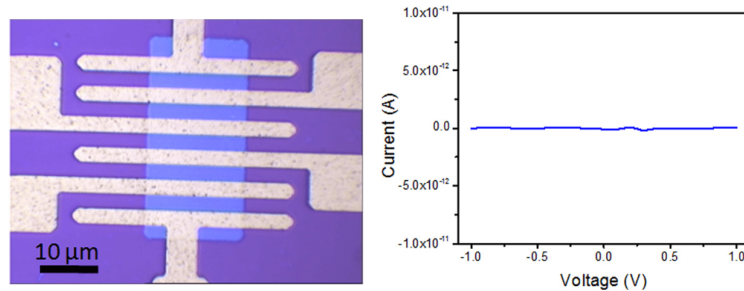


Figure 1.2: Left panel: Optical image of the manufactured device on a NCBN film. Right panel: I-V plot for the NCBN device, indicating the non-conducting properties of the films [1].

The transfer-free process allows for easy integration into large-scale manufacturing of BN with compatible Si-based technology and opens up other applications for thermally and chemically stable ultrathin non-conductive coatings.

Xi Chen *et al.* (2021) also intended to grow h-BN, but applying low-pressure CVD as a method with boron trichloride (BCl_3) and ammonia (NH_3) as precursors, the direct growth of h-BN films on Si <100> substrates was

attempted in a deposition temperature range of 1173-1573 K. They investigated the crystallinity of the as-grown h-BN films by X-ray diffraction (XRD), as a result the h-BN (0002) peak is present at about 26.7° , indicating an oriented growth along the c-axis perpendicularly to the substrate surface.

Including Raman spectroscopy, showing the dominant peaks at $1372\text{-}1382\text{ cm}^{-1}$, as shown in Figure 1.3 which can be assigned to the E_{2g} vibration mode of h-BN, also they observed a blue shift in the peaks that could be caused by the compressive stresses inside the h-BN films. Besides, E_{2g} mode were analyzed, they observed a sharpening with deposition temperature rise in the FWHM, indicating the samples' crystalline quality. Right panel Figure 1.3 shows the c-axis oriented h-BN films with a micrometer-scale thickness, about $2.3\text{ }\mu\text{m}$.

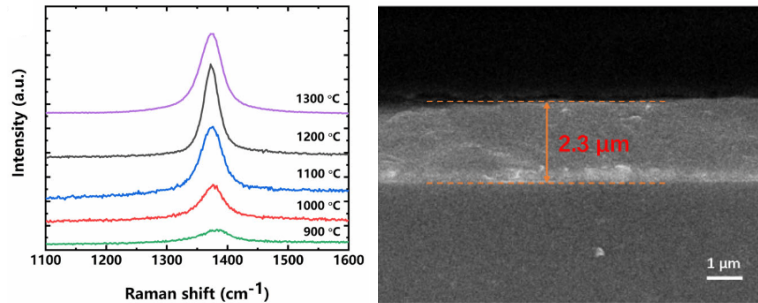


Figure 1.3: Left panel: Raman spectra of the h-BN samples grown on Si substrates by LPCVD at deposition temperatures range of 1173-1573 K. Right panel: cross sectional SEM images of h-BN films grown on the Si substrate at 1473 K [2].

They finally manufactured a DUV photodetector based on a $2.3\text{-}\mu\text{m}$ -thick h-BN film, whose on/off ratio is larger than 312 under the illumination of a UV-enhanced xenon lamp, Figure 1.4 (a) and (b) show the UV-vis absorption at 5.73 eV and the I-V curve of the h-BN and the schematic of the photodetector.

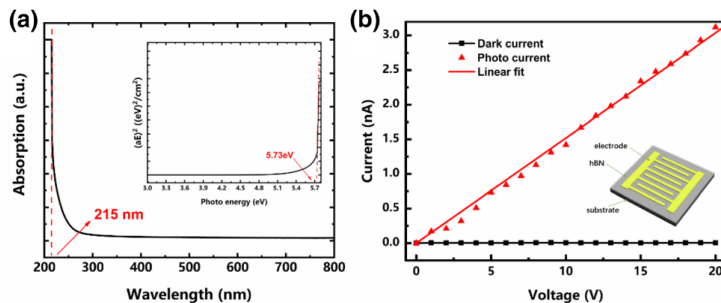


Figure 1.4: (a) UV-visible absorption spectrum, the inset is optical bandgap on a quartz substrate. (b) I-V characteristics of the h-BN photodetector ($2.3\text{ }\mu\text{m}$ thick) measured at room temperature in dark and under UV-enhanced, xenon lamp light irradiation, the inset shows the schematic of the photodetector [2].

2

Structure, Properties and Applications of h-BN

2.1

Structure

Figure 2.1 shows the h-BN atoms configuration of a layered structure along the c direction representing the layers interacting through the weak Van der Waals force, the length is 0.6661 nm , which makes it easier to slide the layers. In each layer, as shown in the right panel of Figure 2.1 B and N atoms are bonded by a covalent of sp^2 with bond length $\mathbf{a} = \mathbf{b} = 0.2504 \text{ nm}$, the \vec{a}_1 and \vec{a}_2 are vector of the unit cell for a monolayer [3, 62, 63, 64].

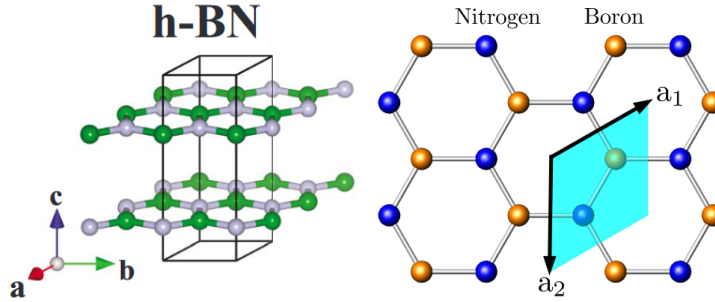


Figure 2.1: Left panel: Crystal structure of h-BN. Right panel: hexagonal structure of monolayer h-BN, showing the unit cell defined by the lattice vectors a_1 and a_2 [3, 4].

Li Song *et al.* (2010) conducted a study on h-BN films on Copper foils, as shown in Figure 2.2 (a-c) the high-resolution transmission electron microscopy (HRTEM) the edges of the films with 2 to 5 layers. The selected area electron diffraction (SAED), inset Figure 2.2 (a) confirms the hexagonal structure of the h-BN film, furthermore, the electron energy loss spectroscopy (EELS) spectrum Figure 2.2 (e) with two visible edges around 180 and 390 eV, proving that B and N are sp^2 hybridized.

In addition to the hexagonal phase, the three-dimensional bulk crystals of boron nitride (BN) include wurtzite BN (wz-BN), and zinc-blende BN (zb-BN) structures. The primitive unit cells of these structures are depicted in Figure 2.3.

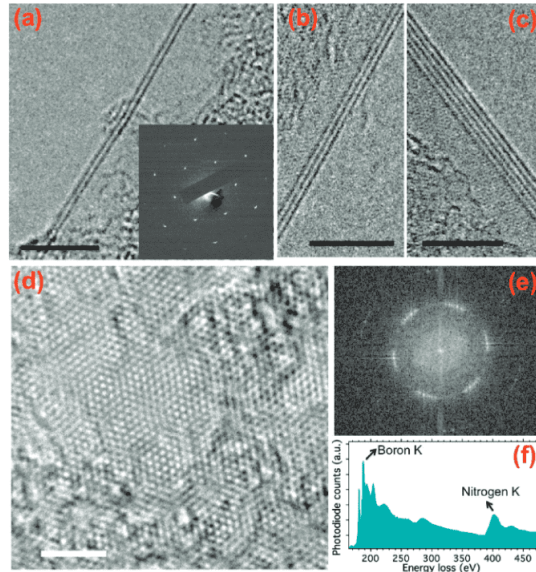


Figure 2.2: Microstructure of atomic layers hexagonal BN. (a-c) HRTEM images of the film edges, with two to five layers (scale bar 5 nm). The insert of (a) is the corresponding SEAD of the regions, (d) A typical atomic image of a h-BN films. The scale bars is 2 nm. (e) The fast Fourier transform pattern of a region of panel d, (f) EELS spectrum of a h-BN film [5].

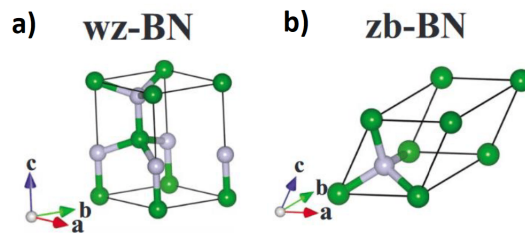


Figure 2.3: Crystal structure of (a) wurtzite (wz-BN); and (b) zinc-blende (zb-BN) crystals [3].

2.2 Properties

2.2.1 Electrical properties

h-BN exhibits a wide band gap, calculations by local density approximation (LDA) obtained bandgap of about 4.5 eV and GW of 6.0 eV [65] indicating that it belongs to the wide band gap class of semiconductors. B. Arnald *et al.* (2006) also calculated the electronic band structure, along the high-symmetry points of the Brillouin Zone (BZ) for bulk h-BN, by LDA (solid lines) and GW (open circles), as shown in Figure 2.4. The results obtained were an indirect band gap of 4.02 for LDA between the bottom of the conduction band (CB) and the top of the valence band (VB) at the M point and 6.04 for GW [6].

Figure 2.5 displays the theoretical band structure calculated along the

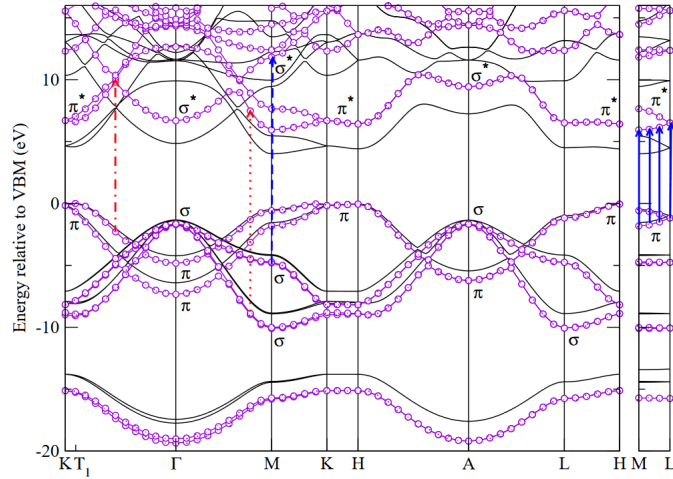


Figure 2.4: Phonon-dispersion curve of bulk h-BN calculated theoretically in the high symmetry points of Brillouin zone (BZ) [6].

points of the BZ for the monolayer h-BN. The energy band is opened at the bonding and antibonding $N-P_z$ and $B-P_z$ orbitals, therefore, the VB is projected mainly to the N-s and partly to N-p and B-s orbitals, and the CB is mostly due to N-p and partly B-p orbitals. Due to the electronegativity difference between B and N atoms, electrons are transferred from B to N this character dominates several properties of h-BN including the opening of the bandgap [3].

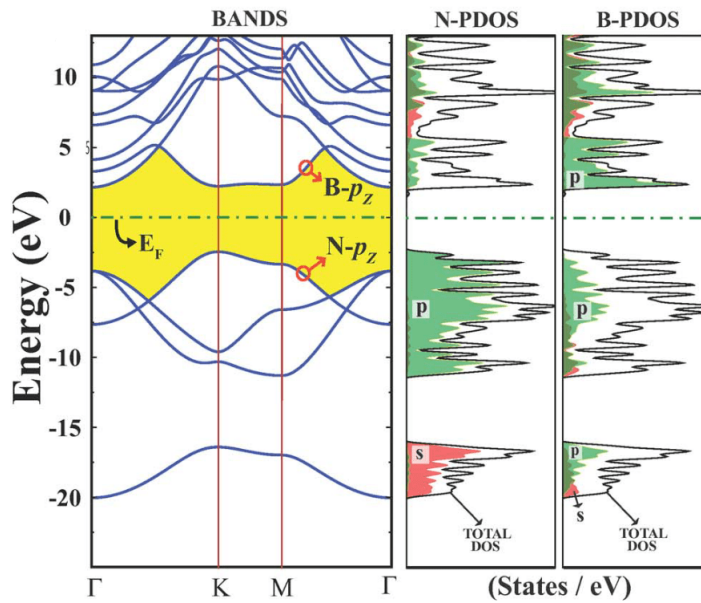


Figure 2.5: Left panel: band structure of monolayer h-BN calculated theoretically in the high symmetry points of Brillouin zone (BZ). Are indicated the Fermi energy E_F i. e., the zero of the energy, $B-P_z$ and $N-P_z$ orbitals [3].

Studies conducted by M. Topsakal *et al.* (2009) [3] obtained 12 phonons of bulk BN branches in the center of the BZ, using a primitive four-atom cell,

which allows the infrared (IR) and Raman active modes of 3D BN and h-BN at the Γ point. As a result, they found that h-BN belongs to D_{6h} (space group $P6/mmm$) point group, the irreducible representations at Γ are given by $2E_{2g} + 2B_{2g} + 2A_{2u} + 2E_{1u}$. Where the modes E_{1u} and E_{2g} are doubly degenerate, the modes B_{2g} and A_{2u} are nondegenerate. The modes E_{1u} and A_{2u} are IR active, the E_{2g} is Raman active. Finally, B_{2g} is an inactive mode.

In the 2D BN honeycomb structure, the unit cell comprises two atoms, resulting in three acoustic branches and three optical branches. The symmetry point group is D_{3h} (space group $P-62m$). The optical phonon modes at the Γ point are denoted by $A''_2 + 2E'$. The A''_2 mode is active in the infrared (IR), while the E' mode is active in both the IR and Raman.

2.2.2

Thermal Properties and Mechanical Strength

At room temperature, hexagonal boron nitride (h-BN) exhibits a thermal conductivity of up to 400 W/mK , which exceeds that of most metals and ceramic materials. h-BN displays typical anisotropic properties: it has a high thermal conductivity of 300 W/mK in the direction perpendicular to the c-axis, a low thermal expansion coefficient of $0 - 2.6 \times 10^{-4} \text{ K}^{-1}$, and a relatively high tensile strength of 41 MPa . In contrast, when aligned parallel to the c-axis, h-BN has a lower thermal conductivity of $20-30 \text{ W/mK}$ and exhibits high compressive strength.

Including, theoretical studies of the mechanical properties reveals that BN layers are extremely strong [66]. Song *et al.* (2010) conducted measurements on the mechanical properties of h-BN film using a diamond tip at the center of each membrane, as illustrated in Figure 2.6 (b). The equation determined the value of mechanical properties:

$$F = \sigma^{2D}(\pi a)(\delta/a) + E^{2D}(q^3 a)(\delta/a)^3 \quad (2-1)$$

Where F - is the applied force, the E^{2D} elastic constant, the σ^{2D} pre-tension in the film, and a - radius of well. The obtained value for elastic constant varying from 503 to 223 N/m for samples of thickness of 2.0 to 1.0 nm [5, 64].

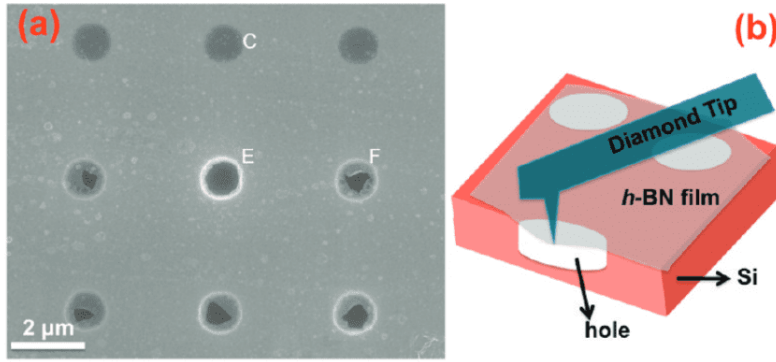


Figure 2.6: (a) Scanning Electron Micrograph of a Large h-BN film spanning an array of circular holes $1 \mu m$ in diameter, and (b) Schematic of nanoindentation performed on a suspended h-BN membrane [5].

2.2.3

Optical properties

Both experimental and theoretical calculations indicate that 2D h-BN has no absorption in the visible range but exhibits absorption spectroscopy in the ultraviolet region and demonstrates good photoluminescence properties.

The optical and fluorescence properties of h-BN have attracted considerable interest over the past decade, particularly since the first observation of intense far-UV exciton emission. This discovery has highlighted h-BN as a promising candidate for use in new light-emitting devices [67].

Studies conducted by Blase *et al.* (1995) theoretically predicted the bandgap for the bulk BN in hexagonal allotropic form as indirect and calculated to be 5.4 eV. And for h-BN monolayer sheet calculated to be 6.0 eV. The optical absorption properties, which are widely used to calculate the bandgap of semiconductors, can reflect the electronic state of materials. From experiments on h-BN the bandgap energy of the structures ranges from 3.6 to 7.1 eV [67, 64].

Figure 2.7 shows an absorption spectra measured by Song *et al.* (2010) of the h-BN film. The absorption peak around 223 nm , corresponds to a band gap energy of 5.56 eV. From the absorbance graphic, the optical bandgap can be calculated using Tauc's Equation 2-2 [68]. This expression is usually used for III-V semiconductors (wide bandgap) like h-BN. Hence, the absorption coefficient adopts the form [69],

$$\alpha = C \frac{(h\nu - E_g)^{1/2}}{h\nu} \quad (2-2)$$

Where C is the proportionality constant, $h\nu$ is the energy of an incident photon, while E_g expresses the energy of the optical bandgap.

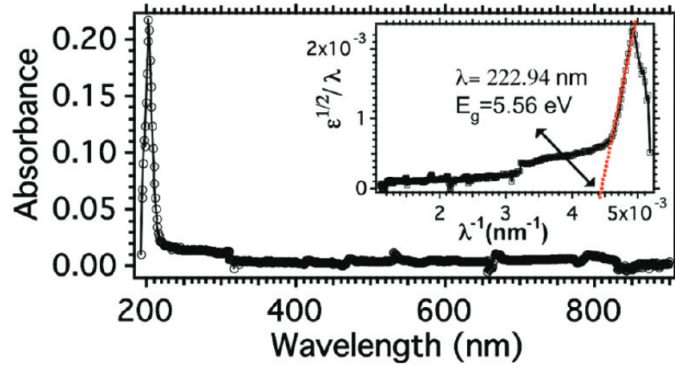


Figure 2.7: Typical ultraviolet-visible absorption spectra of h-BN film [5].

2.3

Applications

2.3.1

Substrate to other materials

h-BN has been recognized as a good substrate for graphene, molybdenum disulfide, and other two-dimensional (2D) nanomaterials, and the performance of these 2D materials has been improved, therefore, attracting much attention. The interest arises primarily because of h-BN's atomically flat surface, which is free of dangling bonds or charge traps. The heterojunction of graphene/h-BN structures exhibits high mobility and negligible intrinsic doping, leading to significant improvements in the switch of the device more than graphene under SiO_2 (graphene/ SiO_2) substrate. In addition, the graphene/h-BN heterostructure serves as a valuable material for studying the intrinsic mechanical properties of graphene [70].

Lee *et al.* (2012) utilized chemical vapor deposition (CVD) to prepare h-BN nanosheets, which were subsequently used as substrates to fabricate thin film transistors with graphene. The device is illustrated in Figure 2.8. The presence of h-BN significantly enhances the performance of the transistors. Specifically, the electron mobility and drain current switching ratios are three times higher ($573 \text{ cm}^2\text{s}^{-1} \text{ V}^{-1}$ at $-2 \times 10^{11} \text{ cm}^{-2}$) compared to transistors without the h-BN substrate [7, 70].

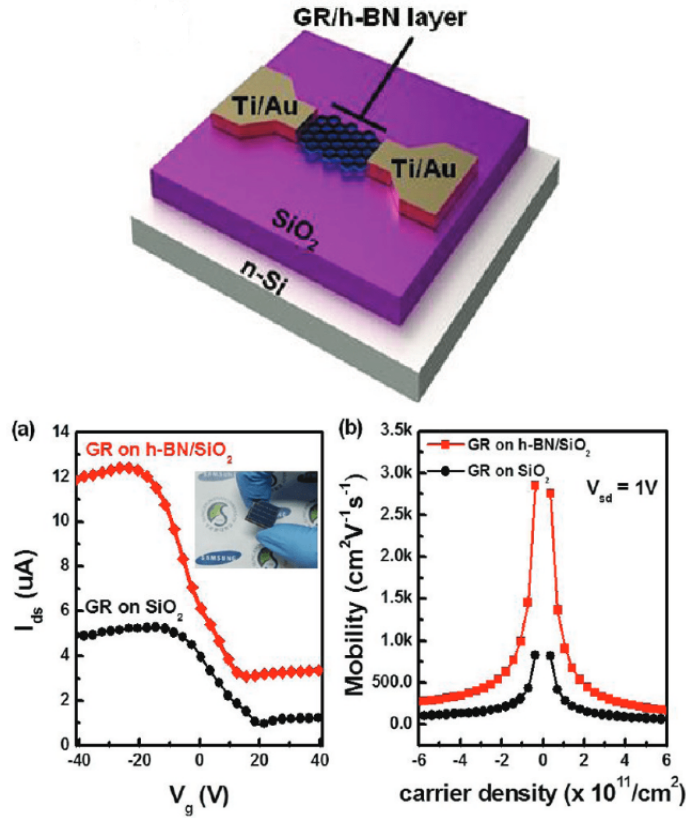


Figure 2.8: Schematic of graphene (GR) device structure with grown h-BN nanosheets [7]. The mobility of charge carriers in graphene as a function of carrier density.

2.3.2

Field-effect transistors with h-BN.

h-BN plays a crucial role in packaging various other two-dimensional materials. Chuang et al. designed a high-performance Field Effect Transistor (FET) based on p-doped $WSe_2(Nb_{0.005}W_{0.995}Se_2)$ 2D drain/source electrodes in contact with an undoped 2D WSe_2 channel. To maintain the inherent electrical characteristics of the channel material, the layers were encapsulated with h-BN, as shown in Figure 2.9 [70]. The devices were fabricated by stacking the mechanically exfoliated flakes of the 2D TMDs, the p-doped TMDs, were used as electrodes placed on top of an undoped TMD channel material using a dry transfer method. The gate dielectric consists of 40 nm thick h-BN on 280 nm thick SiO_2 .

The FETs show low contact resistances of about $0.3 k\Omega\mu m$, high on/off ratios of above 10^9 , and drive currents of above $320 \mu A\mu m^{-1}$ [8, 70]. The requirement of high- κ gate dielectrics is becoming essential as the scaling of transistors results in unacceptable levels of gate leakage current. The insertion of h-BN as gate dielectric was observed to result in a reduction in the subthreshold swing (SS), from $460 mV/dec$, to the near-ideal value of 63

mV/dec . In a classical FET the subthreshold swing is limited by diffusion of charge carriers, and is a feature of a MOSFET's current–voltage characteristic [8].

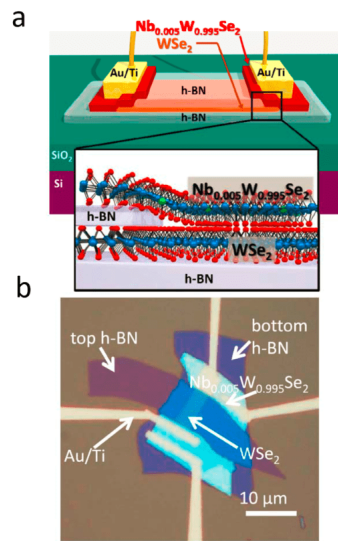


Figure 2.9: (a) Design and Characteristics of a high performance Field-Effect Transistor (FET) based on WSe_2 with contacts made of 2D/2D, and (b) depict the optical micrograph encapsulation of the channel region in h-BN from Both top and bottom within the device [8].

2.3.3

Tribological and lubricant material

B. Padgornik *et al.* (2014) [71] studied the tribological behavior and lubrication performance of h-BN as a possible material to replace graphite in aluminum forming. In metal-forming processes, friction causes issues such as heat generation, adhesion, and tool wear, therefore, poor surface quality, requiring the use of suitable lubricants, especially for aluminum and its alloys. Forming lubricants are required to provide temperature stability, reduce friction, prevent galling, and surface protection. Graphite is an effective solid lubricant for aluminum forming but leaves dark stains, requiring extra polishing. Tests with h-BN powder with three different particle sizes of 0.5, 5.0, and 30 μm showed that the best performance was obtained with the 30 μm particle size and higher concentration, demonstrating good lubricant stability of h-BN and improved surface quality of the formed part.

2.3.4

Corrosion prevention material

Ventaka *et al.* (2023) [72] studied the corrosion prevention of iron substrates, which are vulnerable to corrosion when exposed to aggressive environments such as acidic and salty conditions. These effects cause structural failures and reduce the lifetime of components. One way of preventing metallic surface corrosion is through protective coatings. They focused on using PLD as a nanoscale manufacturing method for obtaining protective, corrosion-resistant h-BN coatings directly on Fe substrates. Their primary goal was to investigate the effects of deposition temperatures on the film microstructure and its related corrosion properties of h-BN coatings on Fe substrates. Additionally, the influence of h-BN coating thickness on corrosion properties was also examined. They confirmed the presence of h-BN phase in the deposited coatings by Raman, GIXRD, and TEM analysis. Electrochemical studies revealed that the h-BN coated Fe substrates made at 600°C showed better barrier properties with lower corrosion rates. The corrosion rates decreased with an increase in h-BN coating thickness from 35 nm to 115 nm. The corrosion inhibition efficiency of Fe was improved by 82% with the deposition of a 115 nm thick h-BN coating. Therefore, the h-BN nanocoatings can serve as protective barrier coatings in aggressive environments and can potentially be used for various material coating applications.

3 Theoretical Background

In this chapter, fundamental theoretical aspects of the characterization techniques used to analyze h-BN films are discussed.

The focus will be on providing a comprehensive understanding of the methodologies employed to investigate the chemical, structural, tribological, and optical properties of hexagonal boron nitride (h-BN) films. This includes an in-depth examination of various analytical techniques such as, Raman spectroscopy, Fourier-Transform Infrared Spectroscopy for molecular and structural analysis, scanning electron microscopy (SEM) for surface morphology characterization.

In addition, the chapter will cover atomic force microscopy (AFM) to study surface topography and morphology, as well as tribological testing to evaluate the wear resistance and frictional behavior of the films. Optical properties will be explored using techniques such as ultraviolet-visible (UV-vis) spectroscopy to understand potential applications of the films in optoelectronics.

Theoretical background and principles behind each technique will be discussed, the relevance and significance of the obtained data in the context of material science and engineering. To provide a solid foundation for the characterization of h-BN films synthesized through chemical vapor deposition (CVD). This knowledge is essential for advancing the development and application of these films in various technological fields.

3.1 Fundamentals concepts about Raman Scattering

This section deals with a brief and simplified description of the theory of Raman scattering. We begin with a discussion of the classical followed by the quantum mechanical formalism. A short literary discussion on Raman spectra in h-BN is also shown.

3.1.1 The classical formalism of macroscopic Raman scattering

The Raman effect, discovered in 1928 by the Indian physicist C.V. Raman demonstrated that the visible wavelength of a small fraction of radiation scattered by certain molecules differs from that of the incident radiation.

Raman was awarded the Nobel Prize in Physics in 1930 for his systematic investigation of this phenomenon.

When light interacts with a medium, various processes, such as transmission and reflection, can occur. However, only a small fraction of the incoming light is scattered due to the inhomogeneities of the medium. These inhomogeneities may be static or dynamic. These scattering processes can be either elastic, where there is no change in wavelength, or inelastic, caused by atomic vibrations that result in changes in wavelength.

Raman spectroscopy is the technique employed to study the inelastic scattering of light from a medium. This scattering is produced by the interaction of light with the same excitation. In a Raman experiment, we measure the shift in energy between the incoming and inelastically scattered light.

The macroscopic theory of Raman scattering elucidates the interactions between light and matter, giving rise to a polarization vector. This theory contemplates an infinite crystalline medium at finite temperature, characterized by dielectric susceptibility χ , which represents polarizability. The induced electric dipole resulting from these interactions can be expressed in terms of the electric field \mathbf{E} of the incident light on the medium as follows [73]:

$$\mathbf{P} = \chi \cdot \mathbf{E} \quad (3-1)$$

In this context, the electric field associated with the incident radiation is expressed as a plane wave, denoted as $\mathbf{E}(\mathbf{r}, t)$, with amplitude $\mathbf{E}_0(\mathbf{K}_i, \omega_i)$:

$$\mathbf{E}(\mathbf{r}, t) = \mathbf{E}_0(\mathbf{K}_i, \omega_i) \cos(\mathbf{K}_i \cdot \mathbf{r} - \omega_i t) \quad (3-2)$$

The polarizability tensor, denoted as χ , should also depend on the atomic vibrations of the medium, as the atomic positions change over time. To describe the variations in χ resulting from atomic motion, we assume that the amplitudes of atomic vibrations at room temperature are much smaller than the lattice constant of the medium. Consequently, the elements of the matrix of can be expanded as a function of the generalized coordinate of a specific vibration mode, $\mathbf{Q}(\mathbf{r}, t)$, in a Taylor series.

$$\chi(\mathbf{K}_i, \omega_i, \mathbf{Q}) \approx \chi_0(\mathbf{K}_i, \omega_i) + \left(\frac{\partial \chi}{\partial \mathbf{Q}} \right) \Big|_0 \mathbf{Q}(\mathbf{r}, t) + \dots \quad (3-3)$$

Combining Equation 3-1, 3-2, and 3-3, we obtain the following equation:

$$\mathbf{P}(\mathbf{r}, t, \mathbf{Q}) \approx \mathbf{P}_0(\mathbf{r}, t) + \mathbf{P}_{ind}(\mathbf{r}, t, \mathbf{Q}) + \dots \quad (3-4)$$

Where $\mathbf{P}_0(\mathbf{r}, t)$ is the polarization vector oscillating with the same frequency as that of the incident radiation, leading to the so-called Rayleigh scattering (or elastic scattering). $\mathbf{P}_{ind}(\mathbf{r}, t, \mathbf{Q})$ represents the polarization induced by the vibration of the atoms. To obtain $\mathbf{P}_{ind}(\mathbf{r}, t, \mathbf{Q})$, a plane wave will

be introduced to describe the quantized atomic displacement $\mathbf{Q}(\mathbf{r}, t)$, referred to as the normal mode of vibration, which is given by:

$$\mathbf{Q}(\mathbf{r}, t) = \mathbf{Q}(\mathbf{q}, \omega) \cos(\mathbf{q} \cdot \mathbf{r} - \omega_0 t) \quad (3-5)$$

Inserting Equation 3-5 into 3-4 and employing the trigonometric relation for cosines. The $\mathbf{P}_{ind}(\mathbf{r}, t, \mathbf{Q})$ term becomes:

$$\mathbf{P}_{ind}(\mathbf{r}, t, \mathbf{Q}) = \frac{1}{2} \left(\frac{\partial \chi}{\partial \mathbf{Q}} \right) \Big|_0 \mathbf{Q}(\mathbf{q}, \omega_0) \mathbf{E}_0(\mathbf{K}_i, \omega_i) \cdot \left\{ \cos((\mathbf{K}_i + \mathbf{q}) \cdot \mathbf{r} - (\omega_i + \omega_0)t) + \cos((\mathbf{K}_i - \mathbf{q}) \cdot \mathbf{r} - (\omega_i - \omega_0)t) \right\} \quad (3-6)$$

The equation $\mathbf{P}_{ind}(\mathbf{r}, t, \mathbf{Q})$ consists of two sinusoidal waves: a Stokes-shifted wave with wave vector $\mathbf{K}_S = \mathbf{K}_i - \mathbf{q}$ and frequency $\omega_S = \omega_i - \omega_0$, and an anti-Stokes-shifted wave with wave vector $\mathbf{K}_{AS} = \mathbf{K}_i + \mathbf{q}$ and frequency $\omega_{AS} = \omega_i + \omega_0$. The radiation produced by these two induced polarization waves is known, respectively, as Stokes-scattered and anti-Stokes-scattered light (Figure 3.1). Since the phonon frequency equals the difference between the incident-photon frequency and the scattered-photon frequency, this difference is called the Raman frequency or Raman shift (one also speaks of Stokes and anti-Stokes shifts). Raman spectra are typically plots of the intensity of the scattered radiation versus the Raman frequency.

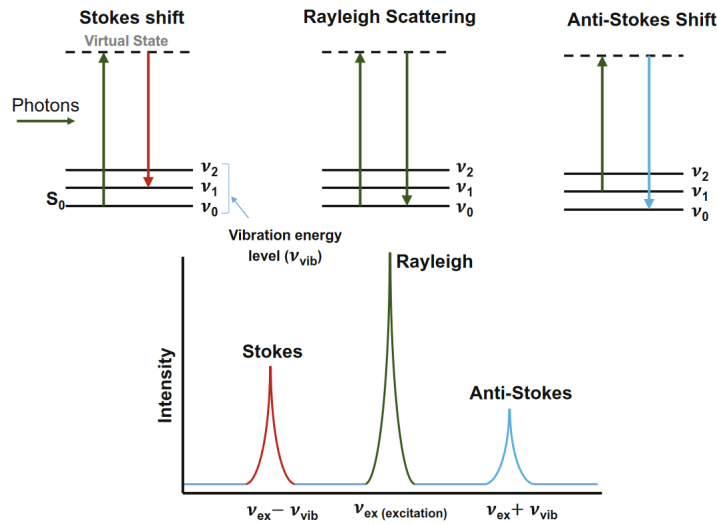


Figure 3.1: Rayleigh scattering, Stokes Raman and anti-Stokes Raman scattering [9].

3.1.2

The Quantum formalism of Microscopic Raman scattering

The microscopic theory involving one-phonon Raman scattering can be briefly described in three steps:

- i. An incoming photon is absorbed by the medium, creating an electron-hole pair.
- ii. The electron-hole pair undergoes inelastic scattering to another state by either emitting (Stokes process) or annihilating (anti-Stokes process) a phonon.
- iii. The electron-hole pair recombines radiatively back to the ground state by emitting a photon.

In this process, the electron acts only as an intermediate state, and all electronic transitions are considered virtual. The initial and final electronic states are assumed to be the ground state.

The quantum mechanical treatment of Raman scattering can be illustrated in light of the Feynman diagram for a Stokes process (Figure 3.2). This diagram consists of three vertices, each representing a first-order time-dependent perturbation in the system. The first vertex depicts the initial state $|i\rangle$ of the system transitioning to an excited state $|n\rangle$ due to electron-radiation interaction. In the second vertex, the state $|n\rangle$ of the system progresses to the state $|n'\rangle$ through an electron-phonon interaction. In the third and final vertex, there is a recombination of the electron-hole pair, and the system reaches the final state $|f\rangle$ [73].

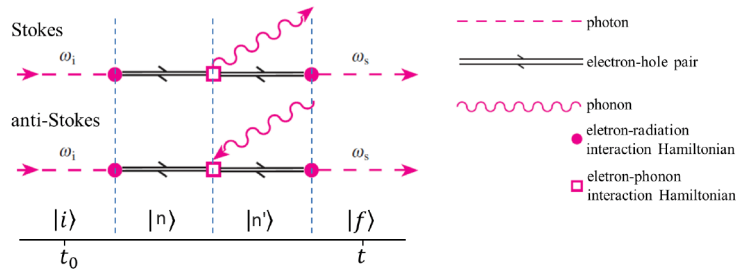


Figure 3.2: Schematic representation of Feynman diagrams for one-phonon Stokes and anti-Stokes scattering and the symbols used in drawing Feynman diagrams [10].

In the first vertex, there is an absorption of a photon with energy $\hbar\omega_i$; in the second vertex, there is an emission of a phonon with energy $\hbar\omega_{ph}$, and in the last vertex, there is an emission of a photon with energy $\hbar\omega_S$. These four states of the system can be defined as:

$$|i\rangle = |P_i, 0, P_{ph}, \psi_0\rangle$$

$$|n\rangle = |P_i - 1, 0, P_{ph}, \psi_e^h\rangle \quad (3-7)$$

$$|n'\rangle = |P_i - 1, 0, P_{ph} - 1, \psi_e^{h'}\rangle \quad (3-8)$$

$$|f\rangle = |P_i - 1, 1, P_{ph} - 1, \psi_0\rangle \quad (3-9)$$

The four terms inside the brackets represent the number of incident photons, the number of scattered photons, the number of phonons, and the electronic state, respectively. The energies associated with these states are given by:

$$E_i = P_i \hbar \omega_i + P_{ph} \hbar \omega_{ph} + E_v$$

$$E_n = (P_i - 1) \hbar \omega_i + P_{ph} \hbar \omega_{ph} + E_c^n \quad (3-10)$$

$$E_{n'} = (P_i - 1) \hbar \omega_i + (P_{ph} - 1) \hbar \omega_{ph} + E_c^{n'} \quad (3-11)$$

$$E_f = (P_i - 1) \hbar \omega_i + \hbar \omega_S + (P_{ph} - 1) \hbar \omega_{ph} + E_v \quad (3-12)$$

In this context, E_v and E_c represent the energy levels of valence and conduction, respectively. The phenomenon is often depicted using a Feynman diagram representation. However, it's essential to note that the horizontal lines in this depiction do not signify the electronic energy levels of the system.

$$\sum_n \frac{\langle n | H_{light} | i \rangle}{\hbar \omega_i - (E_c^n - E_v)} \quad (3-13)$$

To calculate the Raman scattering probability for the process, it is necessary to consider the first vertex, which contributes with a first-order perturbation term.

$$\sum_{n,n'} \frac{\langle n' | H_{el-ph} | n \rangle \langle n | H_{light} | i \rangle}{[\hbar \omega_i - (E_c^n - E_v)][\hbar \omega_i - \hbar \omega_{ph}(E_c^{n'} - E_v)]} \quad (3-14)$$

When we multiply the first vertex, associated with the electron-phonon interaction, by the second vertex, we arrive at a second-order term expressed as:

$$\sum_{n,n'} \frac{\langle f | H_{light} | n' \rangle \langle n' | H_{el-ph} | n \rangle \langle n | H_{light} | i \rangle}{[\hbar \omega_i - (E_c^n - E_v)][\hbar \omega_i - \hbar \omega_{ph}(E_c^{n'} - E_v)][\hbar \omega_i - \hbar \omega_{ph} - \hbar \omega_S]} \quad (3-15)$$

Finally, we multiply this last equation by the third vertex, which contributes to the emission of a photon. Consequently, we obtain:

$$P_{Raman} = \left(\frac{2\pi}{\hbar} \right) \left| \sum_{n,n'} \frac{\langle f | H_{light} | n' \rangle \langle n' | H_{el-ph} | n \rangle \langle n | H_{light} | i \rangle}{[\hbar\omega_i - (E_c^n - E_v)] [\hbar\omega_i - \hbar\omega_{ph} (E_c^{n'} - E_v)]} \right|^2 \delta(\hbar\omega_i - \hbar\omega_{ph} - \hbar\omega_S) \quad (3-16)$$

Here $|n\rangle$ and $|n'\rangle$ are virtual states with E_n and $E_{n'}$ energy. This equation is Fermi's golden rule for a first-order Raman process.

3.1.3

Raman Spectroscopy signature on hexagonal Boron Nitride (h-BN)

As mentioned above, Raman spectroscopy is employed to identify the lattice vibration frequencies of materials. For h-BN layers, it is reported peaks ranging between 1364 and 1370 cm^{-1} correspond to the E_{2g} phonon mode. It has been observed that, for atomically thin h-BN, the intensity of this peak is directly proportional to the number of layers (Figure 3.3). In the case of monolayer h-BN, the peak is blue shifted due to hardening of the E_{2g} phonon, which results from shorter B-N bonds and indicates compressive stress caused by the stretching of the film [11].

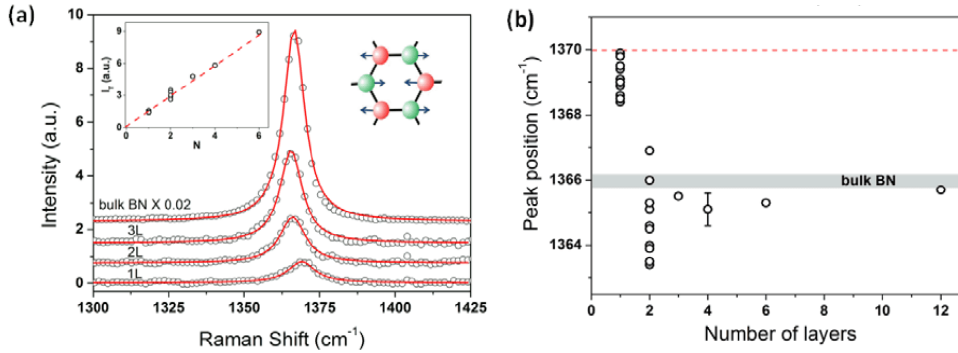


Figure 3.3: Raman spectra of h-BN film: (a) Raman spectra of h-BN films with different thicknesses. The inset shows a plot of Raman peak intensity against the number of h-BN layers. (b) A plot of Raman peak position versus the number of h-BN layers [11].

In contrast, in bilayer h-BN, a red shift of approximately 2 cm^{-1} is observed, attributed to random strain induced during cleavage. The variations in the peaks observed for monolayer ($1368 - 1370 \text{ cm}^{-1}$) and bilayer ($1363 - 1367 \text{ cm}^{-1}$) h-BN, as depicted in Figure 3.3(b), are reported to be caused by differences in the strain of the film [11].

3.2

Fourier-Transform Infrared Spectroscopy

When an molecule is irradiated with an infrared light, the absorption occurs under certain conditions. The energy $h\nu$ of the infrared light is equal to the

difference of energy between a vibrational energy level of the molecule such as the energy E_m and another energy level of vibration of the molecule with an energy E_n (Figure 3.4). As given in the form of the following equation,

$$h\nu = E_m - E_n \quad (3-17)$$

This means that the absorption of infrared light occurs because of a transition between energy levels of molecular vibration. For that reason, an infrared absorption spectrum is a vibrational spectrum of a molecule.

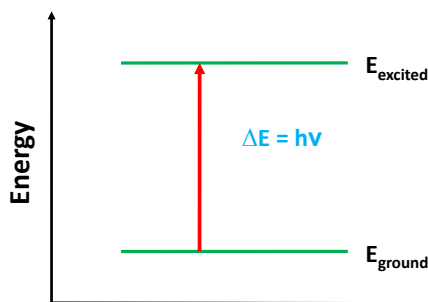


Figure 3.4: Absorption of electromagnetic radiation.

The absorption of infrared light is governed by selection rules; therefore, transitions that are considered allowed are due to a change in the vibrational quantum number by ± 1 and other transitions are forbidden transitions [74].

Another selection rule consider the symmetry of the molecule. This selection rule states that infrared light is absorbed when the electric dipole moment of a molecule changes in accordance with a molecular vibration.

According to quantum mechanics theory a transition between two states m to n by absorbing or emitting infrared light is expressed as,

$$(\mu_x)_{mn} = \int_{-\infty}^{\infty} \Psi_n \mu_x \Psi_m dQ \quad (3-18)$$

Also by $(\mu_y)_{mn}$ or $(\mu_z)_{mn}$ relative to the y and z components of the electric dipole moment which are represented by a similar equation. Where μ_x is the x component of the electric dipole moment, Ψ the eigenfunction of the molecule in its vibrational state, and Q is the normal coordinate or a normal vibration. Normal vibrations are vibrations of nuclei within a molecule, and translational motions and rotational motions of the molecule are not included in normal vibrations.

A given distribution of electrons in the ground state should also depend on the atomic vibrations of the medium, since the atomic position change over time. Therefore, the matrix elements can be expanded as a function of the generalized coordinate Q in a Taylor series by,

$$\mu_x = (\mu_x)_0 + (\partial\mu_x/\partial Q)_0 Q + \frac{1}{2}(\partial^2\mu_x/\partial Q^2)_0 Q^2 + \dots \quad (3-19)$$

Replacing Equation 3-19 in Equation 3-18, considering that the normal vibration term Q has a small value, we can neglect the higher order terms. Therefore, we have:

$$(\mu_x)_{mn} = (\mu_x)_0 \int \Psi_n \Psi_m dQ + \left(\frac{\partial\mu_x}{\partial Q} \right)_0 \int \Psi_n Q \Psi_m dQ \quad (3-20)$$

The first term refers to the magnitude of the permanent dipole of the molecule, and is 0 due to the orthogonality of the eigenfunction or \neq of 0 if $m = n$. The second term, both $(\partial\mu_x/\partial Q)$ and $\int \Psi_n Q \Psi_m dQ$ must be \neq of 0 to satisfy the two selection rules. So the first selection rule is satisfied when $n = m \pm 1$, and the second one that is related with the symmetry of a molecule where $(\partial\mu_x/\partial Q) \neq 0$ indicates that infrared absorption occurs only when certain vibration changes the electric dipole moment. A molecule that is infrared active must undergo a change in its dipole moment when vibrating. Then, the simplest modes of vibration that are infrared active are stretching and bending modes [74].

Because most molecules are in the ground state at room temperature, a transition from the state $\nu'' = 0$ to the state $\nu'' = 1$ (the first excited state) is possible. The absorption corresponding to this transition is called fundamental. Although most bands observed in infrared absorption spectra arise from the fundamental transition, bands corresponding to transitions from the state to higher excited states, known as overtone transitions, can also be found. However, since overtones are forbidden, the resulting bands are very weak.

The horizontal and vertical axes of an infrared absorption spectrum need explanation. The horizontal axis represents frequency, indicated in units of wavenumber (cm^{-1}), with higher wavenumbers always on the left-hand side. The vertical axis represents either transmittance T (%). While infrared spectra primarily include absorption spectra, they can also encompass reflectance and emission spectra [74].

Infrared spectroscopy can be utilized not only for the identification of functional groups but also for investigating the chemical bonds and the environment surrounding these functional groups. Infrared spectroscopy may be used for non-destructive analysis of a sample. It is applicable to a sample in various states, e.g., solid, crystal, fibre, film, liquid, solution, and gas.

3.3 X-ray Photoelectron Spectroscopy

Initially called electron spectroscopy for chemical analysis (ESCA), it is an experiment that involves the emission of photoelectrons when a light source impinges a given material, currently known as X-ray Photoelectron Spectroscopy (XPS). The discovery of this phenomenon was attributed to Hertz in 1887; in the following years, the experiment underwent improvements, whereas the explanation only came in 1905 after Einstein clarified the quantum nature of light. It later came to be called XPS, attributed to Kai Siegbahn as an analytical tool, who received the Nobel Prize in 1981 "for his contribution to the development of high-resolution electron spectroscopy" [12].

In the late 1960s to early 1970s, commercial XPS instruments emerged, owing to the establishment of standardized techniques for achieving Ultra-High Vacuum (UHV) conditions. Since then, XPS has been frequently used as an analytical method to investigate the surface characteristics of solid specimens. The ability of XPS to determine the chemical composition and elemental chemical states makes it a significant analytical tool in diverse fields such as microelectronics, metallurgy, heterogeneous catalysis, polymer technology, and corrosion science [75].

The basic principle of XPS lies in the fact that photons are used to ionize the surface of a sample, resulting in the ejection of photoelectrons whose energy can be measured; this phenomenon is called the photoelectric effect.

Figure 3.5 illustrates the physical principles of the photoemission process. Show the energy-level diagram and the energy distribution of a metal.

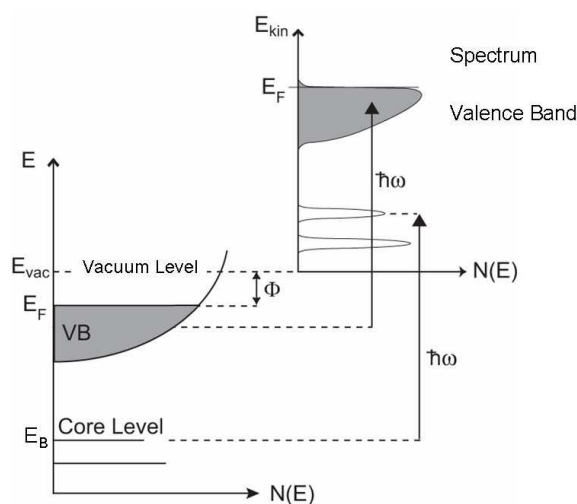


Figure 3.5: Shows the relation of the electronic states density in the sample onto the distribution of kinetic energy of the photoelectrons. Electrons in occupied states are detectable once they are excited above the vacuum level by electrons with energy $\hbar\omega$ [12].

The Fermi energy E_F (The Fermi level corresponds to the zero value in the binding energy) is at the top of the valence band, and the ϕ is a separation between the vacuum level E_{vac} and E_F .

Therefore, the emitted electrons have kinetic energies E_K given by:

$$E_K = h\nu - E_B - \phi_s \quad (3-21)$$

Where $h\nu$ represents the energy of the X-ray quantum, E_B denotes the binding energy of the core level, and ϕ_s spectrometer work function.

The fundamental components of an XPS instrument comprise a light source, an electron energy analyzer, and an electron detector, as shown in Figure 3.6. Commonly X-ray source are used to irradiate samples beams of Mg K_α (1253.6 eV) or Al K_α (1486.6 eV).

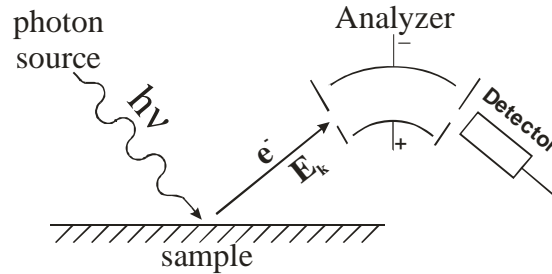


Figure 3.6: Basics components of XPS experiment, include photon source, sample to be analyzed, analyzer and a detector [12].

An electron energy analyzer is used with the purpose of measuring the energy of emitted photoelectrons. Through the analysis of the binding energy and intensity of a photoelectron peak, one can determine the elemental identity, chemical state, and quantity of the detected element.

During the early stages of XPS development, magnetic-electron energy analyzers were employed. However, they were eventually replaced by electrostatic analyzers. Among various types of electrostatic analyzers, such as the retarding field analyzer, cylindrical mirror or deflection analyzers, and the hemispherical analyzer, the latter is extensively utilized in modern XPS applications. This preference is attributed to the superior resolution characteristics offered by hemispherical analyzers [75].

Figure 3.7 show the electrons initially with kinetic energy E_{K0} , which are in the detection path, undergo deceleration or acceleration by electrostatic lenses to reach the analyzer pass energy E_p and are focused onto the inlet slit. The difference of voltage across the hemispherical electrodes determines the selection of electrons with kinetic energy E_p . Consequently, photoelectrons are registered within a narrow kinetic energy range, the width of which defines the resolution of the analyzer.

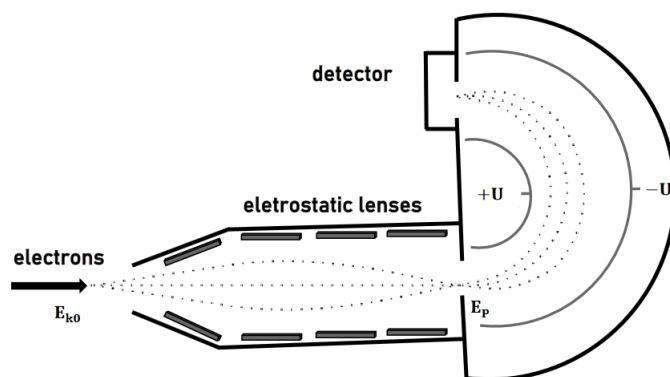


Figure 3.7: A hemispherical electron energy analyzer of XPS instruments.

To generate a spectrum, voltages are swept across the electrostatic lenses and hemispherical electrodes. Electron detection commonly employs an electron multiplier of the channeltron type, along with electronic devices operating in pulse counting mode [12].

3.3.1 Survey spectra of h-BN

The XPS survey spectra are usually applied as primarily way of surface analysis, providing a comprehensive overview of elemental composition and chemical states within a sample. The spectra typically cover a broad energy range, often from 0 to 1200 eV, allowing the detection of core-level peaks corresponding to various elements, for example carbon (C), oxygen (O), nitrogen (N), silicon (Si), and others, which depend on the nature of the sample. Some of the peaks are inherent to the technique, others depend on the chemical and physical nature of the samples, and some arise from instrumental effects. To acquire spectra, certain parameters are crucial, such as pass energy, energy step size, and integration time. These parameters are directly associated to the resolution, intensity, and signal-to-noise ratio of the spectra. For example a higher pass energy, around 50 to 150 eV, is used for survey spectra. This setting sacrifices resolution for faster data acquisition and improved signal-to-noise ratio.

Including, the energy step size which determines the resolution of the spectrum indicating a larger energy step size is acceptable due to the focus on overall elemental composition rather than fine details, and the integration time, longer integration times are employed to enhance the signal intensity/counts and reduce noise, especially for elements at lower concentrations.

Figure 3.8 The typical survey spectra of an h-BN sample exhibit distinct peaks indicative of the elemental composition present. Elements such as B, C, N, and O are commonly observed. However, it is essential to consider

the behavior of photoelectrons after their escape from an atom within the solid. Upon escape, a photoelectron travels a certain distance before reaching the vacuum or undergoing relaxation processes. Therefore, the electron may undergo elastic or inelastic collisions with lattice atoms.

Elastic collisions do not alter the kinetic energy of the electron, whereas inelastic collisions result in a decrease in energy. Inelastically scattered electrons either contribute to the background spectrum or fail to escape the solid, and these electrons can be counted as lost for XPS analysis. These considerations are crucial for accurately interpreting the XPS data and determining the elemental composition of the h-BN sample.

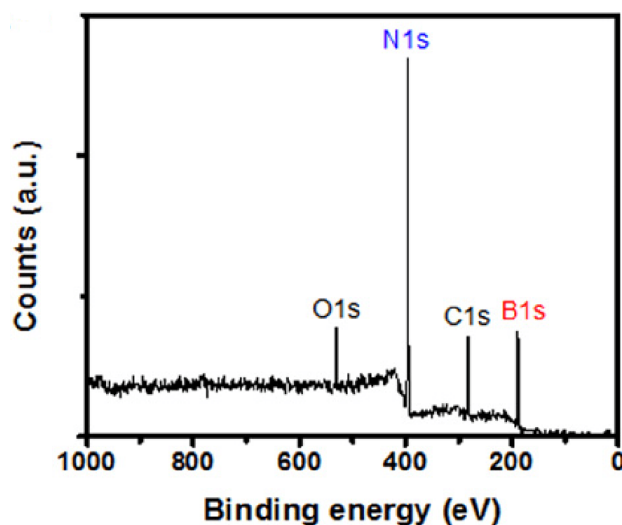


Figure 3.8: Survey spectra of an h-BN sample in the spectral range of energy from 0 to 1000 eV. Are highlighted the interest elements to posterior analysis [1].

The peaks of primary interest are the B $1s$, N $1s$, and Si $2p$ regions as they provide indications of the elemental composition. This is achieved through calculations using area quantification methods and the atom sensitivity factor to obtain atomic percentages.

3.4 Principles of atomic force microscopy (AFM)

The atomic force microscope (AFM) is a member of the class of microscopes known as scanning probe microscopes (SPM), which originated from the scanning tunneling microscope (STM). This approach was pioneered in 1986 by Binnig, Gerber, and Quate, who demonstrated the concept of AFM for the first time. AFM images are acquired by detecting the force exerted on a sharp tip (insulating or not) created by proximity to the surface of the sample.

This force is kept small and at a constant level with a feedback mechanism [76].

Since its invention, AFM has been used in all fields of science, such as chemistry, biology, physics, materials science, nanotechnology, astronomy, medicine, etc.

Figure 3.9 shows a schematic of an AFM showing the fundamental components. Including the scanning unit, which moves the cantilever with a sharp tip across the sample surface, the tip is generally made of silicon or silicon nitride (Si_3N_4). It approaches the sample in a range of interatomic distances (around 10 \AA), an optical detection system that measures the deflection of the cantilever corresponding to a four-quadrant photodiode detector, and the feedback electronics responsible for maintaining a constant force between the tip and the sample [77].

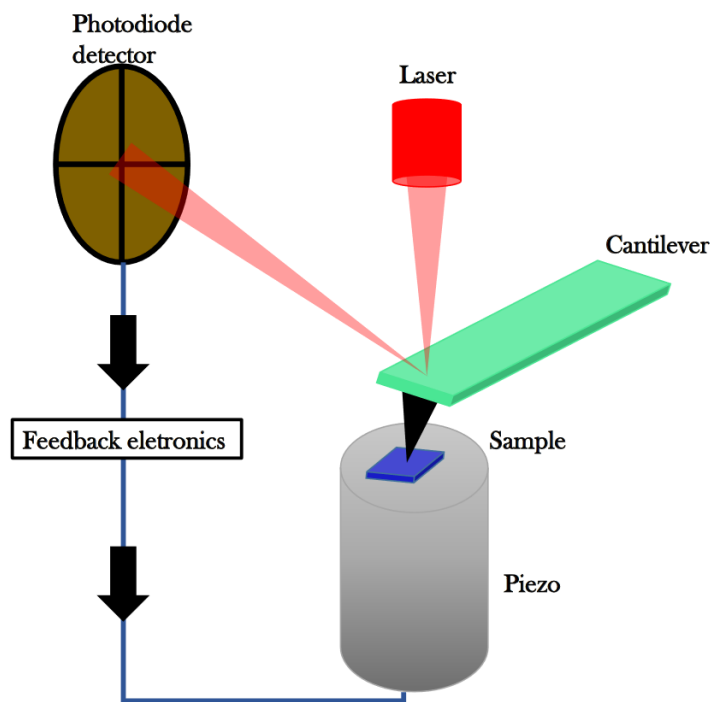


Figure 3.9: The schematic illustrates an Atomic Force Microscope components. A sharp tip mounted on the end of a cantilever, a position-sensitive photodiode, laser diode, sample to be measured, sample holder (base), piezo scanner are shown.

3.4.1 AFM operation modes

AFM operates in three primary working modes, depending on the separation between the tip and the sample surface: contact mode (also known as repulsive mode), non-contact mode (also known as attractive mode), and

intermittent-contact, in this mode, the AFM probe's oscillation is large enough to move from the repulsive regime, through the attractive regime. The contact and non contact are represented in Figure 3.10.

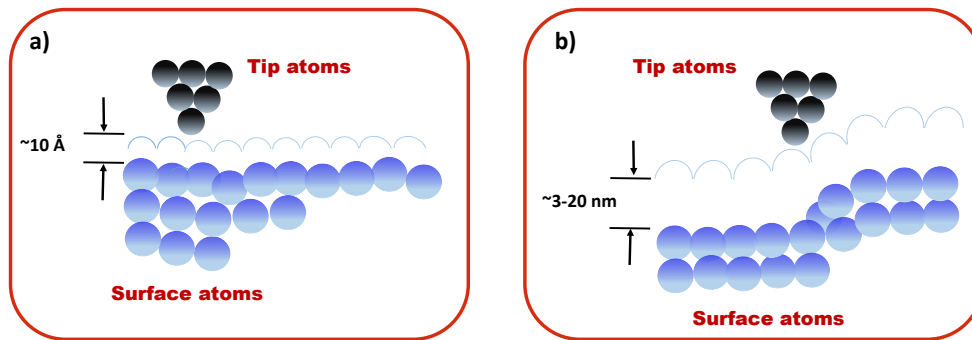


Figure 3.10: Two modes of operation are depicted. Small circles represent sample atoms, and dotted lines represent the contour of constant force. a) Contact mode and b) Non-contact mode.

In contact mode, the tip is brought atomically close to the sample surface, allowing for direct interaction between the tip and the atoms/molecules on the surface. This proximity enables the attainment of atomic resolution, providing detailed information about the surface topography and properties of the sample.

Due to the close proximity in contact mode, atomic force interactions can be significant enough to cause modification of both the tip and the sample, which is generally undesirable. Figure 3.11 shows the force-distance curve on y and x (axis) are the plot of the force vs. distance, this curve is measured by monitoring the deflection of the cantilever.

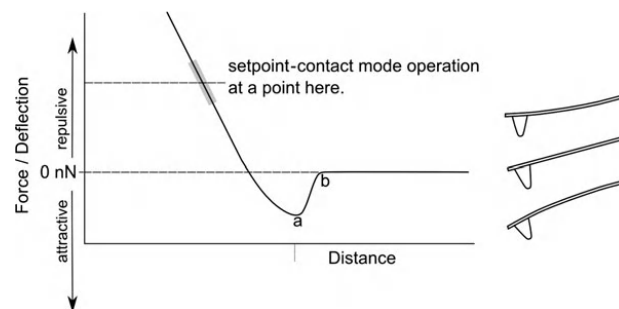


Figure 3.11: The force-distance curve for contact (repulsive region) mode scanning regime. The deflection-distance curve, may be converted to a force-distance curve, both have a similar shape. Right: illustration of probe bending [13].

The tip deflection is a result of tip-sample interaction, therefore, the deflection vs. distance curve, may be converted to a force-distance curve. In this regard, the cantilever can be thought as a spring, in which the quantity

of the generated force between the tip and the surface depends on the spring constant (stiffness) of the cantilever and the distance between the tip and the surface. This force can be characterized as Hooke's Law.

$$F = -k \times D \quad (3-22)$$

Where, F - force (N), k - probe force constant (N/m) and D - deflection distance m . Equation 3-22 shows that a probe with a high force constant means a stiff cantilever or a greater deflection; therefore, a higher set point will result in a higher applied force. The feedback system is used to control the cantilever deflection at a certain value called a set-point.

In contrast, non-contact mode maintains a relatively larger separation between the tip and the sample. In this mode, long-range interaction forces such as Van der Waals force, magnetic force, or electrostatic force are measured without the risk of altering the tip or sample.

One of the limiting factors for non-contact mode in air is the contamination layer present on most surfaces under ambient conditions. In general, the presence of this layer means that the probe-surface interaction forces are governed by the capillary forces between the probe and the contamination layer. Non-contact AFM is therefore conducted in the attractive regime, as depicted in Figure 3.12. Non-contact or close-contact AFM is a widely applied technique and can be used to image almost any sample in AFM [77, 13].

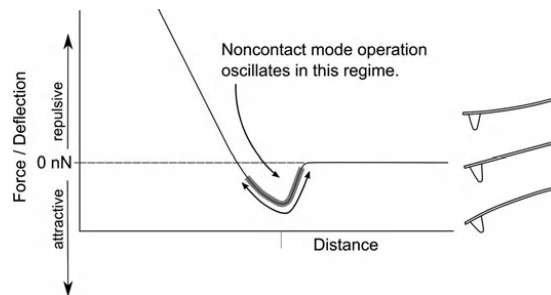


Figure 3.12: The force-distance curve for non-contact (attractive regime) AFM [13].

By using a highly stiff cantilever and monitoring the dynamic effects of the attractive force (i.e., the change in oscillation) in this regime, it is possible to keep the cantilever very close to the surface without transitioning to the repulsive regime. Changes in oscillation amplitude and phase can be observed in this regime. These effects are caused by a change in the cantilever's resonant frequency, which is, in turn, caused by forces from the surface (usually attractive Van der Waals forces) acting on the tip.

Finally, the intermittent contact mode involves the tip coming into intermittent contact with the sample, leading to very strong short-range force contributions close to the sample. In tapping mode, the constant driving frequency is usually selected at or very close to the resonance frequency of the free cantilever. This means that this mode of operation is less destructive than the contact mode.

In this case, the feedback is usually based on amplitude modulation and the tip-sample interaction passes through the attractive regime, and into the repulsive regime, as shown in Figure 3.13.

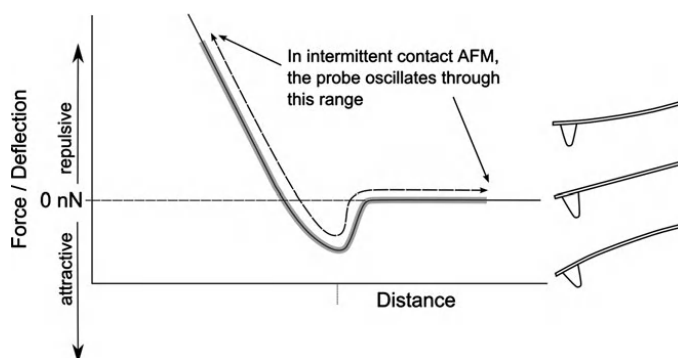


Figure 3.13: Intermittent-contact operating regime. In this mode, the AFM probe's oscillation is large enough to move from the repulsive regime through the attractive regime [13].

Therefore, the electronic feedback loop maintains the oscillation amplitude constant, ensuring a consistent tip-sample interaction throughout the scan. This mode eliminates frictional force by intermittently contacting the surface and oscillating with sufficient amplitude to prevent it from being trapped by adhesive forces. Then, intermittent-contact mode is a widely applied technique and is currently the most widely used technique for imaging in air [77, 13].

3.5 Wettability

Studies related to wettability began in the 19th century when Thomas Young, in 1805, derived an equation based on the idea of force equilibrium. Figure 3.14 schematically illustrates the definition of the contact angle between two surfaces, considering a smooth and a rough surface [78, 79].

Every material has the ability to retain or repel water molecules. This condition is commonly referred to as wettability, which has two defined states: hydrophilic and hydrophobic. The wettability of a material can be determined by calculating the angle formed between a droplet of any liquid and the solid surface. [78, 80].

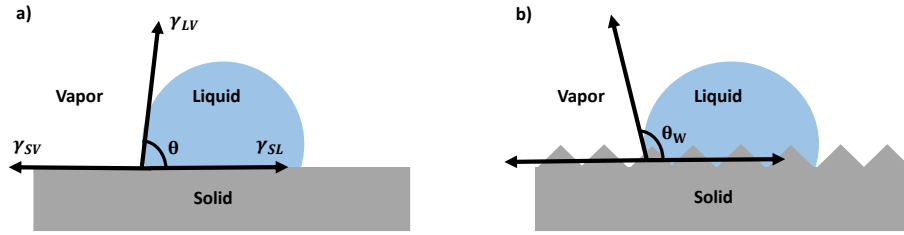


Figure 3.14: Wetting model diagram: (a) Young's model; (b) Wenzel's model

To define the wettability states, we use the magnitude of contact angles as follows: when angles are less than 90° , surfaces are termed hydrophilic; for angles ranging from 90° to values near 120° , surfaces are considered hydrophobic. For contact angles exceeding 120° , surfaces are referred to as superhydrophobic.

In any process involving the wetting of a solid by a liquid, three distinct interfacial boundary surfaces, specifically, solid-liquid, solid-air, and liquid-air are implicated. These surface relationships are contingent on the conditions of the problem and may evolve gradually as wetting progresses. The Young equation correlates the contact angle (θ) between a solid surface and the liquid with the surface tensions and is given as follows [79, 80]:

$$\gamma_{LV} \cos \theta = \gamma_S - \gamma_{SL} \quad (3-23)$$

Here, (γ_{LV}) is the liquid-vapor interface, (γ_{SL}) is the solid-liquid interface, and (γ_S) is the solid-vapor interface. This theory is only applicable to a completely smooth surface with uniform chemical and nonelastic properties, as shown in Figure 3.14 (a). However, such a surface does not exist. The Wenzel model was introduced to address this limitation, suggesting that droplets will become tiny grooves when in contact with a rough surface. Consequently, the droplets expand the contact area beyond the apparent area of contact (see Figure 3.14 (b). Equation 3-24 [80]:

$$\cos \theta_W = r \cos \theta \quad (3-24)$$

where θ_W is the apparent contact angle, r is the roughness factor and θ is the contact angle of a water droplet on a homogeneous surface.

Given that each interface has its unique surface energy content, wetting, accompanied by alterations in the extent of each interface, results in a net decrease or increase in the total surface energy. Wetting is, therefore, a thermodynamic process, and the extent of the free energy change dictates whether wetting will occur spontaneously, at what rate, and to what extent it can advance against external forces that may resist it. Conversely, it determines the magnitude of the external force required to overcome the initial resistance

to wetting [81].

Hydrophilic surfaces are characterized by a high level of surface energy, whereas hydrophobic surfaces possess low surface energy. The adhesion between materials depends on their respective energies, specifically, the higher the energy, the better the adhesion between materials [81]. Figure 3.15 depicts two images of water droplets on the uncoated Si substrate and thin films of h-BN deposited under different conditions, showcasing the hydrophilic and hydrophobic characteristics of uncoated Si and Si coated with h-BN thin films.

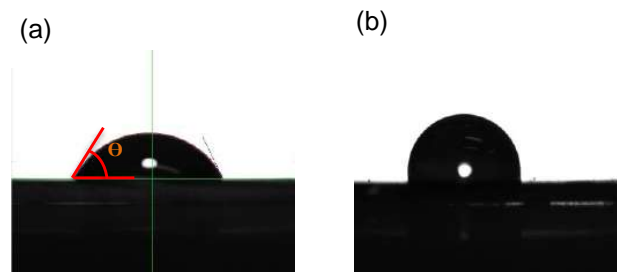


Figure 3.15: Water droplets on bare Si and on the Si substrate coated with h-BN films at 10 min of growth time deposition. (a) bare Si - $\theta = 61.0^\circ \pm 1.0$, and (b) 10 min - $\theta = 105.0^\circ \pm 5.0$.

3.6

Scanning Transmission Electron Microscopy (STEM)

The Scanning Transmission Electron Microscope (STEM) was designed by Manfred von Ardenne in 1937-1938. He demonstrated an image of ZnO crystals with a resolution of 40 nm in the same direction as the horizontal scan. These results were published in 1938.

After a few years, he made improvements that allowed a four-fold increase in resolution, reaching 10 nm. These enhancements were achieved by arranging the detector for bright-field or dark-field imaging in transmission and for reflection or secondary imaging of solid surfaces. Von Ardenne's motivation for developing the STEM was that transmitted electrons did not need to be refocused to form a high-resolution image; they merely needed to be detected.

Consequently, the resolution of a STEM image would not be degraded by the chromatic aberration of the imaging lenses, as was the case with TEM. The optical configuration of the STEM is shown in Figure 3.16 where the components include a series of lens to focuses the beam to form a small spot incident upon a thin sample that is electron transparent. Typical STEM samples, including tissue sections, lamella, and nanoparticles with a thickness

on the order of 100 *nm* or less, require the criteria for electron transparency [14].

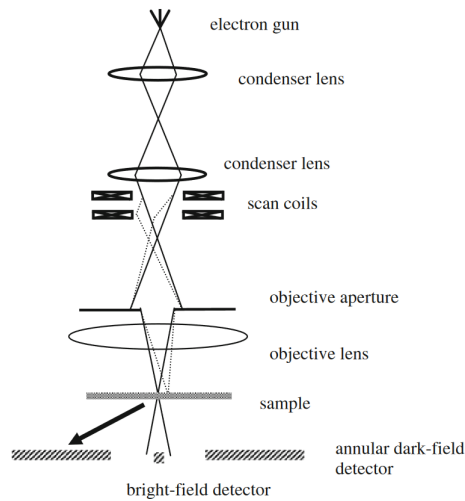


Figure 3.16: Schematic diagram of the major STEM components [14].

The lenses are configured to provide sufficient demagnification (reduction of the diameter of the electronic beam) of the finite-sized electron source in order to form an atomic-scale probe at the sample. Therefore, the first two sets of lenses are called condenser lenses, the lenses slightly above the specimen are called objective lenses, which provide the largest demagnification step. In addition, the objective aperture has two significant considerations, which control the diffraction limit allowing the smallest spot, and limits the amount of beam current due to the loss of electrons that do not pass through the aperture. In STEM, images are built up pixel by pixel by scanning the beam across a fixed field of view using scan coils. Therefore, the magnification is controlled by the size of the scanned area.

The signals collected most frequently in the STEM are the following:

- Bright Field (BF)- Transmitted electrons that leave the sample at relatively low angles with respect to the optic axis (smaller than the incident beam convergence angle).
- Annular Dark Field (ADF)- Transmitted electrons that leave the sample at relatively high angles with respect to the optic axis, typically several times the incident beam convergence angle.
- Electron Energy Loss Spectroscopy (EELS)- Transmitted electrons that have lost a measurable amount of energy as they pass through the sample, forming a spectrum based on the energy lost.
- Energy Dispersive X-ray Spectroscopy (EDX)- X-rays generated from electron excitations in the sample.

The electrons contributing to STEM images can be finely controlled by varying the camera length and inserting various detectors, Figure 3.17 show various STEM detectors.

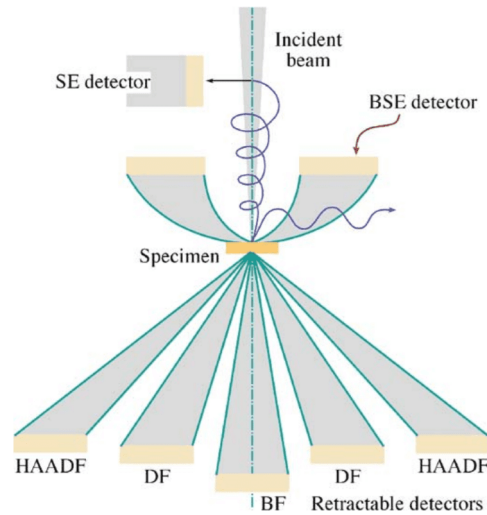


Figure 3.17: Schematic of the various electron detectors in a STEM [15].

3.7

Scanning Electron Microscopy (SEM)

The development of scanning electron microscopy began with the work of M. Knoll in 1935, which detailed the conception of the SEM. The first scanning electron microscope designed for observing thick samples was constructed in 1942 at the RCA laboratories, utilizing a secondary electron detector to produce the image.

The major components of a scanning electron microscope (SEM) are in the electron column, as shown in Figure 3.18. The electron column consists of an electron gun and two or more electron lenses, which influence the paths of electrons traveling down an evacuated tube. The base of the column typically contains vacuum pumps that produce a vacuum of about 10^{-4} Pa. The control console includes a cathode ray tube (CRT) viewing screen, along with the knobs and computer keyboard that control the electron beam.

In the opto-electronic column are located the electron gun, which generates the primary electrons; the condenser lenses, which collimate the primary electron beam; the coils, which deflect the primary electron beam horizontally and vertically over a given region of the sample, also the coils that correct for astigmatism, and the electron detector which is positioned to capture secondary electrons emitted from the sample surface, enabling image formation.

The entire column must be under vacuum during the emission of the primary electron beam [82].

The lens at the final of the column is the objective lens, close to the specimen, whose primary function is to focus the image by varying the focal distance of the electron beam along the optical axis (Z -axis) of the column. This lens typically contains the deflection coils, the astigmatism correction coils, and the final aperture.

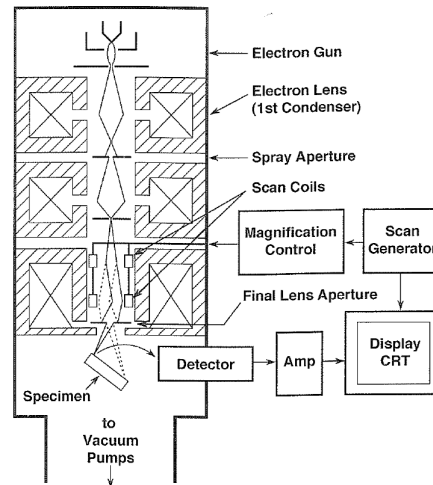


Figure 3.18: Schematic of the electron column showing the electron gun, lenses, the deflection system, and the electron detector [16].

The electron gun generates electrons and accelerates them to an energy range of 0.1-30 keV (100-30,000 electron volts). The spot size from a tungsten hairpin gun is too large to produce a sharp image unless electron lenses are used to demagnify it and create a much smaller focused electron spot on the specimen. Most SEMs can produce an electron beam with a spot size of less than 10 nm (100 Å) at the specimen, containing sufficient probe current to form an acceptable image. The beam emerges from the final lens into the specimen chamber, where it interacts with the specimen to a depth of approximately 1 μm , generating the signals used to form an image.

3.8 Ultra Violet visible spectroscopy

In optical spectroscopy the absorbed or emitted radiation of frequency or wavenumber is governed by the relationship given by Equation 3-17, known as the Bohr-Einstein frequency. This relationship establishes a connection between the discrete atomic or molecular energy states E_i and the frequency ν of the electromagnetic radiation.

UV-vis and IR spectroscopy exploit the interaction of electromagnetic (EM) radiation with matter, as discussed in the previous section. In both

techniques, the absorption of EM radiation is utilized to identify molecules by considering their characteristic spectra. UV-vis spectroscopy yields spectra with broad electronic signals, while IR spectroscopy, due to the narrower energy separation of vibrational bands, offers more detailed spectral information [83].

The process of UV-Vis radiation absorption by a molecule can be illustrated using a Jablonski diagram, as shown in Figure 3.19. Electronic energy levels are represented by horizontal lines: S_0 being the lowest level, S_1 the first excited state, and S_2 the second excited state. The vibrational levels, indicated as $\nu = 0, 1, 2, 3$ are associated with each electronic state. Upon absorbing a photon that resonates with the energy gap between the ground state and an excited state, the molecule is excited to a vibrational level within the excited electronic state. This process is illustrated by the blue and purple arrows. However, the states $\nu' = 1, 2, 3$ are unstable and immediately relax to the vibrational ground state $\nu' = 0$ via a nonradiative process called intermolecular collisions or internal conversion (IC), shown as wavy black arrows. Another relaxation process involves the emission of a photon, a radiative process, which occurs between electronic levels, indicated by the green arrow ($h\nu_F$), which represents fluorescence. Both processes are related to singlet states, while the phosphorescence process occurs at the triplet (T_1) state ($h\nu_p$) [83].

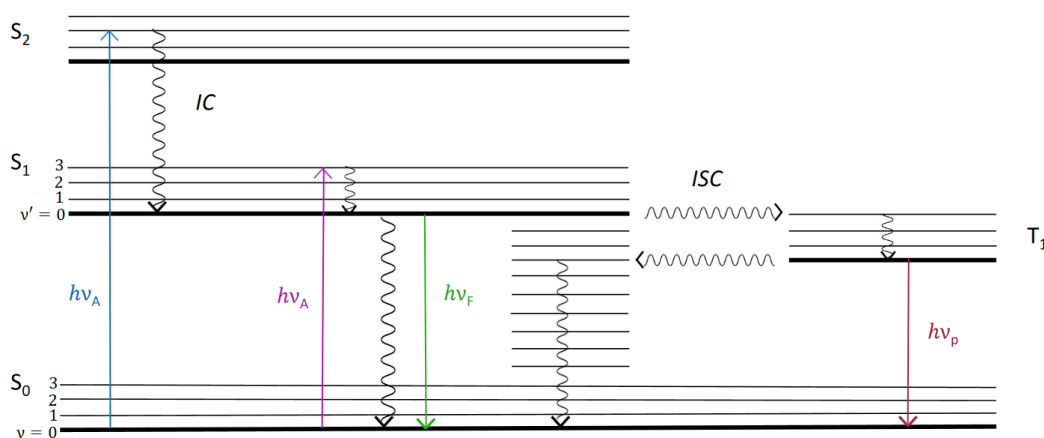


Figure 3.19: The Jablonski diagram for a hypothetical molecule illustrates various photophysical processes. It depicts the absorption of a photon (indicated by purple and green arrows, thermal (non-radiative) relaxation processes including internal conversion (IC) and intersystem crossing (ISC) (represented by black arrows), fluorescence (yellow arrow), and phosphorescence (red arrow).

3.9 Tribology

Tribology refers to the scientific and technological study of two surfaces that interact in relative motion, together with associated subjects and practices. Its common equivalents are friction, wear, and lubrication. Coined in 1966, the term "tribology" originates from the Greek word "tribos," meaning rubbing, hence its literal translation as the science of rubbing.

The emergence of novel techniques to investigate surface topography, adhesion, friction, wear, lubricant film thickness, and mechanical properties at micro- to nanometer scales, permits advancements in imaging lubricant molecules for atomic-scale simulations and has given rise to a new domain known as microtribology, nanotribology, molecular tribology, or atomic-scale tribology. It focuses on phenomena related to adhesion, friction, wear, and thin-film lubrication at sliding surfaces.

The components utilized in micro and nanostructures are extremely lightweight, typically on the order of a few μg , and function under very light loads, ranging from a few μg to a few mg . Consequently, the friction and wear experienced by lightly loaded micro/nanocomponents, particularly at the nanoscale, are influenced by surface interactions spanning only a few atomic layers. Typically, these structures are lubricated using molecularly thin films.

Friction is commonly quantified using a coefficient denoted μ , which is defined as the ratio of the friction force F_r to the normal force (F_N) acting perpendicularly to the surfaces in contact. Mathematically, this can be expressed as:

$$\mu = \frac{F_r}{F_N} \quad (3-25)$$

Where, μ is the coefficient of friction, F_r is the frictional force opposing motion or relative sliding between the surfaces, and (F_N) is the normal force exerted perpendicular to the surfaces in contact. With regard to wear, it is essential to determine the volume rate of wear and to establish the conditions under which catastrophic failure may occur due to wear. This involves understanding the mechanisms of material loss and the factors that can lead to significant degradation of the interacting surfaces over time. The fundamental problem in all studies on friction is determining the coefficient of friction, however it is normally very difficult to predict the value of μ and the wear characteristics of the two surfaces. The reason for this lies in the extreme complexity of the surface phenomena involved in tribology. Three types of surface characteristics contribute to this complexity:

- (1) Surface Geometric Structure: Physical topography and roughness of

the surfaces in contact.

(2) Nature of Surface Forces: The interactions between surface molecules, including adhesive and repulsive forces.

(3) Material Properties of the Surface: The intrinsic properties of the materials making up the surfaces, such as hardness, elasticity, and chemical composition.

Therefore, the tribological literature contains many friction and wear theories that are applicable on different length scales, from macroscopic to atomic scales. Furthermore, a single unifying theory of tribology has not yet been developed. Figure 3.20 (a) shows two surfaces in contact, that is, under a static compression force of F_N . Both exhibit multiscale roughness, so contact will only occur at discrete points that sustain the full compressive force. In this case, the contact between the surfaces is spatially randomly distributed along the interface and the difference in spot size occurs due to the multiple roughness scales.

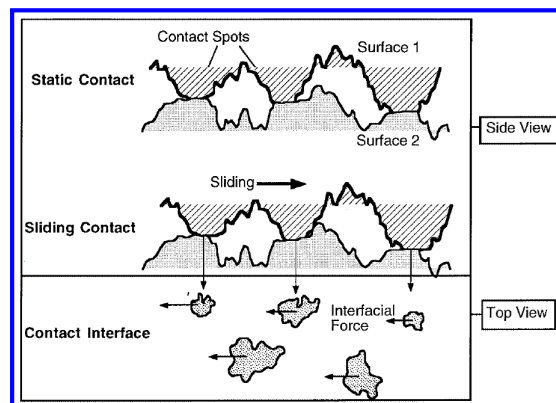


Figure 3.20: (a) A schematic diagram of two surfaces in static contact shows that the contact occurs at only a few discrete contact spots, and (b) two surfaces in sliding contact, therefore the interfacial forces act on these contact spots [17].

On the other hand, when the two surfaces slide against each other, a term related to the resistive tangential force, or frictional force, appears due to the force interactions between the two surfaces that act only at the contact spots, as shown above. It is reasonable to consider that the tangential force depends on the spot size since they are connected by the solid bodies that can support some elastic or plastic deformation.

One can imagine the contact spots to be connected by springs, where the spring constant depends on the elasticity or plasticity of the contacting materials. Since the number of contact spots is very large, the springs form a highly complicated dynamic system. Finally, the basic problem of tribology can be divided into the following aspects: determining the size and spatial

distribution of contact spots, which depend on surface roughness, normal load, and mechanical properties, finding the tangential surface forces acting at each contact spot, and determining the dynamic interactions between these contact spots. That means evaluating the cumulative effect of these interactions in terms of the friction force [17].

3.10 Chemical Vapor Deposition - (CVD)

The Chemical Vapor Deposition (CVD) technique, a bottom-up approach it is widely employed for nanomaterial synthesis on solid substrates, stands out for its superior control over the fabrication of nanomaterials when compared to other synthesis methods. In Figure 3.21 shows a schematic representation of a typical furnace. The CVD exhibits various variations, including atmospheric pressure chemical vapor deposition (APCVD), low-pressure chemical vapor deposition (LPCVD), plasma-enhanced chemical vapor deposition (PECVD), and metal-organic chemical vapor deposition (MOCVD) [84].

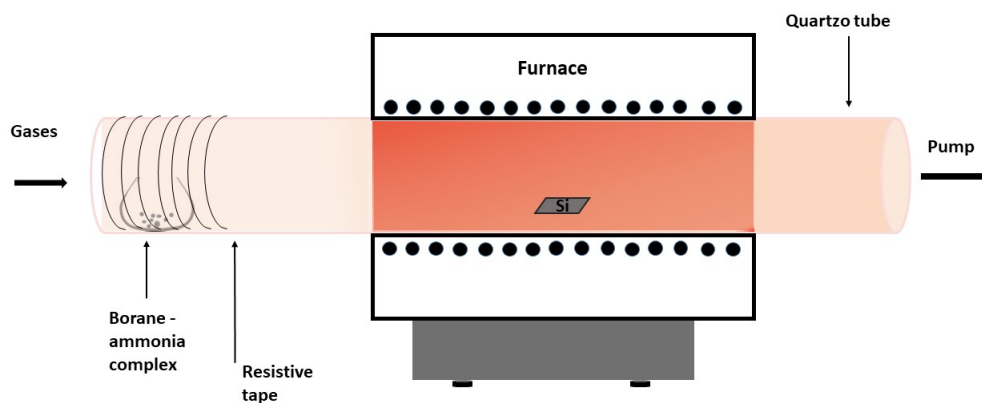


Figure 3.21: Illustrates the setup utilized for the CVD process. The Si $\langle 100 \rangle$ substrate is positioned at the center of the hot zone within the furnace, ensuring optimal exposure to the precursor gases for h-BN film deposition.

In the CVD process, the substrate is exposed to one or more volatile precursors. These precursors undergo reactions and/or decomposition on the substrate surface, leading to the formation of a thin film deposit. This material could be a metal, semiconductor, alloy, nanocomposite, or refractory compound. The process extends to the growth of diverse nanosheets such as graphene, h-BN nanosheets, Transition Metal Dichalcogenides (TMDs), metal carbides, borophenes, antimonene, and silicene. Fine-tuning of the growth of

nanomaterials is achievable by adjusting the CVD parameters, including substrate type, precursors, catalysts, and temperature. Typically carried out at high temperatures and in a vacuum within a reactor [85].

The CVD synthesis process brings forth notable advantages, yielding high-quality, high-purity nanomaterials with precisely controlled properties. This control extends to manipulating the morphology, crystallinity, and defects of the nanostructures through parameter adjustments. Consequently, certain nanomaterials such as graphene MoS_2 and h-BN have been conveniently prepared using this method [86].

The technique facilitates the mass production of materials with high crystal quality, purity, and limited defects on substrates. Applications of 2D nanomaterials prepared using CVD span various fields, including electronics, optoelectronics, and solar cell devices. Despite its advantages, the CVD technique encounters challenges, including the requirement for high temperatures, a high vacuum environment, and specific substrates [87, 86].

3.11

Ultrasonic bath

The ultrasound technique employed in this thesis is utilized for cleaning various components such as tweezers, substrates, quartz crucible, metallic components of CVD connections, etc. The cleaning process is based on a method of cleaning that uses high-frequency sound waves. Figure 3.22 shows a schematic that comprises the following components:

- Ultrasonic Cleaning Tank: This tank serves as the vessel that contains the ultrasonic bath fluid and the objects targeted for cleaning.
- Ultrasonic Generator: The generator is responsible for converting alternating current (AC) electrical energy into ultrasonic frequency waves.
- Ultrasonic Transducer: The transducer plays a crucial role in converting the electrical signal from the ultrasonic generator into mechanical energy, which is then transmitted as ultrasonic waves into the cleaning solution.

It should be noted that contaminants that can be effectively removed by ultrasonic cleaning include dust, dirt, oil, grease, pigments, flux agents, fingerprints, and polishing compounds [18].

The efficiency and quality of ultrasonic cleaning can be expressed as follows:

$$\frac{\Delta G}{G} = 1 - \exp(-Qt^{0.5})$$

The symbols ΔG and G denote the quality of the cleaned dirt and the original dirt, respectively. While, t represents the duration of the cleaning

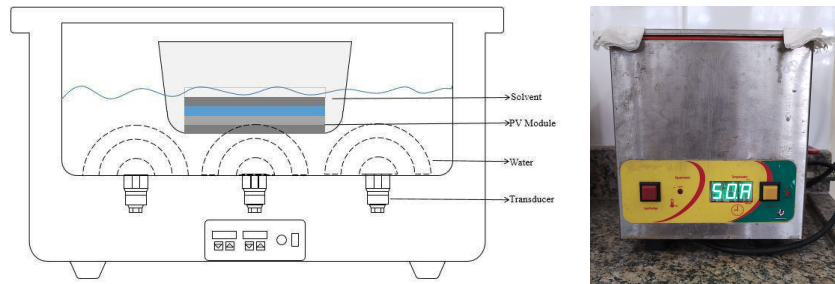


Figure 3.22: Left: the schematic depiction of the ultrasonic cleaning apparatus illustrates key components, including the immersed sample within the solvent, the water bath contained within the tank, and the transducer [18]. Right: ultrasonic cleaner in the *Laboratório de Revestimentos Protetores e Materiais Nanoestruturados* at PUC-Rio.

action, and Q stands for the cleaning efficiency coefficient. The variable Q is related to other acoustic parameters, including ultrasonic frequency, power, distribution of the ultrasonic field, properties of the cleaning solution, duration of the cleaning action, shape of the dirt to be cleaned, acoustic characteristics, among others.

A higher value of Q signifies better cleaning quality and higher cleaning efficiency. This indicates that optimizing acoustic parameters and other influencing factors can lead to more effective removal of contaminants and improved cleanliness results during ultrasonic cleaning processes [88].

4 Methodology

In this chapter, we describe the materials and experimental methodologies utilized, following established protocols for substrate and material cleaning procedures, as well as the optimal parameter conditions employed during the deposition process of h-BN films.

4.1 Materials and methods

The deposition of hexagonal boron nitride (h-BN) films involved the utilization of the following materials, and equipment:

- A one-inch quartz tube.
- A quartz crucible designed to accommodate the precursor.
- The precursor source consisting of Borane-ammonia complex (AB), acquired from the corporation SIGMA-ALDRICH, serving as the primary supplier of B and N.
- Analytical balance unibloc AUW220D, Shimadzu Corporation to weigh the precursor powder.
- A Silicon substrate of type p oriented along the $\langle 100 \rangle$ crystal plane, possessing a thickness of 500 ± 15 micrometers (μm).
- A chemical vapor deposition furnace (CVD) connected to a mechanical pump with a specified flow rate expressed in cubic meters per hour ($70 m^3/h$), together with digital mass flow controllers (MFC) to regulate the precise flow of gases.
- An ultrasonic cleaning apparatus was utilized for the cleaning of substrates and materials.
- A computer system configured for interfacing with hydrogen (H_2) and argon (Ar) MFC's via an Internet Protocol (IP) address, enabling digital control and monitoring of gas flow parameters.
- Resistive tape affixed to a voltage regulator (variac) capable of generating up to 250 Volts (V), used for the sublimation process of the precursor material.

4.2

Borane - ammonia complex (AB) Precursor

In this thesis, AB (BH_3NH_3), is employed as the precursor source of B and N atoms. It was purchased from Sigma-Aldrich Corporation (97% pure). The AB has proven to be a successful single source solid precursor for the production of high-quality h-BN films. This success is attributed to its intrinsic 1:1 B/N stoichiometry, which facilitates the formation of large single crystal domains [49].

Consequently, AB has been utilized as a precursor for the controlled synthesis of h-BN layers. Upon decomposition, the AB precursor yields hydrogen (gas), monomeric aminoborane (solid), and borazine (gas), allowing controlled synthesis [50].

Despite these advantages, AB as a solid precursor presents notable benefits, particularly in terms of chemical stability. It exhibits resistance to oxidation, preventing the formation of borates, and provides significant safety advantages in laboratory environments due to its ease of handling, which is considerably less toxic, and is a relatively low-cost precursor [51].

The thermal decomposition of AB as a precursor occurs in the temperature range of 343 to 413 K. The resulting gaseous molecules are adsorbed on the surface of the substrate, typically copper, and transported to this surface by a carrier gas, such as an argon gas [48].

The AB decomposition studies conducted by Frueh *et al.* (2011) through the use of vibrational spectroscopy techniques, such as FTIR analysis showed the evolution of stretching peaks from room temperature, 393, and 483 K. As a result of the increase in temperature, the release of gaseous species such as hydrogen and borazine ($\text{N}_3\text{B}_3\text{H}_6$) was observed, as well as solid-phase species such as polyaminoborane (PAB) $[\text{NH}_2 - \text{BH}_2]_n$ and polyiminoborane (PIB) $[\text{NH} = \text{BH}]_n$. The positions of the NH and BH stretching mode peaks decreased slightly from the AB case, as indicated in Table reftab: AB. This is associated with the loss of high-symmetry stretching modes present in AB that cannot exist in PAB.

Sample	NH (cm^{-1})	BH (cm^{-1})	BN (cm^{-1})
AB - RT	3302	2278	781
AB - 393 K	3250	2250	850
AB - 483 K	3435	2498	1344

Table 4.1: FTIR - Bond Stretch assignments from Frueh *et al.* (2011) studies [19].

In this work, the decomposition of the precursor subjected to different

temperatures was investigated, in Figure 4.1 shows the Raman spectra of the pure AB precursor, for the residual material that was collected after the synthesis of h-BN and that underwent temperature decomposition at 373 K and 403 K, respectively. It was determined that the optimal decomposition temperature for effective film growth is 373 K. The spectral analysis focused on three distinct regions, as indicated in the studies by Frueh *et al.* (2011) conducted through FTIR analysis.

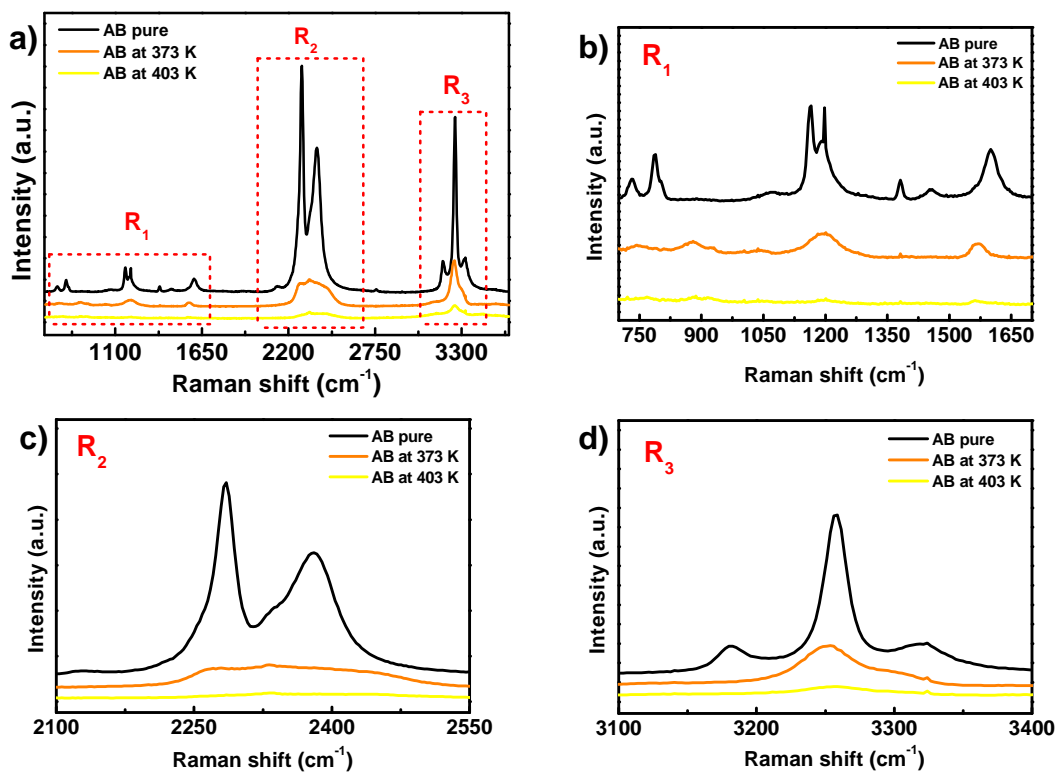


Figure 4.1: Raman spectroscopy of Ammonia - borane (AB) powder pure, and the residual material collected after synthesis, heated at 373 K and 403 K. (a) Raman spectra of the entire region of the powder of AB pure, heated at 373 K and 403 K, respectively. Indicating three distinct regions R_1 , R_2 , and R_3 . (b) the peak in the region R_1 at $\sim 785 \text{ cm}^{-1}$ is related to BN bonds. (c) the peak in the region R_2 at $\sim 2285 \text{ cm}^{-1}$ is related to BH bonds and (d) the peak in the region R_3 at $\sim 3257 \text{ cm}^{-1}$ is related to NH bonds.

Specifically, the peaks identified through Fourier Transform Infrared (FTIR) analysis were associated with Raman spectroscopy, where the NH bond vibrations occurred at 3257 cm^{-1} , the BH bond vibrations at 2285 cm^{-1} , and the BN bond vibrations at 785 cm^{-1} . These findings regarding the bonds were found to be consistent with those of this thesis for the data obtained from Raman spectroscopy. It should be noted that, with the increase in temperature, there is a considerable loss in symmetry of the modes associated with mass loss.

4.3

Substrate preparation

The Silicon (Si) wafer of $500 \pm 15 \mu\text{m}$ thick was initially cleaved into pieces aligned along one of the preferred crystal orientations, using a diamond-tip pen tool (Figure 4.2). These pieces, $\sim 1.5 \text{ cm}^2$ in size, underwent a cleaning procedure before entering the CVD chamber.



Figure 4.2: Si substrate of 500 ± 15 micrometers (μm) thick cut with a diamond-tipped pen tool in the preferred crystal orientation.

The removal of the native silicon oxide layer was achieved by immersing the substrates in hydrofluoric acid (HF) for a duration of 1 minute. Subsequently, the substrates were rinsed multiple times with deionized water and then subjected to ultrasonic treatment for 10 minutes. Following this step, the substrates were placed in an ultrasonic bath containing 30 mL of acetone and then isopropyl alcohol, each for a period of 10 minutes. In the end, the substrates were dried using a flow of nitrogen (N_2) gas.

4.4

Cleaning procedure of quartz tube and crucible

Following each deposition process, a cleaning protocol was applied for both the quartz tube and the deposition crucible. Initially, they were scrubbed using a specially designed brush for cleaning glassware using a neutral detergent solution. Subsequently, they were dried using paper towels.

The quartz tube received cleaning steps involving sequential washing with isopropyl alcohol and acetone, finally, the tube was placed in the oven at 1273 K for 1 hour. Similarly, the deposition crucible underwent an ultrasonic treatment with isopropyl alcohol and acetone, each lasting 10 minutes.

4.5

Hexagonal Boron Nitride (h-BN) synthesis process

The synthesis of h-BN films was carried out using the low-pressure chemical vapor deposition (LPCVD) technique on a Silicon (Si) substrate with an orientation of $\langle 100 \rangle$, as illustrated in Figure 4.3(a) the CVD system used to deposit the samples. The synthesis process involved a gas mixture of Argon-Ar (99.99 pure), Hydrogen- H_2 (99.99 pure), and AB powder as precursor material.

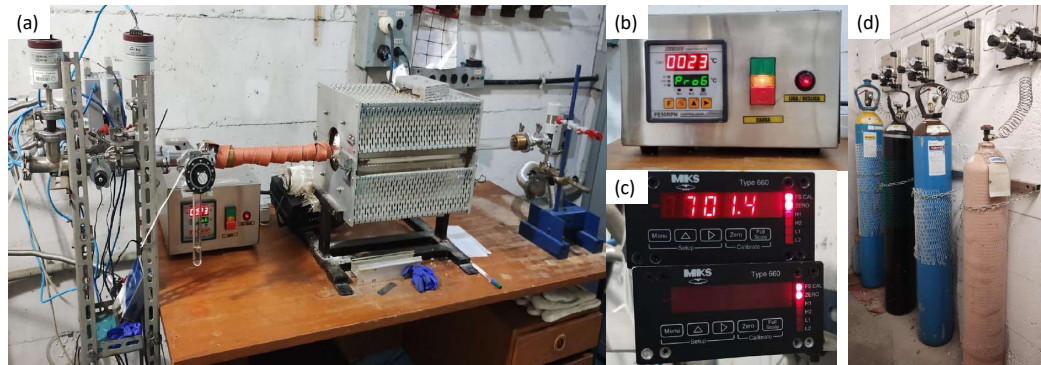


Figure 4.3: Apparatus employed for the deposition of h-BN films comprises: (a) a single-stage temperature-controlled CVD system, (b) an oven temperature controller, (c) the powering and display mechanisms for two Baratron® transducers, calibrated to measure in units of mTorr and Torr, and (d) gas cylinders accessible in the laboratory, including argon, oxygen, hydrogen, and methane.

The Si substrate underwent cleaning procedures described in section (4.3). The cleaned Si substrate pieces (each with an area of 1.5 cm^2) were then loaded into a reactor, consisting of a furnace equipped with a 1-inch quartz tube, operating under controlled atmospheric gas conditions. In a separate hot zone of the quartz tube located upstream 40 cm from the Si substrate, 8 mg of Ammonia - borane (AB) powder was placed in a quartz crucible.

The reactor is connected to a mechanical pump of ($70 \text{ m}^3/\text{h}$) that allows the system to achieve a base pressure of $\sim 10.7 \text{ Pa}$. Pressure was monitored using a digital power supply that displayed the readings of the capacitance manometers on a screen, indicating the pressure in units of mTorr or Torr, Figure 4.3 (c).

Subsequently, a gas mixture of H_2 (99.99 pure) flow of (2 sccm, standard cubic centimeters per minute) and Ar (99.99 pure) flow of (100 sccm) was introduced into the system using digital gas mass flow controllers (MFC), that are connected to a computer by communicating via internet protocol (IP) address. The furnace temperature was ramped up at a rate of $30 \text{ K}/\text{min}$ for 36 minutes until it reached a final working temperature, particularly, 1373 K , the

overview temperature diagram is depicted in Figure 4.4. In the other heating zone of the tube, the AB powder was heated to 373 K using resistive tape.

During the growth process, the pressure remained constant at 5.3×10^3 Pa. After the growth process, the CVD chamber was opened to allow the system to cool at a rate of ~ 300 K/min for 2.5 minutes until it reached 773 K. Subsequently, it took more than 1 hour for the system to return to room temperature under ambient air conditions. All deposition parameters are summarized in Table 4.2.

Parameter	Value
Base pressure (Pa)	10.7
Working pressure (Pa)	5.3×10^3
Ar/H ₂ flow rate (sccm)	100/2
Deposition temperature (K)	1273 - 1373
Distance between Si and crucible (cm)	40
Deposition time (min)	5 - 60
Precursor temperature (K)	373
Precursor (mg)	8

Table 4.2: Experimental parameters used in the deposition of h-BN films on Si substrate.

4.5.1

Variation in growth temperature

In the second part, the investigation shifted its focus to the impact and role of growth temperature. Accordingly, the samples were grown at temperatures of 1273, 1323, and 1373 K. Samples grown below 1223 K, did not show h-BN characteristics, while temperatures exceeding 1373 K compromised the oven functionality, given its upper limit of 1473 K. Including, samples grown at 60 minutes, at 1273, 1323 and 1373 K.

4.5.2

Variation in growth time

In the initial part of this thesis, an examination was conducted on the deposition time parameter and its impact on film growth. Specifically, the deposition time was varied between 5, 10, and 20 minutes at 1373 K, for the growth of the sample, while all other growth parameters were kept constant. Samples with growth times below 5 min did not show h-BN characteristics.

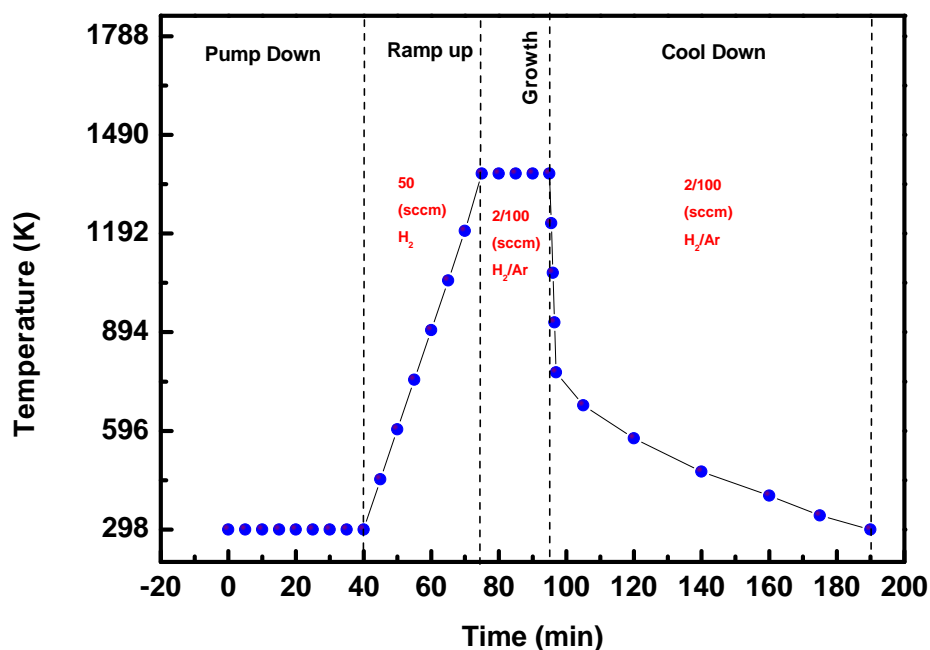


Figure 4.4: Overview temperature profile diagram depicting the temperature distribution within the CVD furnace. The temperature gradient is monitored, starting from the ramp-up to reach 1373 K the deposition temperature and subsequently the growth duration at 20 min of the h-BN films, finally the cool down phase with the opening of CVD chamber to allow the system to cool at a rate of ~ 300 K/min for 2.5 minutes until it reached 773 K, after that, it took over 1 hour and 30 min for the system to return to room temperature under ambient air conditions.

5

Equipment and procedures for characterization

This chapter describes the techniques used in the characterization of h-BN films, focusing on technical operating information, such as operating conditions and principles, including the parameters used to carry out measurements and the environmental conditions under which the samples were exposed.

5.1

Raman spectroscopy/atomic force microscopy (AFM)

Raman spectra and AFM images were obtained using a micro-Raman. The spectrometer consists of a Confocal (upright configuration) from NT-MDT, type NTEGRA SPECTRA, equipped with a CCD (charge-coupled device) detector with a thermoelectric cooling system based on the Peltier effect (with a working temperature of -343 K) and an optical microscope with a single 100 \times objective lens with a large numerical aperture (0.7), used to focus the laser beam on the sample spot size to $\sim 1\mu m^2$ and collect backscattered light. Figure 5.1 shows a photograph of the Raman spectrometer existing in our laboratory and used for measurements.



Figure 5.1: The Raman spectrometer used to analyze the samples in the *Laboratório de Revestimentos Protetores e Materiais Nanoestruturados* at PUC-Rio.

The Raman spectrometer is equipped with a blue laser at a wavelength of 473 nm (2.62 eV) and a maximum output power of 50 mW, and arrival power in the sample on the order of tens of μW including a red, and a green laser at wavelengths of 633 and 532 nm. The system operates with of four gratings that allows obtaining spectra with different spectral resolutions. One of these gratings, an ultra-high dispersion Echelle type, has a spectral resolution of 0.007 nm ($< 0.1\text{ cm}^{-1}$).

Measurements were made with acquisition times ranging from 300-900 s, using 600 (lines/mm) gratings, and achieving a spectral resolution of $\sim 3.4 \text{ cm}^{-1}$.

In the operating mode for carrying out AFM measurements, the samples are mounted on a piezoelectric scanner in a configuration that allows scanning sample by sample with the following dimensions: up to 40 mm in diameter, up to 15 mm in height, and up to 100 g in weight.

After selecting all measurement parameters, after clicking on the RUN button, an image of the scanned area appears line by line in the 2D image panel of the scanned data. Since the sample has a tilt along the X-axis, this tilt can be subtracted in the analysis software. It is consistent that the quality of the images essentially depends on the scanning parameters, such as frequency, set point, and the feedback gain factor (FB gain). All these parameters can be changed directly in the measurement software.

AFM measurements were performed in semi-contact mode, with the setting of the scanned parameter as a different image size from 50 to 1 μm and the number of pixels set to 512 x 512. The topography images were processed using a second-order plane filter to eliminate the tilt between the sample and the microscope.

5.2

FTIR spectroscopy

FTIR spectroscopy was performed on a Bruker FTIR Alpha II spectrometer, using OPUS/IR software for measurements and analysis (Figure 5.2). Measurements were performed in transmittance mode on the ALPHA II-T module with a 30° reflection accessory for solid samples.

The equipment operates according to the following specifications:

- Spectral range 350 - 7.500 cm^{-1} with standard KBr beamsplitter.
- Spectral resolution better than 2 cm^{-1} .
- wavenumber accuracy better than 0.05 cm^{-1} .
- sample spot 8mm.

The measurements were made with 300 minutes of accumulation achieving a resolution of 4 cm^{-1} in the 1600-1200 cm^{-1} region. Standard silicon was used as a background.



Figure 5.2: FTIR spectrometer used to study the vibrational characteristics of the sample in the *Laboratório de Revestimentos Protetores e Materiais Nanoestruturados* at PUC-Rio.

5.2.1

SEM microscopy

The SEM and STEM measurements were carried out in the Van de Graaff laboratory at PUC-Rio, by Carlos Senna. Scanning electron microscopy (SEM) images were acquired with a SCIOS II dual-beam microscope from ThermoScientific. Everhart-Thornley detector (ETD) used in the detection of secondary electrons, working distance of 7.0 mm, chamber vacuum of 2.24×10^{-6} Torr, and magnification varying from 1000 to 120,000 \times .

5.3

XPS spectroscopy

The XPS measurements presented in this work were carried out on two different systems in the first, photoelectrons are energy-filtered using a hemispherical analyzer model Alpha 110 from VG Thermo (Figure 5.3). Subsequently, they are detected by 7 channeltron detectors, which transform the electrons into an amplified current pulse to be analyzed in a multichannel system, resulting in a significant increase in the signal-to-noise ratio after optimizing the count number. Finally, the spectrum is recorded as intensity (counts per second) vs. kinetic energy of the photoelectrons or their binding energy.

The X-ray source used to generate the photoelectrons in the sample was a dual anode electron gun, where in its standard configuration, one anode is covered with Aluminum and the other with Magnesium. The electron beam has sufficient energy to ionize the K-shell of these elements, thus producing a stable X-ray beam with energy dispersion of less than 1 eV.

Survey compositional spectra showing all elements present in the samples were acquired using a pass energy of 50 eV, while for the high-resolution spectra of C *1s*, N *1s*, B *1s*, Si *2p* and O *1s*, a lower pass energy of 20 eV

was used, adjusting the number of scans in both cases to optimize the signal-to-noise ratio. The radiation source used was the K α line of aluminum with an excitation energy of 1486.6 eV. Data analysis was performed using CasaXPS software (from Casa Software Ltd.), with the carbon peak at 284.6 eV used as a reference for binding energies.

X-ray photoelectron spectroscopy (XPS) data were obtained in an ultra-high vacuum chamber with pressure reaching $\sim 10^{-8}$ Pa. Equipped with a VG Thermo Alpha 110 hemispherical analyzer positioned at a 90-degree angle to the sample surface and using a non-monochromatic Al-K α line (~ 1458 eV) as an X-ray beam. The second system used to obtain a few spectra at the end of this thesis, due to problems in the first system, was a SPECS system using a PhoibosTSO analyser.



Figure 5.3: X-ray photoelectron spectrometer used to study chemical composition of the samples in the *Laboratório de Revestimentos Protetores e Materiais Nanoestruturados* at PUC-Rio.

5.4

UV-vis spectroscopy

The UV-vis measurements were carried out in the *laboratório de Pesquisas em Fibras Ópticas* at UERJ-RJ, by professor Alexandre Camara. UV-Vis spectroscopy characterization was performed through diffuse reflectance. Polychromatic light from a UV-Vis-NIR deuterium-halogen light source (Ocean Insight DH-2000-BAL, 210 nm - 2500 nm) was guided through a multimode optical fiber (Ocean Insight, QP300-1-SR, core diameter equal to 300 μm , SMA 905 connectors) and impinged on the sample.

Reflected light was collected by another optical fiber and detected by a UV-Vis-NIR spectrometer (Ocean Insight Flame-T-XR1-ES) with a range from 200 to 1025 nm and a resolution of 0.1 nm. The spectrometer was connected to a computer where the data was processed. The acquisition software (Ocean Insight, SpectraSuite®) allowed us to observe not only the bare spectrum of the light source or the spectrum of the reflected light by the sample, but

also the absorbance or reflectance spectra and process the data with, e.g., the Kubelka-Monk method.

5.5 Contact Angle (Goniometer)

The instrument used to make contact angle measurements was a RAMÉ-HART system (100-25-A), by using the DROPimage software (Figure 5.4).

Contact angle measurements were conducted in the sessile-drop operation mode. A fixed-volume water droplet, of $10 \mu\text{L}$, was deposited onto the sample surface using a needle.

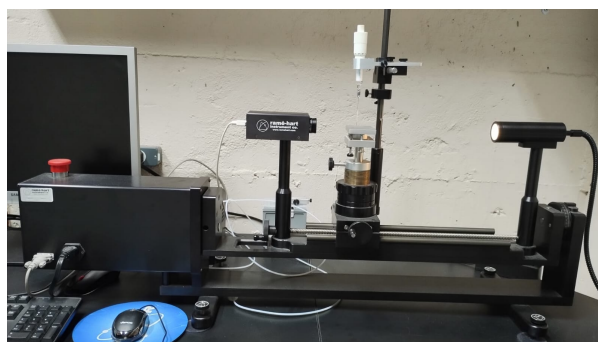


Figure 5.4: Goniometer setup used to contact angles measurements in the *Laboratório de Revestimentos Protetores e Materiais Nanoestruturados* at PUC-Rio.

To ensure statistical integrity, several drops were dropped onto the h-BN surface and for each drop, the number of measurements was set at 100 with a 0.1 s time interval, maintaining consistent conditions for all samples. Finally, the result was obtained by averaging the remaining values from each of the samples.

5.6 Microtribometer

The tribology tests were carried out in the *Laboratório de Caracterização de Materiais* at UFF-RJ, by Professor Juan Lucas Nachez. The equipment used for this purpose was a CTER-UMT micro tribometer with a constant linear load of 0.3 N, corresponding to a constant Hertzian pressure of 398 MPa, considering a flat surface. A stainless steel ball with a 6.35 mm diameter (AISI302) and a hardness of 4.1 GPa was used for the measurements. The test mode involved pin wear on a reciprocal linear disc. The sliding velocity during the test was 10 mm/s, and the sliding amplitude was 10 mm.

6

Temperature-dependent growth of h-BN films

In this chapter, the results of the synthesis of h-BN films will be presented and discussed. Table 6.1 below shows the set of samples grown and the conditions within the temperature range of 1173 K to 1373 K, as well as the samples submitted to tribology tests. Various characterization techniques, such as Raman spectroscopy, Fourier transform infrared (FTIR) spectroscopy, X-ray photoelectron spectroscopy (XPS), atomic force microscopy (AFM), contact angle measurements, scanning electron microscopy (SEM), and UV-visible spectroscopy, were utilized. These techniques were used to investigate the structural, morphological, tribological, and vibrational properties of the h-BN films.

Temperature (K)	Growth	Conditions
1173	No	- Borane ammonia (8 mg) at 373 K
1223	No	- Base/Working pressure ($10.7/5.3 \times 10^3$ Pa)
1273	Yes	- Ramp up H_2 (50 sccm)
1323	Yes	- H_2/Ar flow (2/100 sccm)
1373	Yes	- Growth time (10 min)
Tribology		
Temperature (K)	Growth	Conditions
1273	Yes	
1323	Yes	(same parameters as above)
1373	Yes	- Growth time (1 hour)

Table 6.1: Set of samples varying temperature and for tribology studies with growth conditions.

6.1

Raman spectroscopy

Raman spectroscopy was employed to discern the features of the h-BN film obtained by LPCVD on a Si <100> substrate. In Figure 6.1, several second-order components of the Si substrate are highlighted, identified as transverse optic (2TO) at ~ 1000 cm^{-1} and longitudinal acoustic (2LA) at ~ 600 cm^{-1} scattering.

Similarly, the peak at 520 cm^{-1} (TO) corresponds to the first-order Raman active phonon that creates the 3-fold degeneracy long-wavelength transverse optical phonon [89]. Given the characteristics of Si mentioned

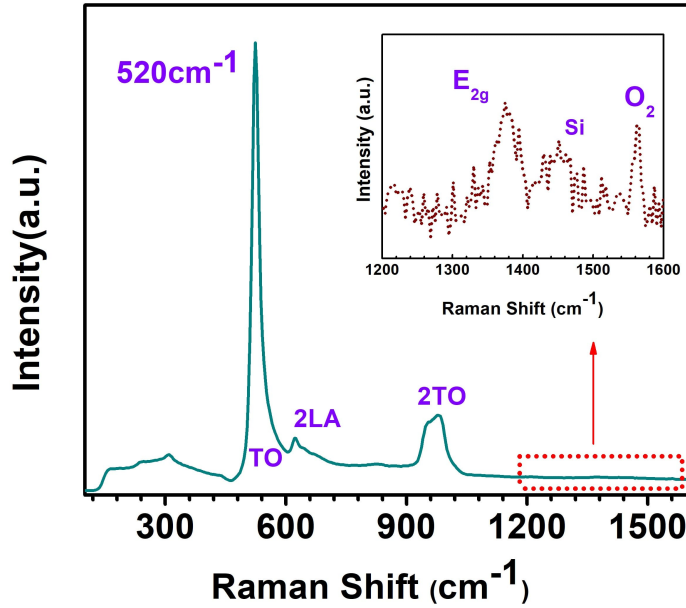


Figure 6.1: Raman spectrum of an h-BN film showing the entire region of Si characteristics in the range from 100 to 1600 cm^{-1} . The Si modes are characterized as the transverse optic (TO)- 520 cm^{-1} , second order longitudinal acoustic (2LA) and second order transversal optic (2TO). On the other hand, the inset Figure show the E_{2g} vibrational mode of h-BN, Si mode at 1450 cm^{-1} , and molecular Oxygen O_2 at ~ 1563 cm^{-1} .

above, it is crucial to consider the high-intensity Si signals, as observed in the quenching of the spectral peak of h-BN.

Furthermore, the inset of Figure 6.1 depicts the Raman spectrum of the dominant peak at ~ 1374 cm^{-1} ; this peak corresponds to the E_{2g} phonon mode, providing evidence of the hexagonal phase of BN in the deposited films. Other peaks corresponding to Si (at ~ 1450 cm^{-1}) and O_2 (at ~ 1563 cm^{-1}) can also be observed, with the latter attributable to the atmospheric environment.

Figure 6.2 (a) presents the Raman spectra obtained from samples grown at 10 min with temperatures of 1273, 1323, and 1373 k, respectively. Following the initial evaluation post-synthesis, Raman measurements conducted on samples grown below 1223 k exhibit an absence of characteristic h-BN signals. The observed peak at 1375 cm^{-1} corresponds to the vibration mode E_{2g} , which represents the phonon within the h-BN plane. This doubly degenerate optical phonon mode involves B and N atoms within each plane moving in opposite directions. As a result of the cancellation of contributions from the two planes, this mode does not exhibit an LO-TO splitting [90].

The observed peak exhibits shifts towards higher phonon frequencies in comparison to the bulk h-BN Raman peak located at 1366 cm^{-1} . These red and blue shifts in the Raman peak predominantly arise due to the presence of compressive and tensile strains within the films. The mismatch

Sample (K)	FWHM (cm^{-1})	L_a (nm)	X_c (cm^{-1})
1273	31 ± 2.1	-	1372
1323	20 ± 1.8	125.0	1369
1373	28 ± 2.5	73.0	1376

Table 6.2: Show the respective analysis parameter for the samples in the temperature range of 1273 to 1373 K. The FWHM values were used to estimate the crystallite sizes (L_a), and X_c is the peak position in cm^{-1} .

in the coefficients of thermal expansion (TEC) between h-BN and the silicon substrate likely induces compressive deformation in the samples, a finding that aligns with similar results reported in [91].

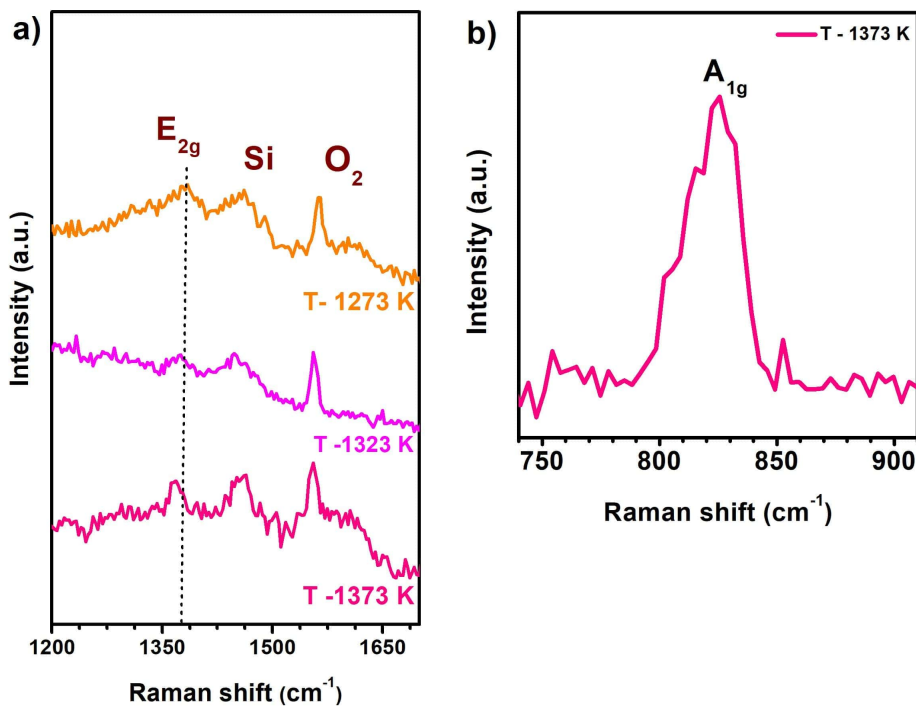


Figure 6.2: Raman spectra of h-BN samples grown in the temperature range of 1273 to 1373 K. In (a) shows the Raman spectra of the h-BN characteristic E_{2g} vibration mode, the dashed line shows that these peaks do not suffer significant shifts for blueshift or redshift. Including the peaks referring to the Si and the molecular oxygen peak, at ~ 1450 and O_2 , ~ 1563 cm^{-1} . (b) show the A_{1g} characteristic out-of-plane h-BN vibration mode observed in a sample grown for 5 minutes. It is noteworthy that the A_{1g} peak is consistently observed across all samples.

In Figure 6.2 (b), the vibration peak centered around 825 cm^{-1} (A_{1g} mode) is characteristic of the out-of-plane h-BN vibration [47]. The experimentally measured Raman peak of the h-BN samples was fitted using Lorentz functions, and the FWHM was estimated, as demonstrated in Table 6.2. Utilizing the obtained FWHM value, it is feasible to calculate the crystallite size

(L_a in nm) by applying the Nemanich Equation [92]:

$$L_a = 1417/(\Gamma_{1/2} - 8.7) \quad (6-1)$$

Here L_a is the crystallite size in angstroms and $\Gamma_{1/2}$ is the FWHM in cm^{-1} . The calculated values are shown in Table 7.2, and all spectra were fitted using a Lorentzian line shape. According to the empirical method, if the high frequency E_{2g} vibration mode of h-BN shifts from $\sim 1366 \text{ cm}^{-1}$ to a higher frequencies $\sim 1375 \text{ cm}^{-1}$ and broadens, it indicates that the crystallite size decreases. Therefore, the calculated FWHM of the Raman peak indicates the crystalline quality and estimates the size of the crystallite [92].

The estimated crystallite sizes for the samples grown at 1323 and 1373 K were 125.0 and 75.0 nm , which is consistent with the findings of morphological studies. Because the morphology of the sample grown at 1273 K exhibited a 2D nano-sheet-like structure, the L_a was not calculated.

6.2

UV- visible spectroscopy

Figure 6.3 illustrates the absorbance spectra and the corresponding energy gap E_g derived from the analysis of Tauc's equation (4.2) [68]. The E_g values for the samples grown at 1273 and 1373 K, are 5.7 and 5.6 eV.

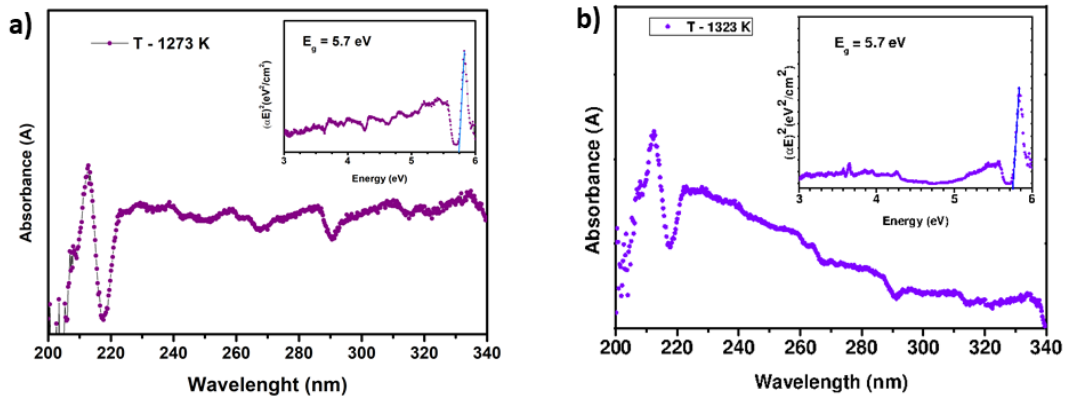


Figure 6.3: UV-Vis spectrum of h-BN film 10 min at 1273, and 1323 K on a Si substrate. The inset shows the optical bandgap analysis of the h-BN film. In (a) and (b) the E_g was 5.7 eV.

These values are lower than the theoretical E_g of 6 eV for an h-BN monolayer, indicating the growth of thin films. The decrease in E_g can be attributed to layer-layer interactions, resulting in increased electronic band dispersion and a tendency to reduce the bandgap [56, 5].

6.3 X-ray Photoelectron Spectroscopy (XPS)

To verify the elemental composition of the samples, X-ray Photoelectron Spectroscopy (XPS) was applied. Figure 6.4 displays the B $1s$ and N $1s$ regions for the samples in the temperature range of 1273 to 1373 K. The peaks were fitted with a Voigt lineshape and a Shirley background. The C $1s$ peak at 284.8 eV was applied to calibrate the entire spectrum.

Figure 6.4 (a) shows the deconvolution, and two main overlapping peaks are evident in the B $1s$ region. The first, at 190 eV, is characteristic of the B-N bonds, and the small shoulder of the B-N peak, located at 192 eV, is related to oxygen (B-O bonds).

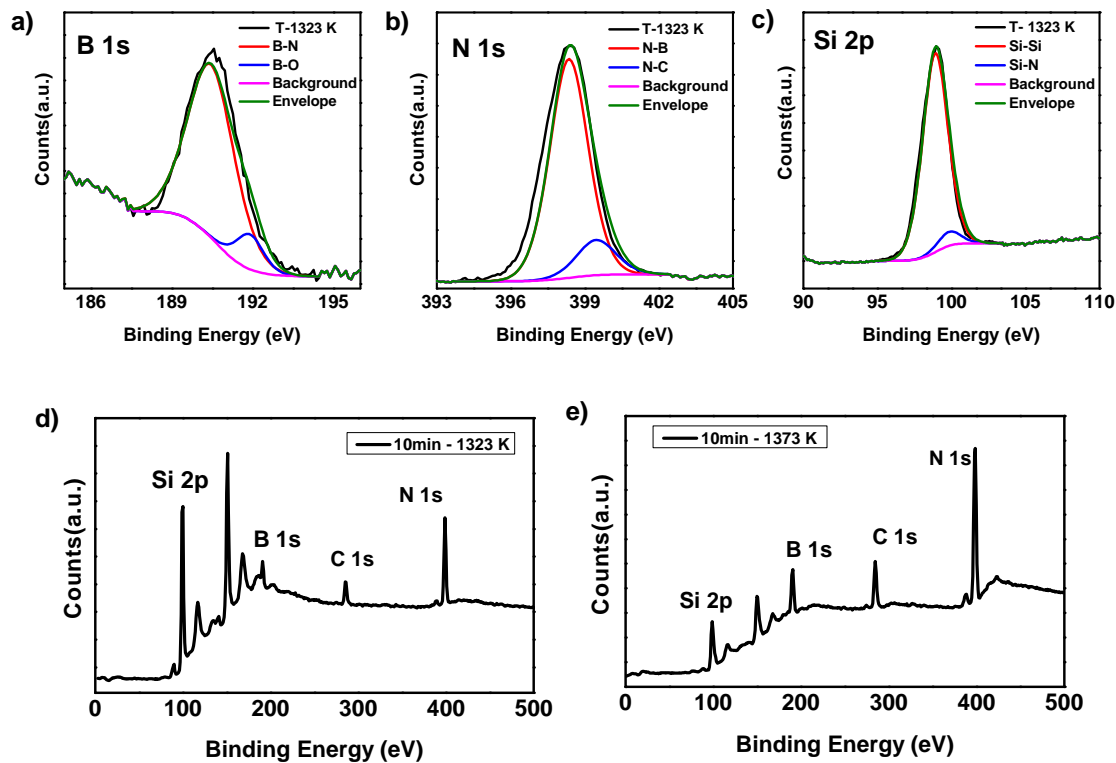


Figure 6.4: XPS spectra of the samples grown in the temperature of 1323, and 1373 K. In (a) show the B $1s$ spectrum of the B-N and B-O overlap (b) show the N $1s$ spectrum of the N-B and N-C overlap, and (c) show the spectra of the Si $2p$ (Si-Si at 99 eV and Si-N at 102 eV) regions of the as-grown sample at 1323 K. (d) and (e) highlight the Survey spectra of the elements in the region, Si $2p$, B $1s$, C $1s$ and N $1s$.

In Figure 6.4 (b), the two peaks are displayed, with the most intense being the N-B bonds at 398 eV, while the small shoulder of the N-B peak, at 400 eV, represents the N-C bonds, given the higher electronegativity of Carbon compared to Boron.

The stoichiometric B/N ratio was calculated and the results show 1.01, which is in good agreement with the theoretical value of 1.0. Are reported that one nitrogen atom is bonded to three boron atoms, and vice versa. The obtained values for the binding energy (BE) related to B-N and N-B bonds agree well with those reported in the literature [5, 91, 61].

Figure 6.4 (c) shows the plot for the Si $2p$ region for the sample grown at 1323 K, where two peaks are identified as Si-Si at 99.0 eV and Si-N [93] at 102.2 eV. The measurements were carried out one-month post-synthesis, revealing an absence of the peak typically associated with SiO_2 (103.3 eV) [94]. This suggests that h-BN coatings, even at thickness ~ 20 nm, effectively maintained the Si surface stable below the coating, without a discernible signal of silicon oxidation.

Taking a careful look at Figure 6.4 (d) and (e) for the survey of the as-grown samples at 1273 and 1373 K, a considerable difference is observed in the Si $2p$ signal for the two samples. The most intense Si $2p$ is related to a thinner film; that is, the decrease in the temperature parameter produces a film less thick.

6.4

Atomic Force Microscopy (AFM)

The surface topography of the films was analyzed with Atomic Force Microscopy (AFM). Figure 6.5 (a) shows the AFM image captured in semi-contact mode, with a scan size of $1 \mu m^2$. The image refers to the sample grown at 1273 K, showing a 2D nanosheet-like morphology. A similar result was found in reference [95]. In Figure 6.5 (b) show the 3D image.

The lateral coverage of the nanosheets varies between 50 - 400 nm, and the topography-based histogram, Figure 6.5 (d) shows the height distribution of the h-BN sheets with a median height of 3.0 ± 0.5 nm and the corresponding roughness root mean square (RMS) of 1.0 ± 0.2 nm.

Figure 6.6 (a) shows the AFM image for the as-grown sample at 1323 K, revealing the formation of a continuum film in Figure 6.6 (b) the 3D image, Figure 6.6 (c) the height in a point of defect where the height is 10.3 ± 1.5 nm. Figure 6.6 (c) the given height distribution and a median thickness of 10.5 nm and roughness RMS of 1.5 ± 0.3 nm.

Figure 6.7 (a) depicts AFM images of 10 min samples, captured in semicontact mode, highlighting the scan size of $1 \mu m^2$. A corresponding 3D plot is shown in Figure 6.7 (b). Figure 6.7 (c) shows the height of the film in a point without nucleation 17.0 ± 1.2 nm along the pink line direction, and Figure 6.7 (d) show the height distribution histogram with height up to 20 nm,

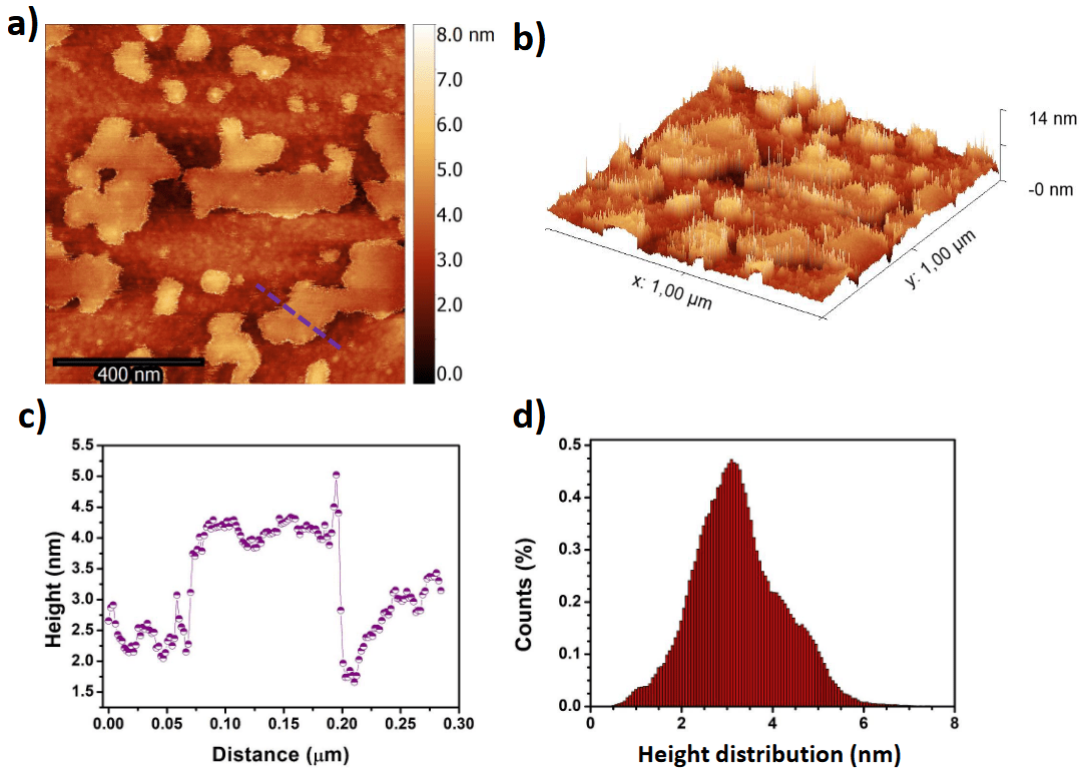


Figure 6.5: AFM images of h-BN films with a scan size of $1 \mu\text{m}^2$ at 1273 K. In (a) shows the 2D nanosheet-like structures with the roughness of $RMS = 1.0 \pm 0.2 \text{ nm}$, (b) the 3D image, (c) the height of the 2D nanosheet of $2.5 \pm 0.6 \text{ nm}$ and (d) the height distribution with the main lying on 3.0 nm .

the negative values in the histogram are related to the rough substrate, cracks, holes, and shallow depressions.

Considering the three samples, there are clear differences in morphology as the temperature changes. The formation of extrusions, known as ‘hillocks’, is observed. These features are higher than the film itself and affect the roughness of the samples. The formation of ‘hillocks’ is related to the compressive stress resulting from the mismatch in the thermal expansion coefficients between h-BN and the substrate. In [96] they observed a similar structure.

As seen, temperature plays a crucial role in the growth kinetics, including species desorption and diffusivity on and within the catalyst substrate. It also affects the density of the nucleation and the size of the grain. The growth process involves several complex steps, including the vaporization and transport of precursors to the substrate, the decomposition of precursors, the migration of species to the substrate, nucleation, and crystal growth [95].

In general, elevated growth temperatures tend to result in a process that is thermodynamically limited by mass transfer, whereas lower growth temperatures are associated with a kinetic process controlled by surface reactions. Lower growth temperatures exhibit significantly higher reactant

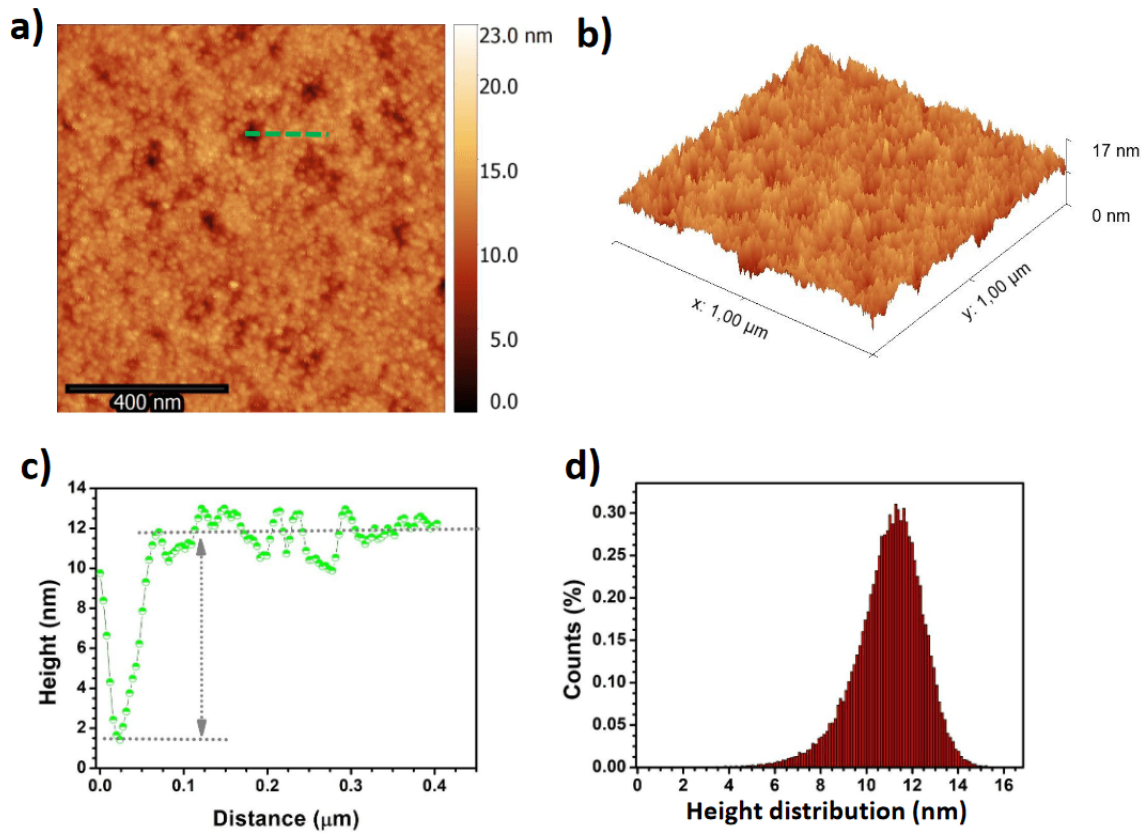


Figure 6.6: AFM images of h-BN films with a scan size of $1 \mu\text{m}^2$ at 1323 K. In (a) the obtained roughness was $\text{RMS} = 1.5 \pm 0.3 \text{ nm}$, (b) the 3D plot, (c) indicates the height of a point without nucleation of $10.3 \pm 1.5 \text{ nm}$ taken from (a) in the green dashed line, (d) shows the height distribution with the main lying on $10.5 \pm 1.0 \text{ nm}$.

surface adsorption compared to higher temperatures, leading to a notable increase in nucleation events but hindering grain size [97].

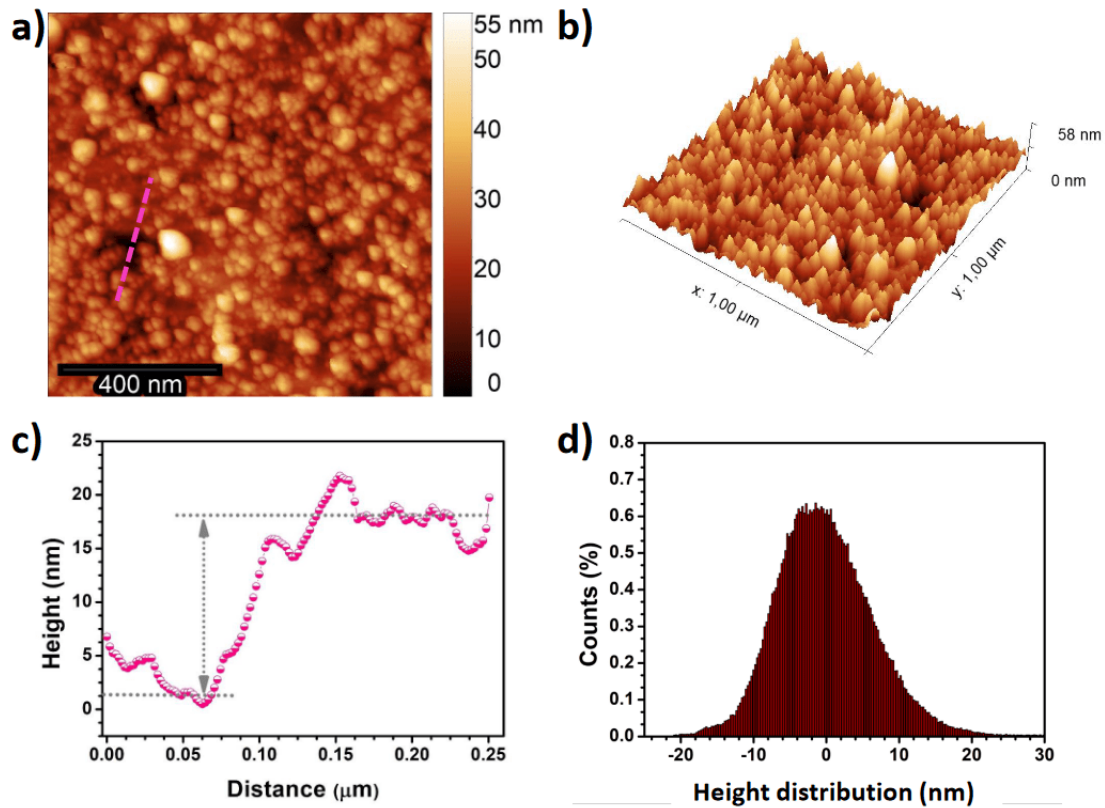


Figure 6.7: AFM image showing the topography of the 10 min sample of an area of $1\mu\text{m}^2$, (a) showing almost total coverage of the substrate surface. The grain analysis shows the respective $\text{RMS} = 6.8 \pm 1.3 \text{ nm}$ roughness. In (b) a 3D image of the film surface, (c) the height of the film of $17 \pm 0.8 \text{ nm}$ along the pink line direction in a region without nucleation, and (d) the histogram of the height distribution of the h-BN film ranging from 0 to 20 nm.

6.5 Scanning Electron Microscopy (SEM)

The sample surface was also analyzed by scanning electron microscopy (SEM). Figure 6.8 shows the h-BN images for samples grown at 1273, 1323, and 1373 K.

As the growth time increases, different surface morphologies are observed, which is consistent with AFM studies. Specifically, for the sample at 1273 K, 2D nanosheet structures are formed; the lateral coverage is around 80-500 nm.

Then, for the sample at 1323 K, a continuous and smooth film is formed on the Si surface. Finally, the sample at 1373 K presents a continuum film, and 3D structures are formed along the Si surface.

As mentioned above, the significance of the substrate temperature lies in providing extra energy for these species to move onto the surface, merge, and establish bonds with the substrates, thereby enhancing nucleation and subsequent crystallinity [95]. Furthermore, this temperature promotes the

formation of structures on the surface of the substrate, as illustrated in the Figure 6.8 (a-e) with a scale of $10\ \mu\text{m}$.

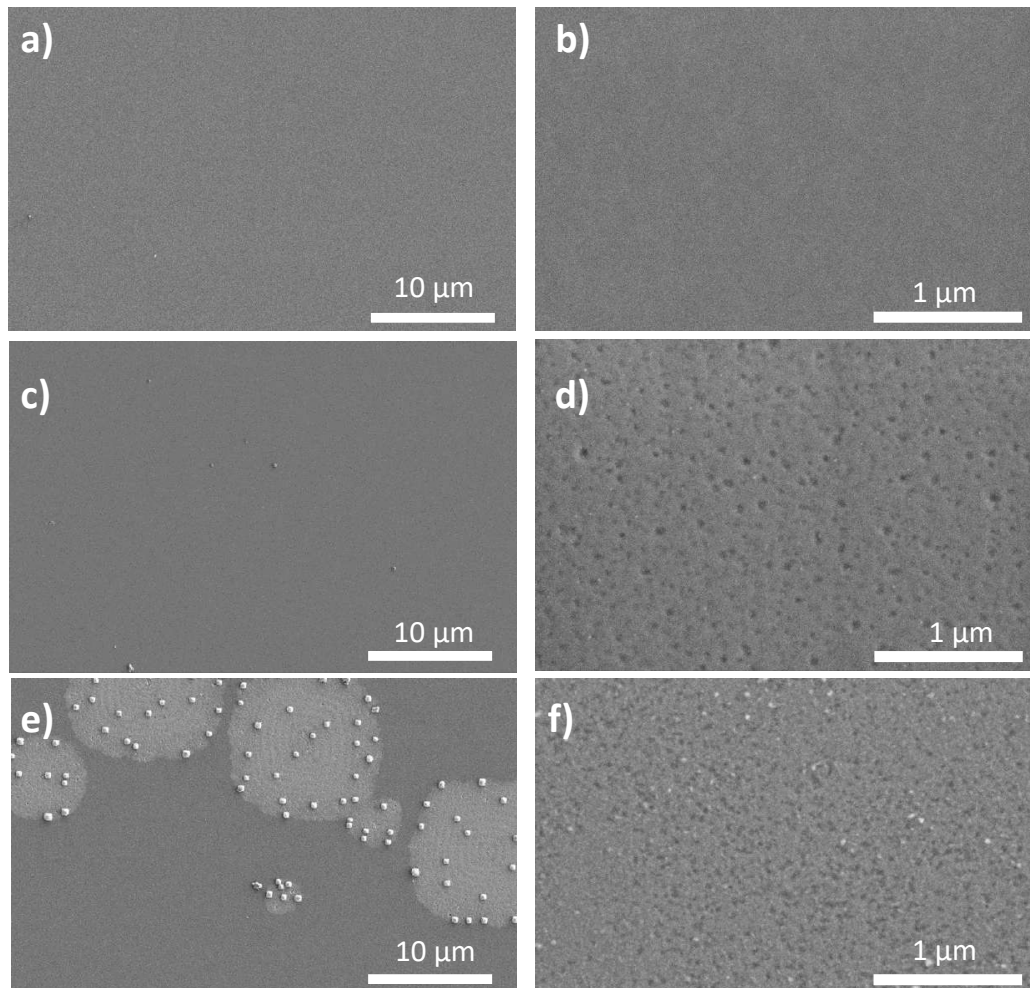


Figure 6.8: Scanning electron microscopy (SEM) images of h-BN samples in the temperature range of 1273 to 1373 K. (a-b) show at 1273 K sample. (c-d) depict sample grown at 1323 K showcasing this point defects on the film's surface. (e-f) exhibiting a circular pattern for the samle at 1373 K characterized by small aspect ratios, identified as "hillocks" features with a brighter contrast (white).

6.6

Contact Angle

The wettability of the samples was investigated by contact angle measurements. Consequently, the samples exhibited hydrophobic behavior, with θ values of $84.0^\circ \pm 1.0$, $76.0^\circ \pm 3.0$, and $105.0^\circ \pm 5.0$ at 1273, 1323, and 1373 K, respectively. The measured CA of the bare Si substrate was $\theta = 61.0^\circ \pm 1.0$, signifying its hydrophilic nature. Considering the polar character of the BN bond ($-N - B + -$), Annamalai *et al.* (2015) [98] noted that wettability is strongly influenced by Van der Waals (vdW) interactions. Another noteworthy parameter influencing wetting characteristics is surface roughness, which is inherent to wetting phenomena.

However, in this case, the surface roughness of the as-grown h-BN measures within a few nanometers (1-7 nm). The impact of roughness on the contact angle is not significant, which means that it depends solely on the surface energy of the h-BN samples. The results are consistent with those reported in [95].

6.7

Tribology

In this section, we discuss the effect of reducing the treatment time of the silicon substrate with HF from 1 minute to 10 seconds. The properties of the resulting films were studied using various analytical techniques, including Raman spectroscopy, Fourier-transform infrared spectroscopy (FTIR), atomic force microscopy (AFM), tribology, and X-ray photoelectron spectroscopy (XPS).

6.7.1

Raman spectroscopy

The samples were grown for 1 hour at 1373 K on the Si substrate after cleaning with HF for 10 seconds. The substrate cleaning time positively influenced the quality of the deposited films, as it did not result in the formation of structures identified as hillocks, which have heights greater than the surface of the film. In previously grown films, these structures were observed to form in pits on the substrate, possibly caused by acid treatment during the removal of the thin native oxide layer.

Figure 6.9 shows the Raman spectra for samples grown for 1 hour at temperatures ranging from 1273 to 1373 K. Three peaks are highlighted in the range of 1300 to 1600 cm^{-1} , marked a $E_{2g} \sim 1375 cm^{-1}$, characteristic of the material grown in the hexagonal phase, and Si, corresponding to the substrate.

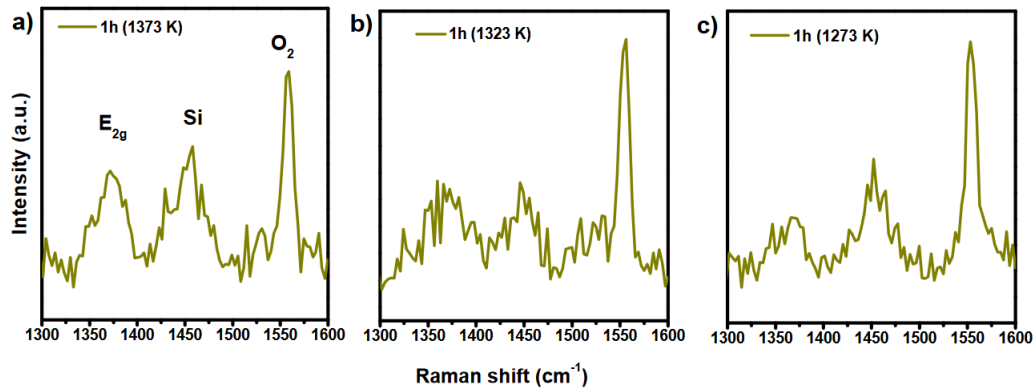


Figure 6.9: Raman spectra of the as-grown h-BN samples. (a), (b) and (c) displays the characteristic vibrational mode E_{2g} at approximately 1375 cm^{-1} .

In addition, the peak corresponding to O_2 and, referring to molecular oxygen, is indicated.

The presence of the silicon peak suggests that a thin film was formed despite the long growth time, due to the limiting factor of the precursor amount, which was maintained at 8 mg . The width of the Raman peaks was $\text{FWHM} = \sim 25\text{ cm}^{-1}$, these values are significantly larger than those observed for an exfoliated monolayer BN flake, which typically has a FWHM of ~ 10 to 12 cm^{-1} [11].

6.7.2

Fourier-transform infrared (FTIR) spectroscopy

The results of Raman spectroscopy were confirmed with FTIR, as shown in Figure 6.10 displaying the spectra for the three samples. The transmittance peak of the B-N bonds is observed at approximately 1375 cm^{-1} .

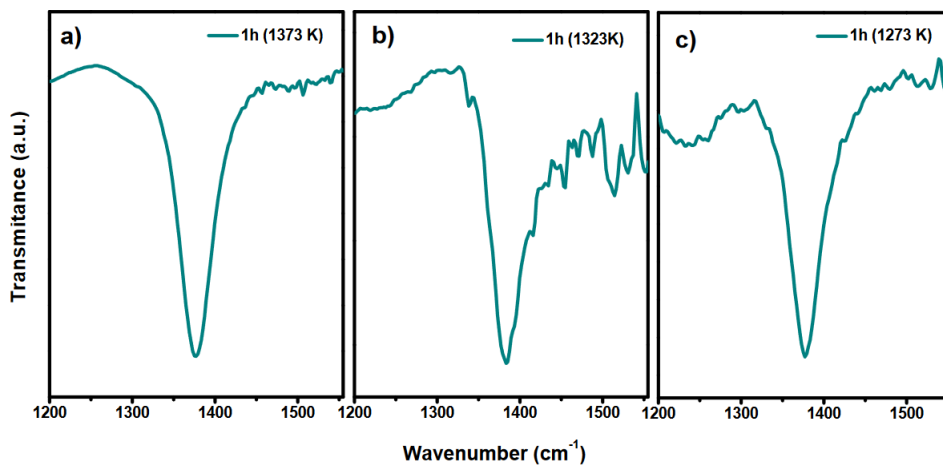


Figure 6.10: Vibrational spectra obtained from FTIR spectroscopy. (a), (b) and (c) shows the corresponding absorption peak at 1375 cm^{-1} .

6.7.3 AFM

Figure 6.11 shows the analysis of the sample grown at 1373 K for 1 hour by AFM. The measurement was performed in contact mode. Figure 6.11 (a) presents the topography of the sample at 1373 K with a scan size of $1 \mu\text{m}^2$ and a roughness of $7.7 \pm 2.1 \text{ nm}$. Figure 6.11 (b) shows the corresponding 3D profile of the image in Figure 6.11 (a). In Figure 6.11 (c), the film height was measured from a defect point in the film where no material nucleation occurred, resulting in a measured value of $38.2 \pm 1.5 \text{ nm}$, which is close to the average height distribution in this $1 \mu\text{m}^2$ area of $\sim 40 \text{ nm}$ as shown in Figure 6.11 (d).

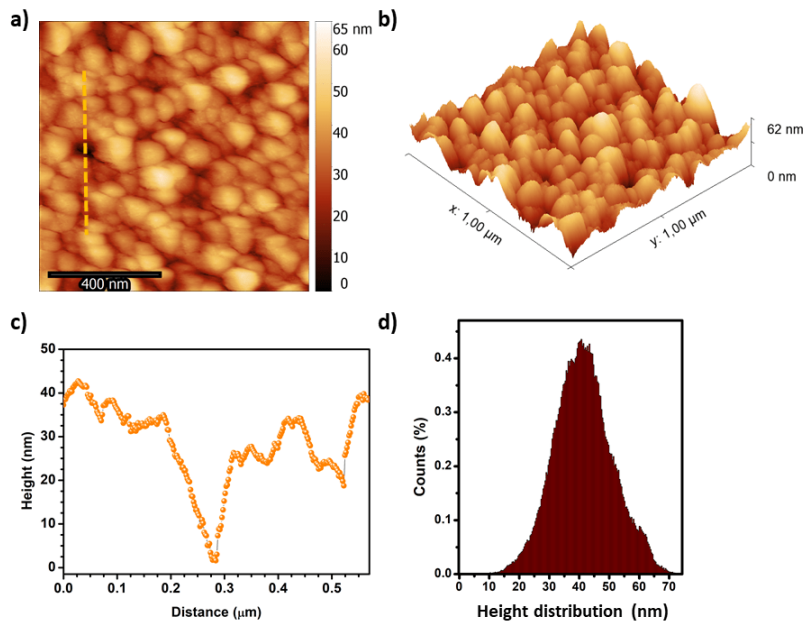


Figure 6.11: AFM images of the h-BN sample grown on Si at 1373 K for 1 hour are shown. (a) Displays the sample morphology with a root mean square (RMS) roughness of $7.7 \pm 2.1 \text{ nm}$, (b) the corresponding 3D profile, (c) the height profile of $30.0 \pm 5.3 \text{ nm}$ taken from the vertically dashed line indicated in (a), and (d) the height distribution, with the main peak lying at 40 nm .

AFM measurements with a scanned area of $10 \mu\text{m}^2$ showed that the surface topography of the film increased in RMS roughness (R_q) from $1.5 \pm 0.2 \text{ nm}$ for samples at 1273 K to $1.99 \pm 0.1 \text{ nm}$ for samples at 1323 K and $12.8 \pm 2.6 \text{ nm}$ for samples at 1373 K (Figure 6.12). This indicates an increase in surface irregularities as the temperature increases. The AFM images with larger scan areas did not show the presence of hillocks on the film surface with heights in the order of 300 nm , as observed in previous films.

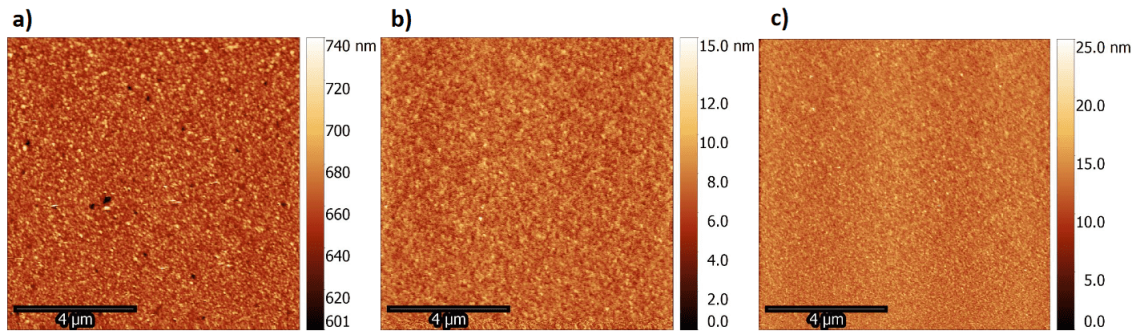


Figure 6.12: AFM images of the h-BN sample grown on Si for 1 hour are shown. Displays the sample topography with a root mean square (RMS) roughness of (a) $12.8 \pm 2.6 \text{ nm}$, (b) $1.99 \pm 0.1 \text{ nm}$, and (c) $1.5 \pm 0.2 \text{ nm}$ for the samples at 1373, 1323 and 1273 K, respectively.

6.7.4 XPS

The elemental composition of the film grown at 1273 K for 1 hour was studied using XPS. The Figure 6.13 shows the peaks in the B $1s$ region at 398 eV and the N $1s$ region at 190 eV, respectively. The contributions from B-O and N-C bonds are also displayed in the deconvolution of the main peaks. Finally, the B/N stoichiometric ratio was calculated, yielding a value of 1.02, which aligns closely with the theoretical value of 1.0.

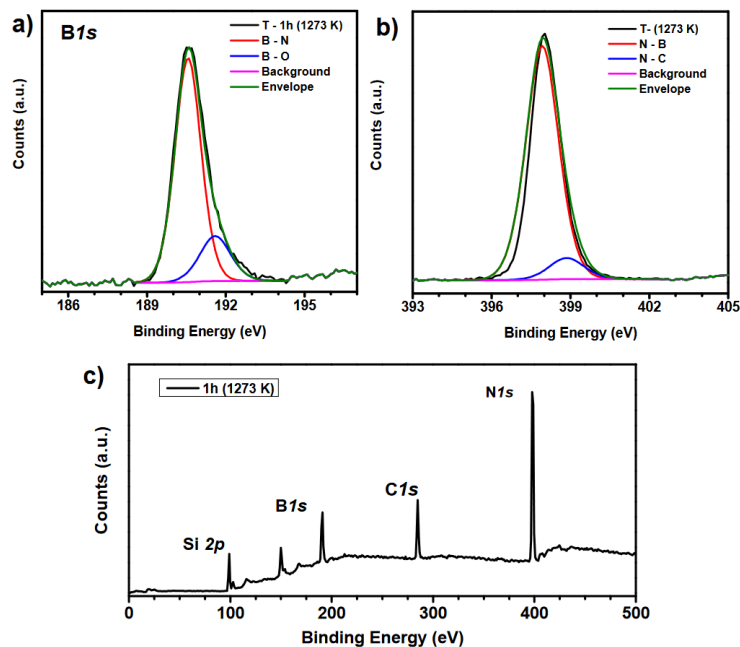


Figure 6.13: XPS spectra of the sample grown at 1273 K for 1 hour. In (a) show the B $1s$ spectrum of the B-N and B-O overlap, (b) show the N $1s$ spectrum of the N-B and N-C overlap, and (c) highlight Survey spectra of the elements in the region, Si $2p$, B $1s$, C $1s$ and N $1s$.

6.7.5

Tribology test

Figure 6.14 illustrates the tribology test results for the Silicon <100> substrate and the Si coated with h-BN (h-BN/Si) grown at 1273, 1323, and 1373 K for 1 hour. The study primarily determined the coefficient of friction (CoF) for Si, which yielded a CoF of 0.6. In contrast, the CoF of the samples did not exceed the value of 0.2.

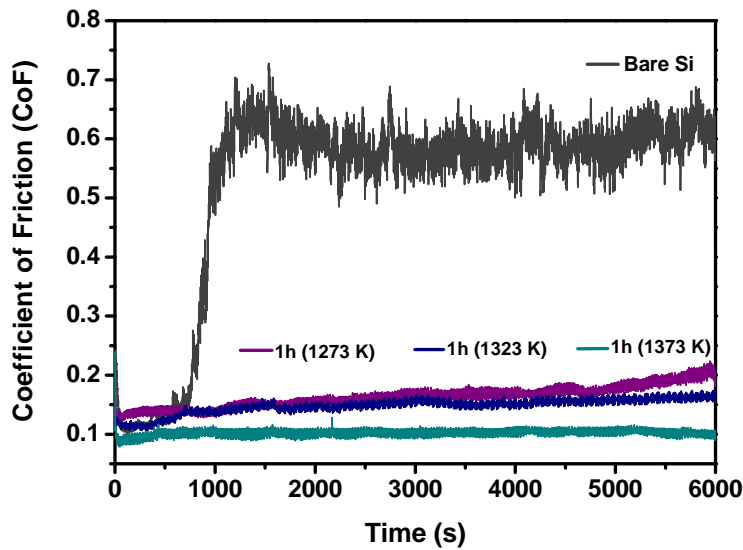


Figure 6.14: Presents the results obtained from the tribology test conducted on the Si <100> substrate and Si coated with h-BN (h-BN/Si) samples grown at 1 hour at 1273, 1323, and 1373 K, respectively. Under linear reciprocating ball-on-disc test. The test involved a constant sliding speed of 10 mm/s, a 10 mm sliding distance, and a corresponding Hertzian pressure of 398 MPa, displaying the variation of the coefficient of friction (CoF) with time (s).

The CoF of Si experienced a significant increase before stabilizing around 0.6. This sudden increase in friction coefficient is related to catastrophic failure and substantial plowing of the ball into the sample, resulting from the mechanical contact exerted on the Si surface, indicating a high wear rate during the first 20 minutes of measurements.

Additionally, material removal occurred through ploughing, producing curly ductile chips, and some surface material along the scratch edges was plastically torn away, indicating that scratching primarily involved plastic deformation typical of ductile materials [99]. Once stabilized, the CoF remained unchanged over the last 1 hour and 20 minutes of measurement. On the other hand, the CoF of the h-BN/Si, at 1373 K, material maintained a constant linear rate of 0.1 for 1 hour and 40 minutes of the test duration. The CoF of

the other samples grew at a low linear rate and did not exceed the value of 0.2.

The h-BN appears to form an adherent film on the Si surface, as observed during the test where the material did not detach from the substrate under mechanical wear. Figure 6.15 (b, d), and Figure 6.16 (b, d) shows the scratch height profiles taken at the end of the test. For h-BN/Si, a reduction in the scratch height is observed, indicating high wear resistance and lower CoF for the coated Si with the h-BN film. The Si height profile indicates a depth of $1340 \pm 5.7 \text{ nm}$, .

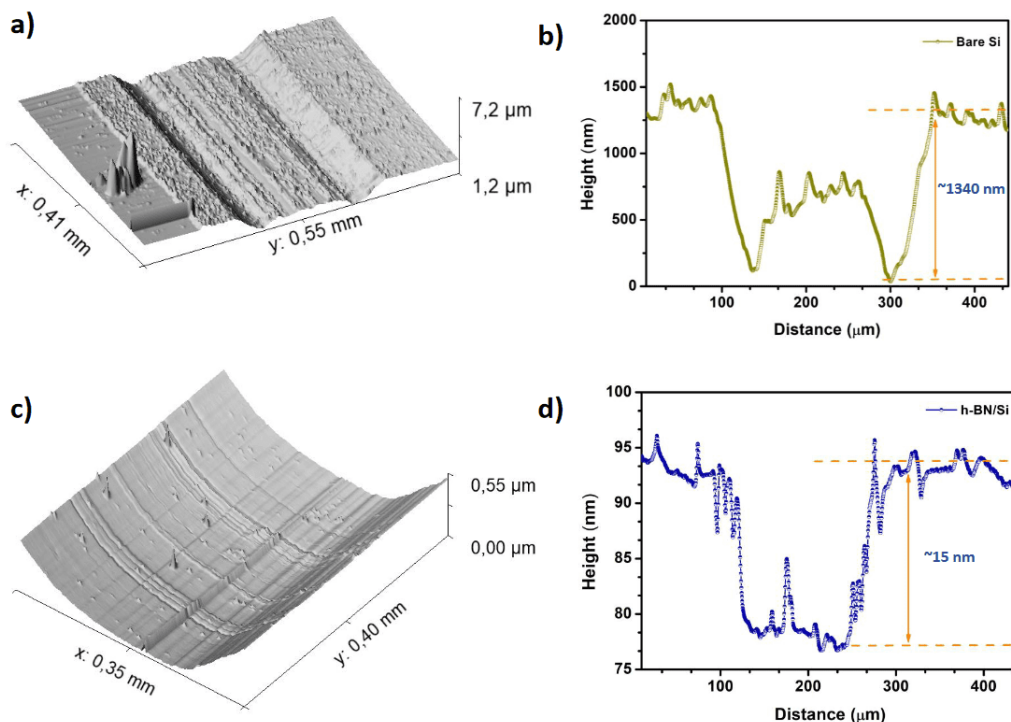


Figure 6.15: Study of Wear tracks through Profilometry. (a) A 3D profile of the wear track from the tribology test of a bare Si substrate, (b) The height of the scratch corresponding to (a), indicating a depth of $\sim 1340 \text{ nm}$, (c) A 3D profile of the wear track of the 1373 K (sample), and (d) The height of the scratch corresponding to (c), indicating a depth of $\sim 15.7 \text{ nm}$.

This suggests that h-BN maintains its frictional properties due to its chemical and thermal stability, high resistance to oxidation at elevated temperatures, and effective lubrication capability, even under a constant linear load of 0.3 N corresponding to a constant Hertzian pressure of 398 MPa. Additionally, the material exhibits high thermal conductivity, contributing to improved dissipation of frictional heat across the entire sample surface, thereby effectively reducing negative thermal effects on the CoF.

Therefore, h-BN emerges as a promising film for use as a solid lubricant to enhance the tribological properties of materials, including CoF, wear rates,

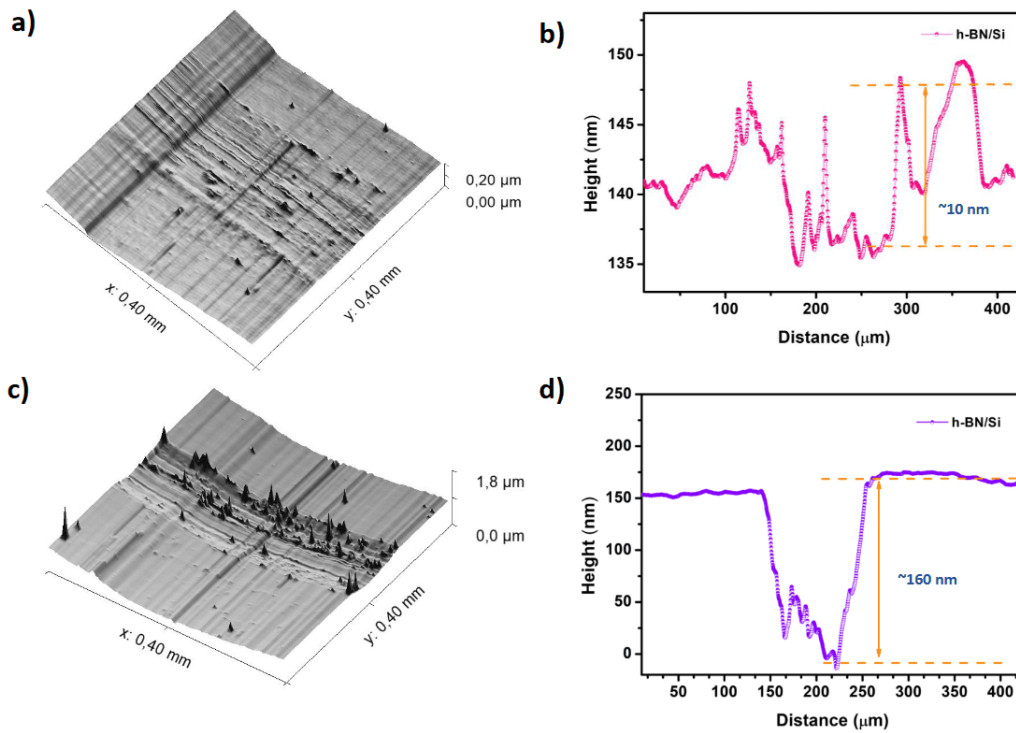


Figure 6.16: Study of Wear tracks through Profilometry. (a) A 3D profile of the wear track from the tribology test for 1323 K (sample), (b) The scratch height corresponding to (a) of ~ 10 nm, (c) A 3D profile for 1273 K (sample), and (d) The height of ~ 160 nm.

and high-temperature efficiency. The lubricating properties of solid lubricants are attributed to their crystalline structure layered with weak Van der Waals bonding, allowing these layers to slide over each other with minimal applied force, resulting in low friction properties.

6.8

Summary

The h-BN films were synthesized at varying temperatures. Characterization techniques were used to elucidate the effect of growth temperature on the films. Films with the formation of different structures were observed on the Si surface. Growth is observed from 1273 K, while samples grown below 1223 K do not show signs of growth. We observed the formation of two-dimensional (2D) sheets with lateral dimensions ranging from 80 to 500 nm, as well as the continuous growth of films with nanocrystals of varying sizes. After understanding possible factors that affect the quality of the films, better quality was observed in films grown for 1 hour by varying the temperature. These films were subjected to tribology tests and showed promise in the application of solid lubricants, since the coefficient of friction was kept low during the test.

7

Time-dependent growth of h-BN films

In this section, the results obtained for h-BN films synthesized at 1373 K through low-pressure chemical vapor deposition (LPCVD) on Si <100> substrates, using the AB complex as a precursor, are presented. The Table 7.1 below shows the set of samples grown from 2 to 20 min and the growth conditions. The temperature of 1373 K was chosen for the growth of the films despite being favorable for the growth of hillock structures, as the samples showed better crystallinity observed through vibrational analyses. The investigation was carried out using different complementary characterization techniques, including Raman spectroscopy, infrared spectroscopy (FTIR), X-ray photoelectron spectroscopy (XPS), atomic force microscopy (AFM), contact angle measurements, scanning electron microscopy (SEM), and UV-visible spectroscopy to confirm the growth and quality of the h-BN films.

Time (min)	Growth	Conditions
02	No	- Borane ammonia (8 mg) at 373 K
05	Yes	- Base/Working pressure ($10.7/5.3 \times 10^3$ Pa)
10	Yes	- Ramp up H_2 (50 sccm)
20	Yes	- H_2 /Ar flow (2/100 sccm) - Temperature (1373 K)

Table 7.1: The set of samples grown from 2 to 20 min and the growth conditions.

7.1

Raman spectroscopy

Figure 7.1 (a) shows the corresponding Raman spectra obtained at room temperature for the h-BN films as a function of growth time and temperature. These spectra required a longer integration time (500-900 s) for acquisition due to the higher signal emanating from the Si surface. Samples grown in less than 5 minutes did not show a Raman signal. In Figure 7.1 (b), the vibration peak centered around $\sim 827 \text{ cm}^{-1}$ (A_{1g} mode) is characteristic of the out-of-plane h-BN vibration, observed consistently across all samples [47].

The Raman spectra of the h-BN films exhibit a dominant peak at $\sim 1370.0 \text{ cm}^{-1}$. The peak intensity increases with the growth time, as evidenced in the sample range of 5-20 minutes, where the E_{2g} vibrational mode is more intense for the 20-minute sample than to the 5-minute sample, both grown at 1373 K.

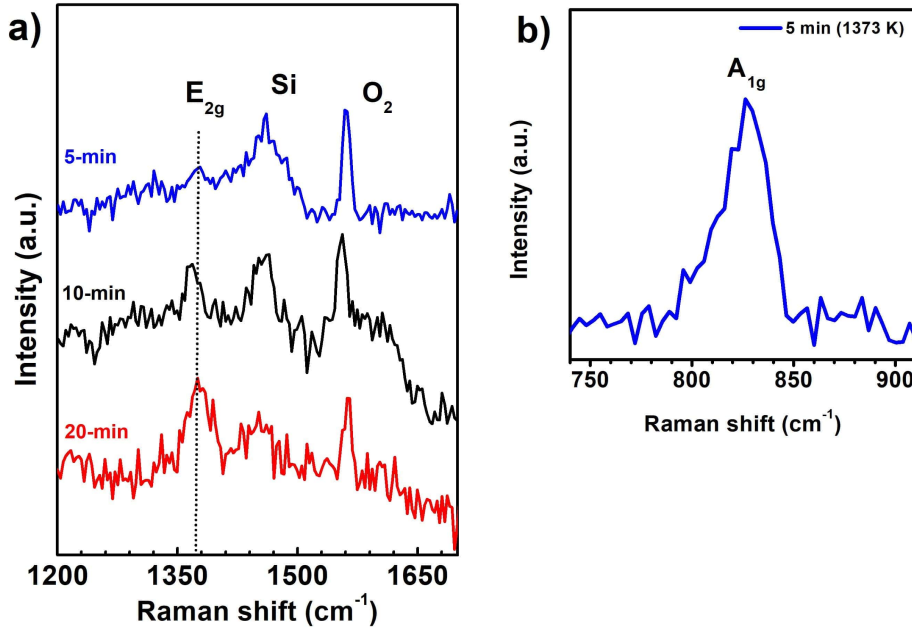


Figure 7.1: Raman spectra of h-BN samples grown at 1373 K variation in growth time between 5, 10, and 20 minutes under Si substrate. In (a) shows the Raman spectra of samples with different growth times the characteristic E_{2g} vibration mode, the dashed line shows that these peaks do not suffer significant shifts for blueshift or redshift. Are highlighted peaks referring to the silicon substrate and the molecular oxygen peak, at ~ 1450 and O_2 , ~ 1563 cm^{-1} . In (b) show the A_{1g} relative to the out-of-plane h-BN vibration mode sample grown at 5 minutes. The A_{1g} peak is present in all samples.

This suggests a potential correlation with increasing film thickness, as Raman intensity is proportional to the number of layers in h-BN [11]. The Full Width at Half Maximum (FWHM) was determined from the Raman spectral lines (Table 7.3), and the Nemanich model was applied to study the size of crystallites of BN [92], Equation 6-1 [92].

Similar study of crystallite size was found in other reports of h-BN films on Si $\langle 111 \rangle$ with an estimated value of ~ 9 nm for crystallite size [90], on Ge $\langle 001 \rangle$ /Si substrates, with values varying from 2-3 nm [91], also grown by atomic layer deposition (ALD) on Si $\langle 001 \rangle$ and sapphire substrates oriented $\langle 0001 \rangle$ with an estimated size of ~ 5 nm [43], and on Si and Sapphire substrates found with a value of ~ 6 nm [52].

Sample (min)	FWHM (cm^{-1})	L_a (nm)	X_c (cm^{-1})
05	18.4 ± 2.4	146	1372
10	28.0 ± 2.5	73.0	1369
20	35.5 ± 3.2	53.0	1376

Table 7.2: Show the respective analysis parameter for the samples grown at 5, 10 and 20 minutes (1373 K). The FWHM values in cm^{-1} were used to estimate the crystallite sizes (L_a), and X_c is the peak position in cm^{-1} .

7.1.1 FTIR spectroscopy

Fourier transform infrared (FTIR) spectroscopy is also a valuable technique for analyzing the h-BN lattice vibration modes resulting from stretching bonds between Nitrogen and Boron atoms. Figure 7.2 presents FTIR spectra for an h-BN film grown at 10 minutes (1373 K).

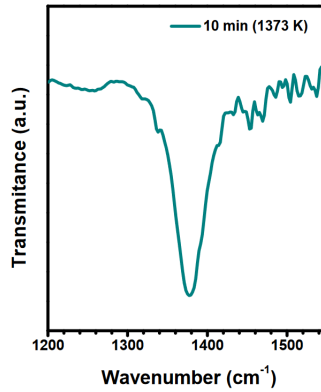


Figure 7.2: Infrared transmission spectra of films grown at 10 min (1373 K). The absorption band at $\sim 1373.2 \text{ cm}^{-1}$, is attributed to B-N bonds characteristic of the in-plane ring vibration.

The prominent absorption band, centered at $\sim 1373.2 \text{ cm}^{-1}$, is attributed to the in-plane ring vibration, [47] therefore confirming the existence of B-N bonds.

7.2 XPS

The chemical composition of the deposited h-BN films was examined using X-ray Photoelectron Spectroscopy (XPS) measurements. The spectra for $N1s$ (Nitrogen) and $B1s$ (Boron) regions are presented in Figure 7.3 for the as-grown h-BN films at 5, 10 and 20 minutes (1373 K).

All spectra underwent a peak-fitting process using a Voigt lineshape and a Shirley background were used for convolution, for better observation and

clarity. Furthermore, the C $1s$ core-level peak at 284.8 eV was used to calibrate all the spectra.

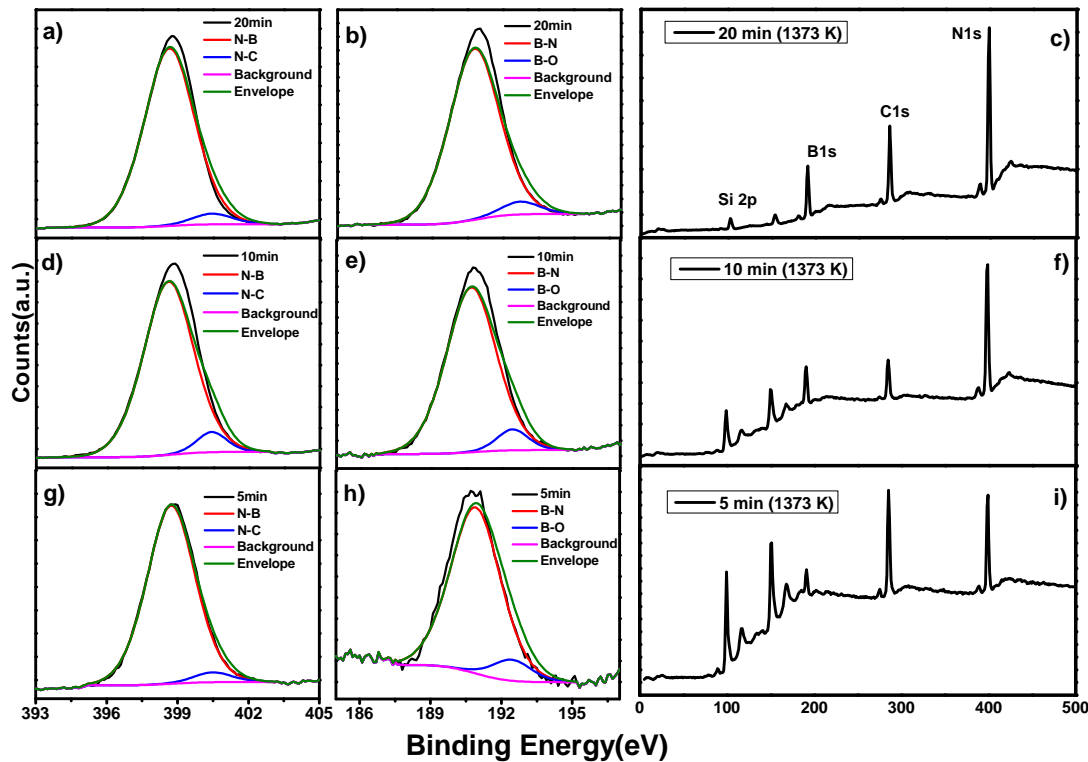


Figure 7.3: XPS spectra of the samples in the range of 5-20 min growth at 1373 K. In (a) are the N $1s$ spectrum of the N-B and N-C overlap, (b) the B $1s$ spectrum of the B-N and B-O overlap, and (c) the from the Survey highlighting the elements in the region, Si $2p$, B $1s$, C $1s$ and N $1s$ for the 20 min sample. In (d-i) show the N $1s$, B $1s$ and Survey spectra for the 10 and 5 min samples, respectively.

The findings are shown in Figure 7.3 (a, d, g), where the N $1s$ region shows two overlapping peaks observed for all samples. These peaks are attributed to the contributions of N-B bonds at ~ 398.6 eV, and the peak located at ~ 400 eV is the contribution of N-C bonds, as the electronegativity of carbon is higher compared to Boron [100]. Similarly, in Figure 7.3 (b, e, h), two overlapping peaks are observed attributed to B-N bonds in the B $1s$ region for all samples at ~ 190.8 eV, while the other peak at ~ 192 eV is relative to oxygen bonds [101].

Considering the B-N and N-B bonds, it is noteworthy to mention that one nitrogen atom is bonded to three boron atoms. Analogously, a boron atom is bonded to three nitrogen atoms [101, 102, 61, 100], as schematically shown in the inset of Figure 7.3 (a, b) for the B $1s$ and N $1s$ regions.

The values obtained are shown in Table 7.3 for the binding energy (BE) related to the B-N and N-B bonds are well aligned with those reported in the literature [53, 90, 91]. The measured B/N ratio of the h-BN films obtained in this study was close to 1.01, this value was achieved by area quantification,

Sample (min)	Pos. B-N (eV)	Pos. N-B (eV)	At (ratio)
05	190.9	398.7	1.04
10	190.7	398.6	1.01
20	190.8	398.6	1.02

Table 7.3: Position of the B-N and N-B peaks in the B $1s$ and N $1s$ regions, respectively. And stoichiometric atomic ratio of B and N atoms obtained by area quantification, using the factor RSF = 0.486 (B) and RSF = 1.8 (N).

applying the relative sensitivity factor (RSF) of variables B and N, which aligns well with the theoretical stoichiometric values of 1.0 (Table 7.3).

Figures 7.3 (c, f, i) present the survey spectra in the energy range of 0 to 500 eV, highlighting the regions of interest for atomic analysis. Examination of the Si $2p$ region reveals a noticeable decrease in film thickness corresponding to a reduced growth duration. This deduction is supported by a qualitative evaluation of the Si $2p$ peak intensity, demonstrating a gradual decrease in Si-specific characteristics as growth time diminishes.

The plot of the Si $2p$ region referring to Figure 7.4 shows two peaks identified as Si-Si at ~ 99.0 eV and Si-N [93] at ~ 102.2 eV. The measurements were performed one month after synthesis and did not show the peak associated with SiO_2 (103.3 eV) [94]. This indicates that h-BN coatings, even at dimensions of approximately 20 nm, keep the Si surface below the coating stable without a signal of silicon oxidation.

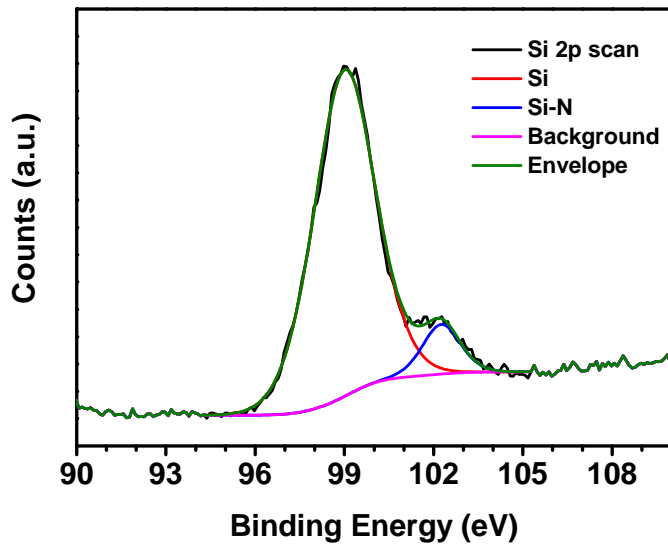


Figure 7.4: XPS spectra of the Si $2p$ (Si-Si at 99 eV and Si-N at 102 eV) regions of the as-grown sample at 10 minutes.

7.3 AFM

The topography of the samples was studied using Atomic Force Microscopy (AFM). Figure 7.5 (a) depicts AFM images of 5 *min* sample, captured in semicontact mode, highlighting the scan size of $1 \mu\text{m}^2$. A corresponding 3D plot is shown in Figure 7.5 (b). Figure 7.5 (c) show the height of the hillock of $\sim 65 \text{ nm}$ along the cyan line direction, and Figure 7.5 (d) show the height distribution histogram the main lies on $\sim 35 \text{ nm}$.

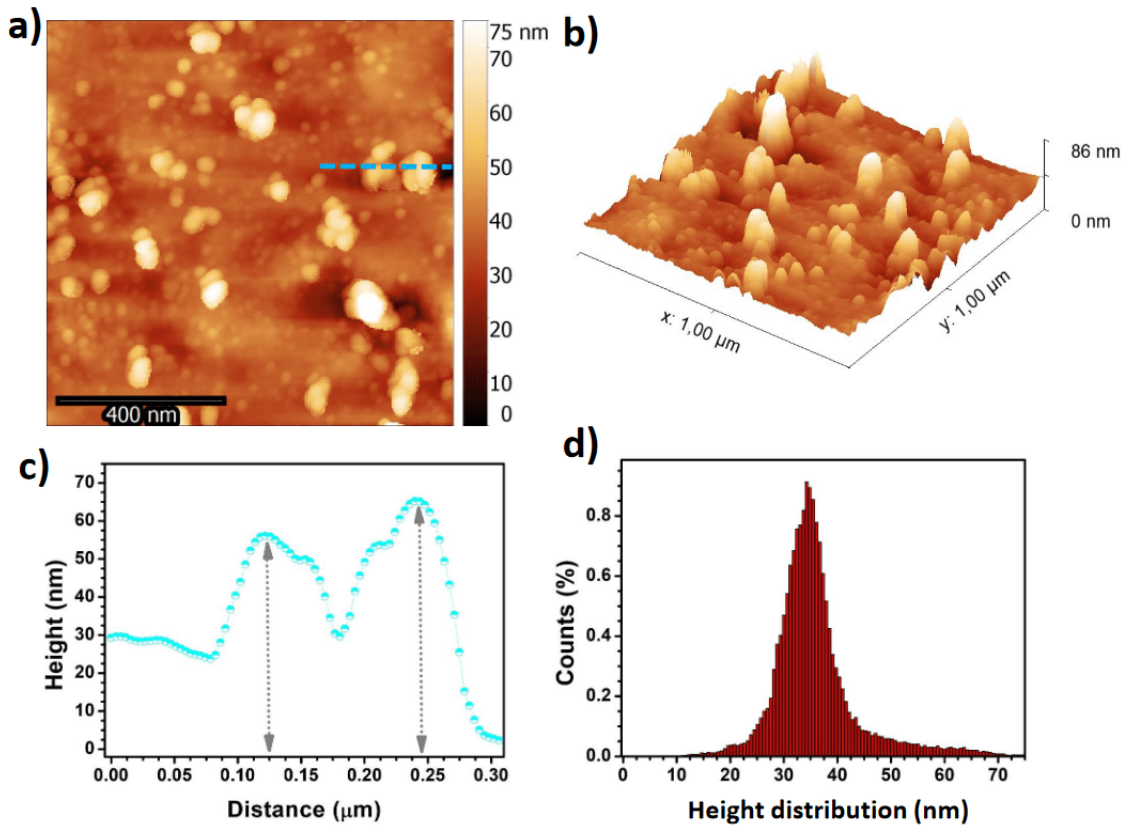


Figure 7.5: AFM image showing the topography of the 5 *min* sample of an area of $1 \mu\text{m}^2$, (a) showing the surface with features identified as "hillock". The grain analysis shows the respective $\text{RMS} = 8.4 \pm 3.0 \text{ nm}$ roughness. In (b) show a 3D image of the film surface, (c) the height of the "hillock" of $\sim 68 \text{ nm}$, and (d) the histogram of the height distribution ranging from 20 to 70 *nm*, indicating the rapid promotion of this features.

Figure 6.7 (Section 6.4) shows the AFM image for the as-grown sample at 1373 K, showing a continuum film with a roughness RMS of $6.8 \pm 1.3 \text{ nm}$.

Figure 7.6 (a) depicts AFM images of 20 *min* samples, captured in semicontact mode, highlighting the scan size of $1 \mu\text{m}^2$. A corresponding 3D plot is shown in Figure 7.6 (b). Figure 7.6 (c) shows the height distribution histogram the main lies on $\sim 11 \text{ nm}$.

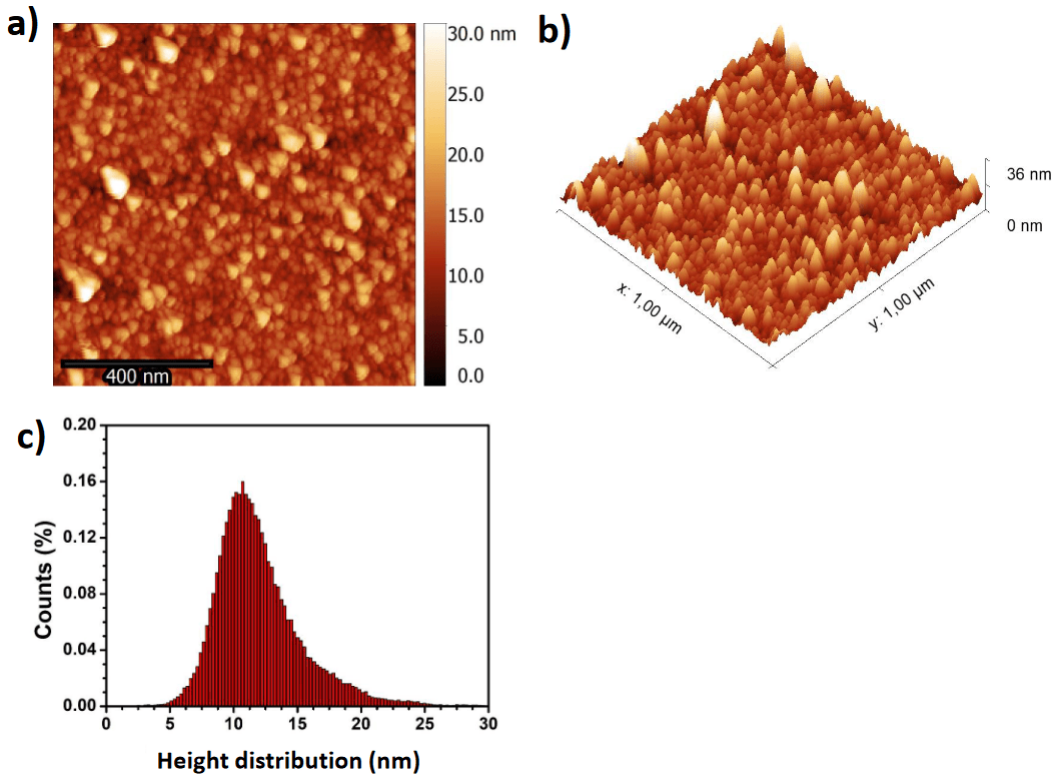


Figure 7.6: AFM image showing the topography of the 20 min sample of an area of $1 \mu\text{m}^2$, (a) show total coverage of the substrate surface the grain analysis shows the respective $\text{RMS} = 3.7 \pm 1.6 \text{ nm}$ roughness. In (b) show a 3D image of the film surface. In (c) the histogram of the height distribution of the h-BN film ranging from 5 to 30 nm, the main lies on $10.8 \pm 0.3 \text{ nm}$.

As the growth time increases, two fundamental changes become evident: an increase in the nucleation density and the growth rate. Furthermore, the roughness of the sample surface experiences variations in response to changing growth time conditions. It is observed as the growth time increases the roughness of the root mean square (RMS) decreases. For $t = 5 \text{ min}$, $t = 10 \text{ min}$, and $t = 20 \text{ min}$ the obtained values to the RMS roughness were $8.4 \pm 3.0 \text{ nm}$, $6.8 \pm 1.3 \text{ nm}$, and $3.7 \pm 1.6 \text{ nm}$, respectively. This implies that, although there is evidence of a decrease in film thickness over time, the average height is dominated by the height of the hillocks due to their rapid formation.

This notable feature mentioned as "hillocks" [61] is an extrusion of film material extracted from grains or grain boundaries during a process that relieves compressive stress caused by a mismatch in thermal expansion coefficients between h-BN and the substrate, this feature leads to an overvalued surface roughness in the h-BN films [96].

The tension felt by the film caused by the substrate can create a gradient between the relatively relaxed grains and the surrounding films. This gradient causes the atoms to flow along the film-substrate interface, resulting in "hillock"

growth from the base [96].

In a study by Yang et al. (2018), these features identified as "hillock" were characterized as islands or detritus in h-BN grown by metalorganic chemical vapor deposition (MOCVD) in sapphire, and their density was influenced by NH_3 flux [103].

The measured height of the hillock is 10 to 100 nm with a displacement lateral coverage of 0.1 to 10 nm . The high density of "hillocks" on the h-BN surface makes it difficult to form thin, smooth films over a large area, and the roughness of the surface limits the potential applications of the material [103]. Understanding these surface effects is crucial to reducing defects and enabling the production of continuous films with controlled thickness.

7.4 Contact Angle

The hydrophobicity capacity of the coating was analyzed using the water contact angle (CA). Figure 7.7 displays water droplets on h-BN thin films for CA measurements were made considering the synthesized films at different growth time conditions. The measured CA of the bare Si substrate was $\theta = 61.0^\circ \pm 1.0$, signifying its hydrophilic nature.

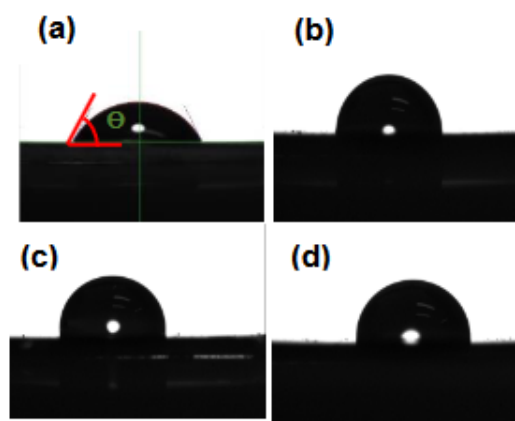


Figure 7.7: Water droplets on bare Si and on the Si substrate coated with h-BN films at 10 min of growth time deposition. (a) bare Si - $\theta = 61.0^\circ \pm 1.0$, and (b) 5 min - $\theta = 101.0^\circ \pm 3.0$, (c) 10 min - $\theta = 105.0^\circ \pm 5.0$, and (d) 20 min - $\theta = 100.0^\circ \pm 1.0$.

When examining the Si surface coated with h-BN film, for the as-grown samples the results show clear evidence that the wettability decreased with the deposition of h-BN thin films at all deposition times. This improvement was attributed to the outstanding physical properties of h-BN.

For the grown samples at $t = 5$ min, $t = 10$ min, and $t = 20$ min, the values obtained for contact angles were $\theta = 101.0^\circ \pm 3.0$, $\theta = 105.0^\circ \pm 5.0$, and $\theta = 100.0^\circ \pm 1.0$, respectively. All the surface is smooth (roughness RMS below 8 nm) which indicates that hydrophobicity depends only on the surface energy of the surface.

7.4.1

Scanning Transmission/Electron Microscopy (SEM) and (STEM)

Figure 7.8 shows scanning electron microscopy (SEM) images of h-BN films grown on Si $\langle 100 \rangle$ under identical conditions for 5, 10, and 20 minutes of growth time, with a scale bar of 1 and 10 μm , are illustrated the surface morphology of the samples.

The images reveal a circular pattern inherent to the films under study, that is, a small aspect ratio. Additionally, these small circular structures, confirmed in AFM analysis as "hillocks" features with brighter contrast (white) than the background, are visible in these images.

With increasing growth times (5 to 20 minutes), a smooth and continuous film forms along the surface of Si, as shown in Figure 7.8 (a, c, e) the 10 μm scale bar. This indicates that the density of the multilayer sites increases, suggesting that the growth mechanism follows the Frank Van der Merwe model, i.e., growth layer-by-layer [27].

This behavior is similar to the growth of graphene in nickel [104] under LPCVD, except for the presence of multilayer sites and their development over time. This suggests that the growth of h-BN on Si $\langle 100 \rangle$ under such LPCVD is not self-limiting, in contrast to the case of graphene on the copper substrate [105].

A cross section SEM image of the hillock is shown in Figure 7.9, the measured height for this structure was ranging from 280 - 350 nm.

The thickness of h-BN multilayer films was further studied using transverse STEM. The surface of the film was coated with a platinum film deposited with an electron beam (Pt electron surface) with the following dimensions (10 $\mu\text{m} \times 2 \mu\text{m} \times 100 \text{ nm}$).

Subsequently, a second layer of platinum was deposited with an ion beam (Pt dep) with the following dimensions (to protect it from possible damage caused by the Ga ion beam). Subsequently, a lamella extracted from the film was transferred to a grid to obtain the estimated profile height of the h-BN film through cross-sectional STEM measurements, resulting in a value of approximately 20 nm, as illustrated in Figure 7.10.

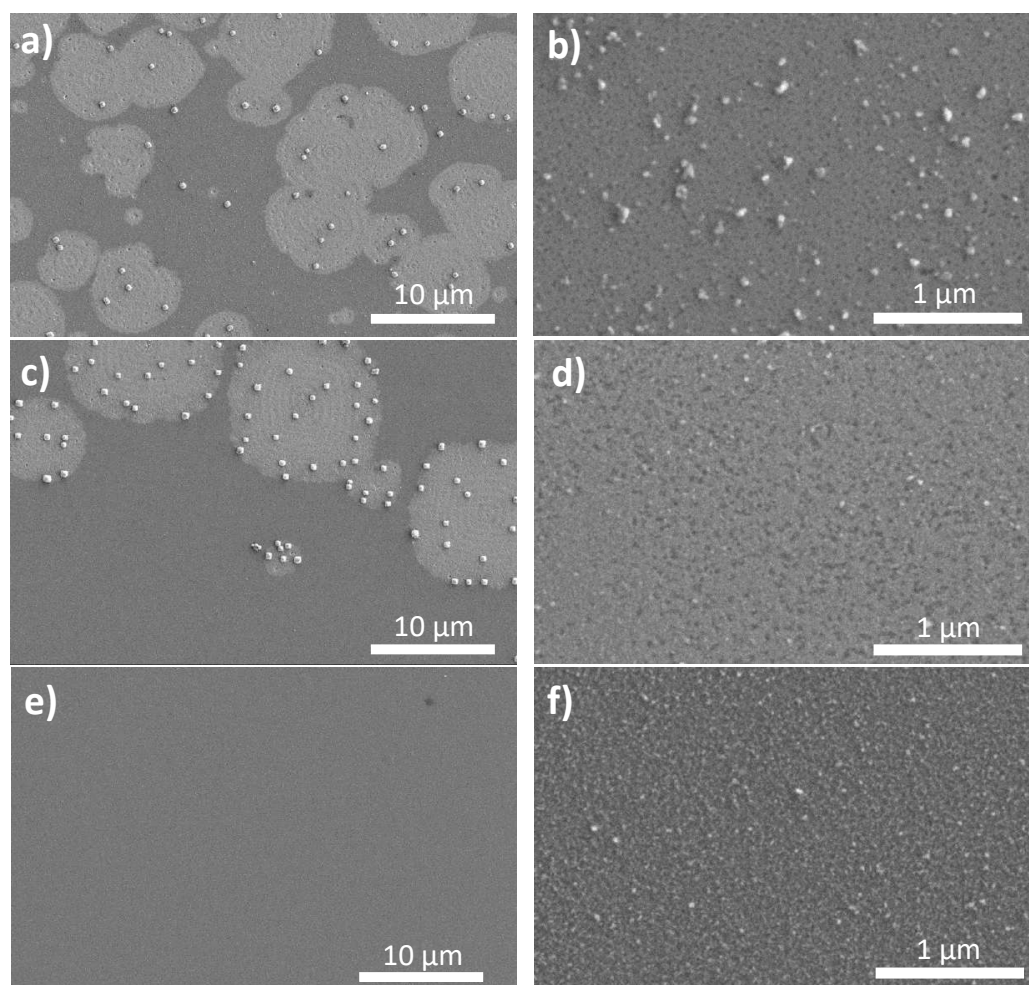


Figure 7.8: Scanning electron microscopy (SEM) images of h-BN films grown at 1373 K are provided. (a-b) displays a 5-min grown sample exhibiting a circular pattern characterized by small aspect ratios, and features identified as "hillocks" with a brighter contrast (white). (c-d) displays a 10-min grown sample exhibiting a circular pattern and features and (e-f) depict the sample at 20-min showcasing a continuous and a coverage of the surface with the h-BN film.

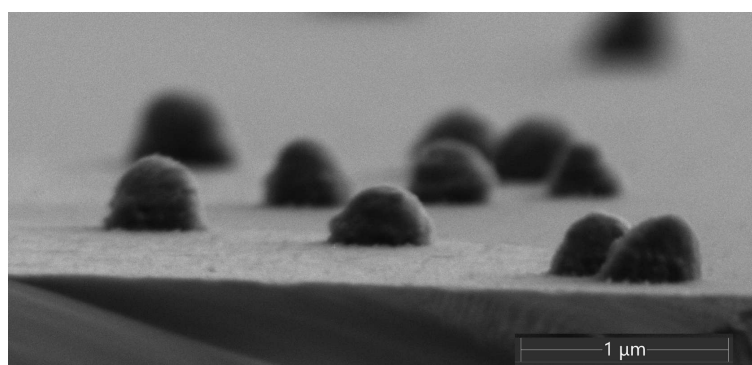


Figure 7.9: Cross-section SEM image of h-BN film showing the hillock features with height of ~ 300 nm

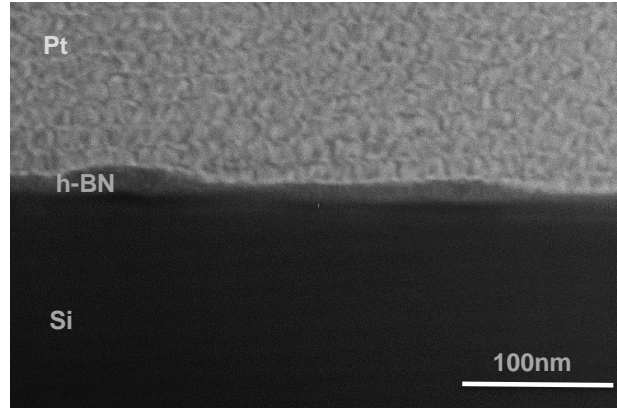


Figure 7.10: Cross-section STEM image of h-BN film depicting an h-BN film, overlaid with a 100 nm thick platinum (Pt) coating, grown on a Si $\langle 100 \rangle$ substrate, following a 10-minute growth period at 1373 K.

7.5

UV-visible spectroscopy

The UV-visible experiment was conducted to investigate the optical properties of the h-BN film and the optical energy gap related to its direct-band transition [47]. Absorption spectra were obtained, with the findings elucidated in Figure 7.11. The samples were irradiated with white light, and the absorbance of the samples in function of the incident wavelength was investigated.

From the absorbance graphic, the optical bandgap can be calculated using Tauc's Equation 2-2 [68]. This expression is usually used for III-V semiconductors (wide bandgap) like h-BN. Figure 7.11 shows that the h-BN film absorption spectra in a wavelength range of 200-340 nm, and one absorption peak at ~ 210 nm is observed.

Besides, a fundamental optical parameter, the optical bandgap (OBG), is achieved by considering a direct transition between the valence and conduction bands. When $(\alpha h\nu)^2$ assumes a zero value, an extrapolation is applied to determine the spectras offset followed by a straight line. Therefore, the corresponding $h\nu$ value aligns with the optical bandgap (E_g). The inset plot of Figure 7.11 (a-c) depicts the extrapolation made to determine the E_g of the h-BN film grown at 1373 K at 10 min, the E_g was obtained for the three samples 5.7, 5.6 and 5.7 eV, respectively.

The measured gap for the h-BN film is smaller than the theoretical gap value of a single layer (6 eV). This could be due to the layer-layer interaction, i.e., increasing the electronic band dispersion tends to reduce the gap. In particular, the band gap obtained is larger than the expected value for the bulk h-BN, ranging from 5.2 to 5.4 eV [5, 69, 56].

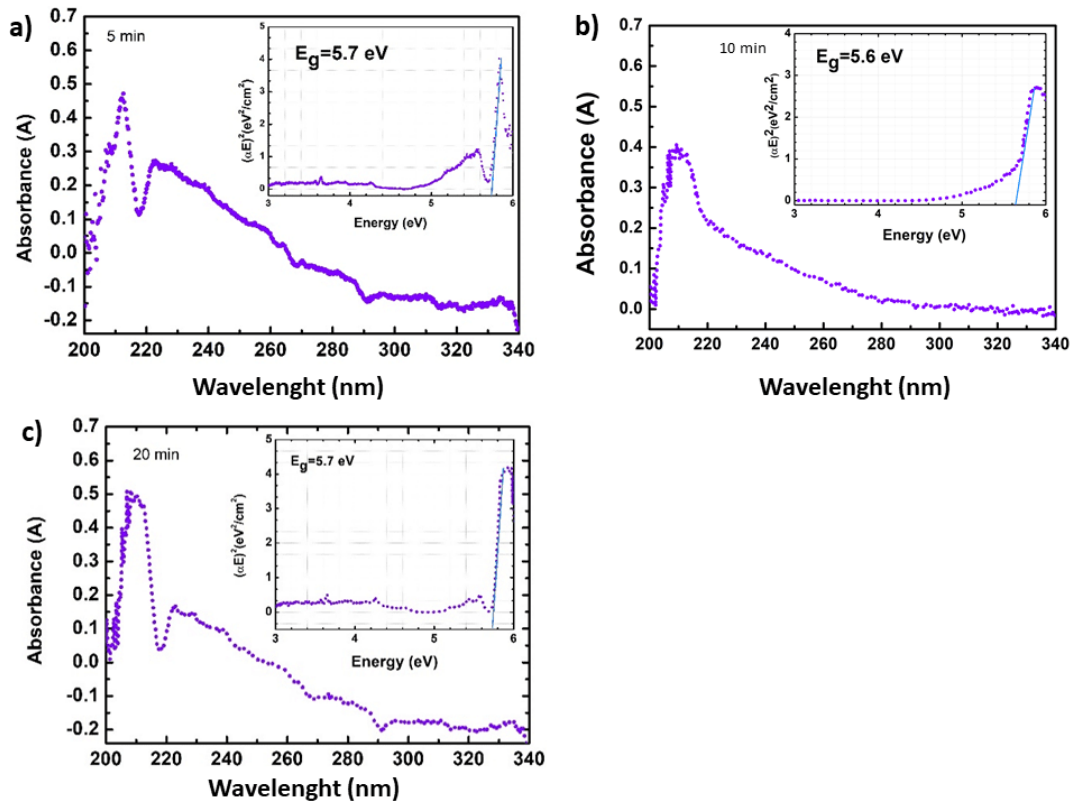


Figure 7.11: The UV-Vis spectrum of h-BN films grown at 1373 K on a silicon substrate, the inset shows an analysis of the optical bandgap by applying the Tauc's equation. samples grown at (a) 5 min the E_g of 5.7 eV (b) 10 min E_g of 5.6 eV and (c) 20 min E_g of 5.7 eV.

As a result, the process observed in this study produces thin BN films. This analysis provides a comprehension of the optical characteristics of the material, and then contributes to understanding the photonic behavior of h-BN and paving the way for optoelectronic and electronic applications.

7.6 Summary

h-BN films were synthesized by varying the growth time, and characterization techniques were employed to elucidate the role of growth time in the films. The aim was to produce thin films. A correlation was observed between growth time and film thickness, showing that reducing the growth time produced thinner films. Furthermore, increasing the time resulted in greater substrate coverage and films with lower roughness. An important characteristic observed in the films was the appearance of hillock structures, related to the random accumulation of material on the surface of the film. These structures pose a problem as they increase the roughness because they are higher than the film surface.

Efforts were made to understand the factors that promote these charac-

teristics. One factor investigated was the treatment time of Si with HF, which was reduced from 1 minute to 10 seconds, as deep circular structures and holes in Si were observed. However, the studies did not provide enough information to infer the contribution of the Si treatment time with HF. Another factor considered was the growth temperature. Since the melting temperature of Si is 1687 K, films grown at 1273 K did not show these patterns, while films grown at 1373 K showed hillocks and circular patterns. This information serves as a starting point for improving the quality of future film growth and controlling thickness without the formation of hillock structures.

8

Conclusion and perspectives

In summary, h-BN films were synthesized on Si <100> substrates using LPCVD, employing B and N elemental sources derived from Borane-ammonia powder. The effect of the growth temperature 1273-1373 K at 10 minutes, and at 1 hour, and growth durations at 5-20 minutes at 1373 K, was investigated. A systematic characterization of the as-grown h-BN films was conducted. The crystalline nature of the h-BN films was confirmed by Raman spectroscopy, showing a characteristic peak at $\sim 1374 \text{ cm}^{-1}$. Notably, a correlation between Raman peak intensity and growth duration was observed, with the increase in growth time resulting in a gradual increase in Raman peak intensity, indicating that Raman intensity is proportional to the number of h-BN layers. Further validation of the B-N bond was achieved through FTIR spectroscopy, which exhibited an absorption band centered at $\sim 1373.2 \text{ cm}^{-1}$, corroborating the Raman results. Additionally, X-ray Photoelectron Spectroscopy (XPS) measurements revealed a B:N ratio of 1.01 in the h-BN films, closely aligning with the theoretically stoichiometric value of 1.0. XPS studies also demonstrated the surface protection capability of Si since the measurements were made one month after growth and did not show the signal corresponding to SiO_2 , only relative to Si, however, to understand the protection, it is necessary to conduct corrosion tests or temporal evolution tests. Furthermore, the XPS analyses corroborated the increase in the number of layers with growth time, as revealed through the characteristics of the Si substrate in the Survey spectrum. Atomic Force Microscopy (AFM) was employed to analyze surface topography and morphology, displaying two features across the film: "hillocks" and patterned circular structures arranged on the Si surface. As the temperature increased, the surface coverage also increased, which promoted the appearance and growth of "hillocks". Therefore, temperature plays a crucial role in the growth kinetics, including desorption and diffusion of species on the substrate, thereby affecting the nucleation density, the size of nanocrystals and grains. The evaluation of h-BN thin film wettability indicated enhanced hydrophobicity compared to bare Si substrates coated with h-BN, showing a contact angle (CA) of $\sim 100^\circ$, indicating hydrophobic film properties. The SEM image indicated features of prominent contrast identified as small patterned circular structures, suggesting a possible effect of temperature on the recrystallization of Si at temperatures of 1373 K, given that the melting point of Si is 1687 K, also seen in the AFM analysis. Furthermore, the optical bandgap of

the h-BN films on Si substrates $\langle 100 \rangle$ was determined to be ~ 5.6 eV, which is relatively close to the theoretically calculated value for a monolayer (~ 6 eV), indicating the production of thin films. Furthermore, after understanding possible factors that affect the quality of the films, better quality was observed in films grown for 1 hour by varying the temperature. These films exhibit good quality, smoothness, and continuity without the formation of hillocks, they were subjected to tribology tests, indicating high wear resistance, and exhibited a low coefficient of friction, showing promise in the application of solid lubricants, as the coefficient of friction (CoF) was kept low during 1h:40min of the test. This study has yielded valuable insights into the nucleation and growth behavior of h-BN, particularly highlighting the formation of thinner films with decreased growth time, a phenomenon corroborated by complementary techniques that provided clear evidence of these observations. Films grown at different temperatures maintaining the same growth period of 10 min exhibited various morphologies, such as 2D nanostructures and continuous films on the Si surface with different sizes of nanocrystals. Subsequent investigations are warranted to further elucidate the nucleation and growth mechanisms of this material, aiming to contribute to advancements in Van der Waals (vdW) material synthesis. These findings underscore the potential of LPCVD as an effective technique for achieving controlled growth of continuous h-BN layers on large areas using Si substrates, which are utilized in the semiconductor industry. Moreover, the protective, tribological, and hydrophobic properties of h-BN highlight its utility as an insulator or ultra-wide bandgap material, wear protective and a water-repellent coating, offering significant potential in various technological domains, such as optoelectronics, photonics, and ultra-wide-bandgap electronics.

As a perspective, our aim is to produce continuous 2D films on the surface. To achieve this, we need to modify the synthesis parameters. In addition, we plan to deposit other materials, such as graphene and TMDs, since, as mentioned earlier, h-BN serves as a substrate for these materials. We also want to continue studying the properties of h-BN as a protective material, conducting corrosion tests, and using it as a dielectric layer in devices.

Bibliography

- [1] Roland Yingjie Tay, Siu Hon Tsang, Manuela Loeblein, Wai Leong Chow, Guan Chee Loh, Joo Wah Toh, Soon Loong Ang, and Edwin Hang Tong Teo. Direct growth of nanocrystalline hexagonal boron nitride films on dielectric substrates. *Applied Physics Letters*, 106(10), 2015. Cited 5 times in pages 12, 13, 23, 25, and 47.
- [2] Chen Xi, Tan Chunbo, Liu Xiaohang, Kairan Luan, Yufeng Guan, Xiuhuan Liu, Jihong Zhao, Lixin Hou, Yanjun Gao, and Zhanguo Chen. Growth of hexagonal boron nitride films on silicon substrates by low-pressure chemical vapor deposition. *Journal of Materials Science: Materials in Electronics*, 32, 02 2021. Cited 3 times in pages 12, 22, and 26.
- [3] M. Topsakal, E. E. Aktürk, and S. Ciraci. First-principles study of two- and one-dimensional honeycomb structures of boron nitride. *Physical Review B*, 79(11):115442, March 2009. Cited 4 times in pages 12, 27, 28, and 29.
- [4] CE Ekuma, V Dobrosavljević, and D Gunlycke. First-principles-based method for electron localization: application to monolayer hexagonal boron nitride. *Physical Review Letters*, 118(10):106404, 2017. Cited 2 times in pages 12 and 27.
- [5] Li Song, Lijie Ci, Hao Lu, Pavel B. Sorokin, Chuanhong Jin, Jie Ni, Alexander G. Kvashnin, Dmitry G. Kvashnin, Jun Lou, Boris I. Yakobson, and Pulickel M. Ajayan. Large scale growth and characterization of atomic hexagonal boron nitride layers. *Nano Letters*, 10(8):3209–3215, 2010. PMID: 20698639. Cited 10 times in pages 12, 21, 23, 28, 30, 31, 32, 78, 80, and 102.
- [6] B. Arnaud, S. Lebègue, P. Rabiller, and M. Alouani. Huge excitonic effects in layered hexagonal boron nitride. *Phys. Rev. Lett.*, 96:026402, Jan 2006. Cited 4 times in pages 12, 21, 28, and 29.
- [7] Kang Hyuck Lee, Hyeon-Jin Shin, Jinyeong Lee, In-yeal Lee, Gil-Ho Kim, Jae-Young Choi, and Sang-Woo Kim. Large-scale synthesis of high-quality hexagonal boron nitride nanosheets for large-area graphene electronics. *Nano letters*, 12(2):714–718, 2012. Cited 3 times in pages 12, 32, and 33.
- [8] Hsun-Jen Chuang, Bhim Chamlagain, Michael Koehler, Meeghage Madusanka Perera, Jiaqiang Yan, David Mandrus, David Tomanek, and Zhix-

- ian Zhou. Low-resistance 2D/2D ohmic contacts: a universal approach to high-performance WSe_2 , MoS_2 , and $MoSe_2$ transistors. *Nano letters*, 16(3):1896–1902, 2016. Cited 3 times in pages 12, 33, and 34.
- [9] Young Cho and Sung Ahn. Fabricating a raman spectrometer using an optical pickup unit and pulsed power. *Scientific Reports*, 10, 07 2020. Cited 2 times in pages 13 and 38.
- [10] Bruno Ricardo de Carvalho. *Raman Spectroscopy In MoS_2 -Type Transition-Metal Dichalcogenides*. PhD thesis, Universidade Federal de Minas Gerais, 2017. Cited 2 times in pages 13 and 39.
- [11] Roman V. Gorbachev, Ibtisam Riaz, Rahul R. Nair, Rashid Jalil, Liam Britnell, Branson D. Belle, Ernie W. Hill, Kostya S. Novoselov, Kenji Watanabe, Takashi Taniguchi, Andre K. Geim, and Peter Blake. Hunting for monolayer boron nitride: Optical and raman signatures. *Small*, 7(4):465–468, 2011. Cited 4 times in pages 13, 41, 86, and 93.
- [12] Stefan Hufner. *Photoelectron spectroscopy: principles and applications*. Advanced texts in physics. Springer, Berlin ; New York, 3rd ed edition, 2003. Cited 4 times in pages 13, 44, 45, and 46.
- [13] P. Eaton and P. West. *Atomic Force Microscopy*. OUP Oxford, 2010. Cited 4 times in pages 13, 49, 50, and 51.
- [14] S.J. Pennycook and P.D. Nellist. *Scanning Transmission Electron Microscopy: Imaging and Analysis*. Springer New York, 2011. Cited 2 times in pages 13 and 54.
- [15] D.B. Williams and C.B. Carter. *Transmission Electron Microscopy: A Textbook for Materials Science*. Number v. 1 in Cambridge library collection. Springer, 2009. Cited 2 times in pages 13 and 55.
- [16] J. Goldstein, D.E. Newbury, D.C. Joy, C.E. Lyman, P. Echlin, E. Lifshin, L. Sawyer, and J.R. Michael. *Scanning Electron Microscopy and X-Ray Microanalysis: Third Edition*. Springer US, 2012. Cited 2 times in pages 13 and 56.
- [17] B. Bhushan. *Handbook of Micro/Nanotribology: Second Edition*. Mechanics & Materials Science. CRC-Press, 1999. Cited 3 times in pages 14, 59, and 60.
- [18] Chuang Xu, Bin Li, Xiao Yuan, Cui Liu, Chun-yin Shen, and Gan-ce Dai. Separation of backsheets from waste photovoltaic(pv) modules by ultrasonic

- irradiation. *IOP Conference Series: Earth and Environmental Science*, 242:032046, 03 2019. Cited 3 times in pages 14, 61, and 62.
- [19] Samuel Frueh, Richard Kellett, Carl Mallery, Trent Molter, William S. Willis, Cecil KingTMondu, and Steven L. Suib. Pyrolytic Decomposition of Ammonia Borane to Boron Nitride. *Inorganic Chemistry*, 50(3):783–792, February 2011. Cited 2 times in pages 19 and 64.
- [20] K. S. Novoselov, A. K. Geim, S. V. Morozov, D. Jiang, Y. Zhang, S. V. Dubonos, I. V. Grigorieva, and A. A. Firsov. Electric field effect in atomically thin carbon films. *Science*, 306(5696):666–669, 2004. Cited in page 21.
- [21] K. S. Novoselov, D. Jiang, F. Schedin, T. J. Booth, V. V. Khotkevich, S. V. Morozov, and A. K. Geim. Two-dimensional atomic crystals. *Proceedings of the National Academy of Science*, 102:10451–10453, July 2005. Cited in page 21.
- [22] Andrew E. Naclerio and Piran R. Kidambi. A Review of Scalable Hexagonal Boron Nitride (h-BN) Synthesis for Present and Future Applications. *Advanced Materials*, 35(6):2207374, 2023. Cited 2 times in pages 21 and 22.
- [23] Guillaume Cassabois, Pierre Valvin, and Bernard Gil. Hexagonal boron nitride is an indirect bandgap semiconductor. *Nature Photonics*, 10, 12 2015. Cited in page 21.
- [24] D. M. Hoffman, G. L. Doll, and P. C. Eklund. Optical properties of pyrolytic boron nitride in the energy range 0.05—10 ev. *Phys. Rev. B*, 30:6051–6056, Nov 1984. Cited in page 21.
- [25] Kenji Watanabe, Takashi Taniguchi, and Hisao Kanda. Direct-bandgap properties and evidence for ultraviolet lasing of hexagonal boron nitride single crystal. *Nature Materials*, 3:404–409, 2004. Cited in page 21.
- [26] S. J. Grenadier, A. Maity, J. Li, J. Y. Lin, and H. X. Jiang. Origin and roles of oxygen impurities in hexagonal boron nitride epilayers. *Applied Physics Letters*, 112(16):162103, 04 2018. Cited in page 21.
- [27] Ki Kang Kim, Allen Hsu, Xiaoting Jia, Soo Min Kim, Yumeng Shi, Mario Hofmann, Daniel Nezich, Joaquin F. Rodriguez-Nieva, Mildred Dresselhaus, Tomas Palacios, and Jing Kong. Synthesis of monolayer hexagonal boron nitride on cu foil using chemical vapor deposition. *Nano Letters*, 12(1):161–166, 2012. PMID: 22111957. Cited 3 times in pages 21, 23, and 100.

- [28] Lu Hua Li, Jiri Cervenka, Kenji Watanabe, Takashi Taniguchi, and Ying Chen. Strong oxidation resistance of atomically thin boron nitride nanosheets. *ACS Nano*, 8(2):1457–1462, 2014. PMID: 24400990. Cited in page 21.
- [29] N. A. Novikova, E. G. Vlasov, and L. B. Nepomnyashchii. Huge excitonic effects in layered hexagonal boron nitride. *Refractories*, 12:667–680, 1971. Cited in page 21.
- [30] E. K. Sichel, R. E. Miller, M. S. Abrahams, and C. J. Buiocchi. Heat capacity and thermal conductivity of hexagonal pyrolytic boron nitride. *Phys. Rev. B*, 13:4607–4611, May 1976. Cited in page 21.
- [31] Kenji Watanabe, Takashi Taniguchi, Takahiro Niiyama, Kenta Miya, and Masateru Taniguchi. Far-ultraviolet plane-emission handheld device based on hexagonal boron nitride. *Nature Photonics - NAT PHOTONICS*, 3:591–594, 09 2009. Cited in page 21.
- [32] C. R. Dean, A. F. Young, I. Meric, C. Lee, L. Wang, S. Sorgenfrei, K. Watanabe, T. Taniguchi, P. Kim, K. L. Shepard, and J. Hone. Boron nitride substrates for high-quality graphene electronics. *Nature Nanotechnology*, 5(10):722–726, August 2010. Cited in page 21.
- [33] T.C. Doan, S. Majety, S. Grenadier, J. Li, J.Y. Lin, and H.X. Jiang. Hexagonal boron nitride thin film thermal neutron detectors with high energy resolution of the reaction products. *Nuclear Instruments and Methods in Physics Research Section A: Accelerators, Spectrometers, Detectors and Associated Equipment*, 783:121–127, 2015. Cited in page 21.
- [34] Liam Britnell, Roman V. Gorbachev, Rashid Jalil, Branson D. Belle, Fred Schedin, Mikhail I. Katsnelson, Laurence Eaves, Sergey V. Morozov, Alexander S. Mayorov, Nuno M. R. Peres, Antonio H. Castro Neto, Jon Leist, Andre K. Geim, Leonid A. Ponomarenko, and Kostya S. Novoselov. Electron tunneling through ultrathin boron nitride crystalline barriers. *Nano Letters*, 12(3):1707–1710, 2012. PMID: 22380756. Cited in page 21.
- [35] Haidong Chen, Zongxue Yu, Guangcheng Yang, Kexi Liao, Bokai Peng, Yuchi Guo, and Lijuan Zhu. A hydrophobic smart coating based on hexagonal boron nitride/metal-organic frameworks for high-performance corrosion protection. *Progress in Organic Coatings*, 172:107154, 2022. Cited in page 21.
- [36] Venkata A.S. Kandadai, Venkataramana Gadhamshetty, and Bharat K. Jasthi. Effect of buffer layer and substrate growth temperature on the

- microstructural evolution of hexagonal boron nitride thin films. *Surface and Coatings Technology*, 447:128805, 2022. Cited in page 21.
- [37] T. W. Scharf and S. V. Prasad. Solid lubricants: a review. *Journal of Materials Science*, 48(2):511–531, January 2013. Cited 2 times in pages 21 and 22.
- [38] Harun Yanar, Gencaga Purcek, Muhammed Demirtas, and Hasan Huseyin Ayar. Effect of hexagonal boron nitride (h-BN) addition on friction behavior of low-steel composite brake pad material for railway applications. *Tribology International*, 165:107274, January 2022. Cited in page 21.
- [39] Weiyi Lin, Pingping Zhuang, Deji Akinwande, Xue-Ao Zhang, and Weiwei Cai. Oxygen-assisted synthesis of hBN films for resistive random access memories. *Applied Physics Letters*, 115:073101, 08 2019. Cited in page 22.
- [40] Jiye Kim, Kyung-Yeon Doh, Seokho Moon, Chang-Won Choi, Hokyong Jeong, Jaewon Kim, Wonseok Yoo, Kyungwook Park, Kyeongock Chong, Chunhyng Chung, Hanmei Choi, Si-Young Choi, Donghwa Lee, and Jong Kyu Kim. Conformal growth of hexagonal boron nitride on high-aspect-ratio silicon-based nanotrenches. *Chemistry of Materials*, 35(6):2429–2438, 2023. Cited in page 22.
- [41] D. Pacilé, J. C. Meyer, Ç. Ö. Girit, and A. Zettl. The two-dimensional phase of boron nitride: Few-atomic-layer sheets and suspended membranes. *Applied Physics Letters*, 92(13):133107, 04 2008. Cited in page 22.
- [42] S. Nakhaie, J. M. Wofford, T. Schumann, U. Jahn, M. Ramsteiner, M. Hanke, J. M. J. Lopes, and H. Riechert. Synthesis of atomically thin hexagonal boron nitride films on nickel foils by molecular beam epitaxy. *Applied Physics Letters*, 106(21):213108, 05 2015. Cited in page 22.
- [43] Michael Snure, Qing Paduano, Merle Hamilton, Jodie Shoaf, and J. Matthew Mann. Optical characterization of nanocrystalline boron nitride thin films grown by atomic layer deposition. *Thin Solid Films*, 571:51–55, 2014. Cited 2 times in pages 22 and 93.
- [44] Haolin Wang, Xingwang Zhang, Junhua Meng, Zhigang Yin, Xin Liu, Yajuan Zhao, and Liuqi Zhang. Controlled growth of few-layer hexagonal boron nitride on copper foils using ion beam sputtering deposition. *Small*, 11(13):1542–1547, 2015. Cited in page 22.
- [45] Chaohua Zhang, Lei Fu, Shuli Zhao, Yu Zhou, Hailin Peng, and Zhongfan Liu. Controllable co-segregation synthesis of wafer-scale hexagonal boron

- nitride thin films. *Advanced Materials*, 26(11):1776–1781, 2014. Cited in page 22.
- [46] Yao Wen, Xunzhong Shang, Ji Dong, Kai Xu, Jun He, and Chao Jiang. Ultraclean and large-area monolayer hexagonal boron nitride on Cu foil using chemical vapor deposition. *Nanotechnology*, 26(27):275601, jun 2015. Cited in page 22.
- [47] Yumeng Shi, Christoph Hamsen, Xiaoting Jia, Ki Kang Kim, Alfonso Reina, Mario Hofmann, Allen Long Hsu, Kai Zhang, Henan Li, Zhen-Yu Juang, Mildred. S. Dresselhaus, Lain-Jong Li, and Jing Kong. Synthesis of few-layer hexagonal boron nitride thin film by chemical vapor deposition. *Nano Letters*, 10(10):4134–4139, 2010. PMID: 20812716. Cited 5 times in pages 22, 77, 92, 94, and 102.
- [48] Ren-Jie Chang, Xiaochen Wang, Shanshan Wang, Yuewen Sheng, Ben Porter, Harish Bhaskaran, and Jamie H. Warner. Growth of large single-crystalline monolayer hexagonal boron nitride by oxide-assisted chemical vapor deposition. *Chemistry of Materials*, 29(15):6252–6260, 2017. Cited 2 times in pages 22 and 64.
- [49] Roland Yingjie Tay, Hongling Li, Siu Hon Tsang, Minmin Zhu, Manuela Loeblein, Lin Jing, Fei Ni Leong, and Edwin Hang Tong Teo. Trimethylamine Borane: A New Single-Source Precursor for Monolayer h-BN Single Crystals and h-BCN Thin Films. *Chemistry of Materials*, 28(7):2180–2190, 2016. Cited 2 times in pages 22 and 64.
- [50] Jaehyun Han, Jun-Young Lee, Heemin Kwon, and Jong-Souk Yeo. Synthesis of wafer-scale hexagonal boron nitride monolayers free of aminoborane nanoparticles by chemical vapor deposition. *Nanotechnology*, 25(14):145604, mar 2014. Cited 3 times in pages 22, 23, and 64.
- [51] Xiaochen Wang, Thomas N. Hooper, Amit Kumar, Isobel K. Priest, Yuewen Sheng, Thomas O. M. Samuels, Shanshan Wang, Alex W. Robertson, Mercè Pacios, Harish Bhaskaran, Andrew S. Weller, and Jamie H. Warner. Oligomeric aminoborane precursors for the chemical vapour deposition growth of few-layer hexagonal boron nitride. *CrystEngComm*, 19:285–294, 2017. Cited 2 times in pages 22 and 64.
- [52] Ranjan Singhal, Elena Echeverria, David N. McIlroy, and Raj N. Singh. Synthesis of hexagonal boron nitride films on silicon and sapphire substrates by low-pressure chemical vapor deposition. *Thin Solid Films*, 733:138812, 2021. Cited 2 times in pages 22 and 93.

- [53] Sanjay Behura, Phong Nguyen, Rousan Debbarma, Songwei Che, Michael R. Seacrist, and Vikas Berry. Chemical Interaction-Guided, Metal-Free Growth of Large-Area Hexagonal Boron Nitride on Silicon-Based Substrates. *ACS Nano*, 11(5):4985–4994, 2017. PMID: 28441003. Cited 3 times in pages 22, 23, and 95.
- [54] Qing S. Paduano, Michael Snure, James Bondy, and Timothy W. C. Zens. Self-terminating growth in hexagonal boron nitride by metal organic chemical vapor deposition. *Applied Physics Express*, 7(7):071004, jun 2014. Cited in page 22.
- [55] Isaac G Juma, Gwangwoo Kim, Deep Jariwala, and Sanjay K Behura. Direct growth of hexagonal boron nitride on non-metallic substrates and its heterostructures with graphene. *IScience*, 24(11), 2021. Cited in page 23.
- [56] Sanjay K. Behura, Phong H. Nguyen, Songwei Che, Rousan Debbarma, and Vikas Berry. Large-Area, Transfer-Free, Oxide-Assisted Synthesis of Hexagonal Boron Nitride Films and Their Heterostructures with MoS_2 and WS_2 . *Journal of the American Chemical Society*, 137 40:13060–5, 2015. Cited 3 times in pages 23, 78, and 102.
- [57] A-Rang Jang, Seokmo Hong, Chohee Hyun, Seong In Yoon, Gwangwoo Kim, Hu Young Jeong, Tae Joo Shin, Sung O Park, Kester Wong, Sang Kyu Kwak, et al. Wafer-scale and wrinkle-free epitaxial growth of single-orientated multilayer hexagonal boron nitride on sapphire. *Nano letters*, 16(5):3360–3366, 2016. Cited in page 23.
- [58] Aaditya Pendse, Semih Cetindag, Pavel Rehak, Sanjay Behura, Haiqi Gao, Ngoc Hoang Lan Nguyen, Tongshuai Wang, Vikas Berry, Petr Král, Jerry Shan, et al. Highly efficient osmotic energy harvesting in charged boron-nitride-nanopore membranes. *Advanced Functional Materials*, 31(15):2009586, 2021. Cited in page 23.
- [59] Chen Wang, Sanjay K Behura, and Vikas Berry. Temperature dependent device characteristics of graphene/h-bn/si heterojunction. *Semiconductor Science and Technology*, 35(7):075020, 2020. Cited in page 23.
- [60] Jaebeom Lee, Arul V Ravichandran, Jaidah Mohan, Lanxia Cheng, Antonio T Lucero, Hui Zhu, Zifan Che, Massimo Catalano, Moon J Kim, Robert M Wallace, et al. Atomic layer deposition of layered boron nitride for large-area 2D electronics. *ACS applied materials & interfaces*, 12(32):36688–36694, 2020. Cited in page 23.

- [61] Michael S. Bresnehan, Matthew J. Hollander, Maxwell Wetherington, Ke Wang, Takahira Miyagi, Gregory Pastir, David W. Snyder, Jamie J. Gengler, Andrey A. Voevodin, William C. Mitchel, and et al. Prospects of direct growth boron nitride films as substrates for graphene electronics. *Journal of Materials Research*, 29(3):459–471, 2014. Cited 4 times in pages 23, 80, 95, and 98.
- [62] Miyagawa Hiroki, Kazuhide Kumakura, and Hideki Yamamoto. Substrate-transfer Technique Using h-BN for GaN-based High-power Transistors. *NTT Technical Review*, 14, 08 2016. Cited in page 27.
- [63] N Ooi, A Rairkar, L Lindsley, and JB Adams. Electronic structure and bonding in hexagonal boron nitride. *Journal of Physics: Condensed Matter*, 18(1):97, 2005. Cited in page 27.
- [64] Jingang Wang, Fengcai Ma, and Mengtao Sun. Graphene, hexagonal boron nitride, and their heterostructures: properties and applications. *RSC Adv.*, 7:16801–16822, 2017. Cited 3 times in pages 27, 30, and 31.
- [65] Andrii Goriachko, He, Marcus Knapp, Herbert Over, Martina Corso, Thomas Brugger, Simon Berner, Juerg Osterwalder, and Thomas Greber. Self-Assembly of a Hexagonal Boron Nitride Nanomesh on Ru(0001). *Langmuir*, 23(6):2928–2931, 2007. PMID: 17286422. Cited in page 28.
- [66] E Hernandez, C Goze, P Bernier, and A Rubio. Elastic properties of C and B x C y N z composite nanotubes. *Physical review letters*, 80(20):4502, 1998. Cited in page 30.
- [67] Rui Gao, Longwei Yin, Chengxiang Wang, Yongxin Qi, Ning Lun, Luyuan Zhang, Yu-Xian Liu, Le Kang, and Xianfen Wang. High-yield synthesis of boron nitride nanosheets with strong ultraviolet cathodoluminescence emission. *The Journal of Physical Chemistry C*, 113(34):15160–15165, 2009. Cited in page 31.
- [68] J. Tauc, R. Grigorovici, and A. Vancu. Optical properties and electronic structure of amorphous germanium. *physica status solidi (b)*, 15(2):627–637, 1966. Cited 3 times in pages 31, 78, and 102.
- [69] T.H. Yuzuriha and D.W. Hess. Structural and optical properties of plasma-deposited boron nitride films. *Thin Solid Films*, 140(2):199–207, 1986. Cited 2 times in pages 31 and 102.
- [70] Jingang Wang, Fengcai Ma, Wenjie Liang, and Mengtao Sun. Electrical Properties and Applications of Graphene, hexagonal Boron Nitride (h-BN)

- and Graphene / h-BN Heterostructures. *Materials Today*, 2:6–34, 07 2017. Cited 2 times in pages 32 and 33.
- [71] B. Podgornik, T. Kosec, A. Kocijan, and C. Donik. Tribological behaviour and lubrication performance of hexagonal boron nitride (h-BN) as a replacement for graphite in aluminium forming. *Tribology International*, 81:267–275, 2015. Cited in page 34.
- [72] Venkata A.S. Kandadai, Jacob B. Petersen, Venkataramana Gadhamshetty, and Bharat K. Jasthi. Synthesis of hexagonal boron nitride nanocoatings for corrosion prevention of iron substrates. *Surface and Coatings Technology*, 468:129736, 2023. Cited in page 35.
- [73] Peter Y. Yu and Manuel Cardona. *Fundamentals of Semiconductors: Physics and Materials Properties*. Springer-Verlag Berlin Heidelberg, New York, 2010. Cited 2 times in pages 37 and 39.
- [74] Alfred Christy, Yukihiro Ozaki, and Vasilis Gregoriou. Modern fourier transform infrared spectroscopy. *Wilson and Wilson's Comprehensive Analytical Chemistry*, pages 1–356, 01 2011. Cited 2 times in pages 42 and 43.
- [75] D. Briggs and M.P. Seah. *Practical Surface Analysis, Auger and X-ray Photoelectron Spectroscopy*. Practical Surface Analysis. Wiley, 1990. Cited 2 times in pages 44 and 45.
- [76] G. Binnig, C. F. Quate, and Ch. Gerber. Atomic force microscope. *Phys. Rev. Lett.*, 56:930–933, Mar 1986. Cited in page 48.
- [77] B. Voigtlander. *Atomic Force Microscopy*. NanoScience and Technology. Springer International Publishing, 2019. Cited 3 times in pages 48, 50, and 51.
- [78] Kelaine Chaves Gomes Höfelmann. Espectroscopia raman por transformada de fourier e análise de molhabilidade nos filmes finos de carbono amorfo hidrogenado (a-c:h), 2013. Cited in page 51.
- [79] K.L. Mittal. *Contact Angle, Wettability and Adhesion*. CRC Press, 2008. Cited 2 times in pages 51 and 52.
- [80] Robert Miller, Shugang Hu, Sonkarlay Weamie, Saavia Naame, and Dauda Kiazolu. Superhydrophobic coating fabrication for metal protection based on electrodeposition application: A review. *Journal of Materials Science and Chemical Engineering*, 09:68–104, 01 2021. Cited 2 times in pages 51 and 52.

- [81] Robert N. Wenzel. Resistance of solid surfaces to wetting by water. *Industrial & Engineering Chemistry*, 28(8):988–994, 1936. Cited in page 53.
- [82] V. Kazmiruk. *Scanning Electron Microscopy*. IntechOpen, 2012. Cited in page 56.
- [83] H.H. Perkampus. *UV-VIS Spectroscopy and Its Applications*. Springer laboratory. Springer-Verlag, 1992. Cited in page 57.
- [84] Jingxue Yu, Jie Li, Wenfeng Zhang, and Haixin Chang. Synthesis of high quality two-dimensional materials via chemical vapor deposition. *Chem. Sci.*, 6:6705–6716, 2015. Cited in page 60.
- [85] Chapter 1 - deposition technologies: An overview. In Peter M. Martin, editor, *Handbook of Deposition Technologies for Films and Coatings (Third Edition)*, pages 1–31. William Andrew Publishing, Boston, third edition edition, 2010. Cited in page 61.
- [86] Ramakrishna Podila, Apparao Rao, Pooja Puneet, Sriparna Bhattacharya, Sai Sunil Kumar Mallineni, Anurag Srivastava, Fengjiao Liu, Jaime Taha-Tijerina, Laura Peña-Parás, Demófilo Maldonado, Guangzhao Qin, Ming Hu, Yazeed Alaskar, Shamsul Arafin, Kang Wang, Qijin Chi, Mianqi Xue, Fengwang Li, Rebecca Cheung, and Li Guangshe. *Two-dimensional Materials-Synthesis, Characterization and Potential Applications*. 08 2016. Cited in page 61.
- [87] Yasir Beeran Pottathara, Yves Grohens, Vanja Kokol, Nandakumar Kalarikkal, and Sabu Thomas. Chapter 1 - synthesis and processing of emerging two-dimensional nanomaterials. In Yasir Beeran Pottathara, Sabu Thomas, Nandakumar Kalarikkal, Yves Grohens, and Vanja Kokol, editors, *Nanomaterials Synthesis, Micro and Nano Technologies*, pages 1–25. Elsevier, 2019. Cited in page 61.
- [88] Xin Cheng. Research and application of ultrasonic cleaning technology in medical equipment cleaning under computer control system. *Journal of Physics: Conference Series*, 1574:012042, 06 2020. Cited in page 62.
- [89] Paul Spizzirri, Jinghua Fang, S. Rubanov, E. Gauja, and S. Praver. Raman spectroscopy of silicon surfaces. *Materials Forum*, 34, 02 2010. Cited in page 75.
- [90] K. Ahmed, R. Dahal, A. Wertz, J.-Q. Lu, Y. Danon, and I. B. Bhat. Growth of hexagonal boron nitride on (111) Si for deep UV photonics and thermal

- neutron detection. *Applied Physics Letters*, 109(11):113501, 09 2016. Cited 3 times in pages 76, 93, and 95.
- [91] Max Franck, Jaroslaw Dabrowski, Markus Andreas Schubert, Christian Wenger, and Mindaugas Lukosius. Towards the Growth of Hexagonal Boron Nitride on Ge(001)/Si Substrates by Chemical Vapor Deposition. *Nanomaterials*, 12(19), 2022. Cited 4 times in pages 77, 80, 93, and 95.
- [92] R. J. Nemanich, S. A. Solin, and Richard M. Martin. Light scattering study of boron nitride microcrystals. *Phys. Rev. B*, 23:6348–6356, Jun 1981. Cited 2 times in pages 78 and 93.
- [93] V.G. Antunes, C.A. Figueroa, and F. Alvarez. A comprehensive study of the TiN/Si interface by X-ray photoelectron spectroscopy. *Applied Surface Science*, 448:502–509, 2018. Cited 2 times in pages 80 and 96.
- [94] Qiufeng An, Zhujun Lyu, Wenchao Shangguan, Bianli Qiao, and Pengwei Qin. The Synthesis and Morphology of a Perfluoroalkyl Oligosiloxane@SiO₂ Resin and Its Performance in Anti-Fingerprint Coating. *Coatings*, 8(3), 2018. Cited 2 times in pages 80 and 96.
- [95] Abhijit Biswas, Rishi Maiti, Frank Lee, Cecilia Y. Chen, Tao Li, Anand B. Puthirath, Sathvik Ajay Iyengar, Chenxi Li, Xiang Zhang, Harikishan Kannan, Tia Gray, Md Abid Shahriar Rahman Saadi, Jacob Elkins, A. Glen Birdwell, Mahesh R. Neupane, Pankaj B. Shah, Dmitry A. Ruzmetov, Tony G. Ivanov, Robert Vajtai, Yuji Zhao, Alexander L. Gaeta, Manoj Tripathi, Alan Dalton, and Pulickel M. Ajayan. Unravelling the room temperature growth of two-dimensional h-BN nanosheets for multifunctional applications. *Nanoscale Horizons*, 8(5):641–651, 2023. Cited 4 times in pages 80, 81, 83, and 85.
- [96] K. T. Raic. An explanation of hillock growth in thin Al films. *Surface Engineering*, 32(11):823–828, 2016. Cited 3 times in pages 81, 98, and 99.
- [97] Azimkhan Kozhakhmetov, Riccardo Torsi, Cindy Y Chen, and Joshua A Robinson. Scalable low-temperature synthesis of two-dimensional materials beyond graphene. *Journal of Physics: Materials*, 4(1):012001, November 2020. Cited in page 82.
- [98] Meenakshi Annamalai, Kalon Gopinadhan, Sang A. Han, Surajit Saha, Hye Jeong Park, Eun Bi Cho, Brijesh Kumar, Abhijeet Patra, Sang-Woo Kim, and T. Venkatesan. Surface energy and wettability of van der Waals structures. *Nanoscale*, 8(10):5764–5770, 2016. Cited in page 85.

- [99] Bharat Bhushan and Xiaodong Li. Micromechanical and tribological characterization of doped single-crystal silicon and polysilicon films for microelectromechanical systems devices. *Journal of Materials Research*, 12(1):54–63, January 1997. Cited in page 89.
- [100] M. R. Uddin, T. C. Doan, J. Li, K. S. Ziemer, J. Y. Lin, and H. X. Jiang. Electrical transport properties of (BN)-rich hexagonal (BN)C semiconductor alloys. *AIP Advances*, 4(8):087141, 08 2014. Cited in page 95.
- [101] S. Saha, A. Rice, A. Ghosh, S. M. N. Hasan, W. You, T. Ma, A. Hunter, L. J. Bissell, R. Bedford, M. Crawford, and S. Arafin. Comprehensive characterization and analysis of hexagonal boron nitride on sapphire. *AIP Advances*, 11(5):055008, 05 2021. Cited in page 95.
- [102] M. R. Uddin, S. Majety, J. Li, J. Y. Lin, and H. X. Jiang. Layer-structured hexagonal (BN)C semiconductor alloys with tunable optical and electrical properties. *Journal of Applied Physics*, 115(9):093509, 03 2014. Cited in page 95.
- [103] Xu Yang, Shugo Nitta, Kentaro Nagamatsu, Si-Young Bae, Ho-Jun Lee, Yuhuai Liu, Markus Pristovsek, Yoshio Honda, and Hiroshi Amano. Growth of hexagonal boron nitride on sapphire substrate by pulsed-mode metalorganic vapor phase epitaxy. *Journal of Crystal Growth*, 482:1–8, 2018. Cited in page 99.
- [104] Arjun Dahal and Matthias Batzill. Graphene-nickel interfaces: a review. *Nanoscale*, 6:2548–2562, 2014. Cited in page 100.
- [105] Pradeep Kumar Kashyap, Indu Sharma, and Bipin Kumar Gupta. Continuous growth of highly reproducible single-layer graphene deposition on cu foil by indigenously developed lpcvd setup. *ACS Omega*, 4(2):2893–2901, 2019. PMID: 31459519. Cited in page 100.